Ice Loads on Offshore Wind Farms

Studying the effects of different wind direction and ice concentration

Fabian Lambregts

Delft University of Technology And Norwegian University of Science and Technology

TUDelft

NTNU

Ice Loads on Offshore Wind Farms

Studying the effects of different wind direction and ice concentration

by

Fabian Lambregts

In partial fulfillment of the requirements for the *European Wind Energy Master (EWEM) – Offshore Engineering track*.

to obtain the degree of Master of Science:

MSc. Offshore Engineering at the Delft University of Technology,
MSc. Technology-Wind Energy at the Norwegian University of Science and Technology

to be defended publicly on **10-07-2025**.

Student number:	5083060 (TU Delft), 123740 (NTNU)	
Project duration:	January 20, 2025 – June 10, 2025	
Supervision:	Dr. ir. H. Hendrikse,	TU Delft, supervisor
	Prof. dr. K. V. Høyland,	NTNU, supervisor
	Prof. dr. R. K. Lubbad,	NTNU, co-supervisor
Thesis committee:	Dr. ir. H. Hendrikse,	TU Delft, Chair
	Dr. ir. J. Hoving,	TU Delft
	Dr. ir. W. Lu,	NTNU, Additional Expert Member
	Prof. dr. R. K. Lubbad,	NTNU, Additional Expert Member

Cover: Artificially generated picture using ChatGPT

An electronic version of this thesis is available at http://repository.tudelft.nl/.

TU Delft

NTNU

Preface

This thesis represents the final part of my academic journey. After completing my Bachelor's Degree in Civil Engineering, I was seeking a new challenge both on personal and academic level. The European Wind Energy Master was the perfect fit, creating new challenges and inspiring learning environments at three different universities (TU Delft, DTU and NTNU). From the beginning of my master, the interaction of ice with wind turbines sparked my interest. The novelty of this subject and the many challenges and unknowns was of main interest to me. Unfortunately, a course in Ice Engineering at UNIS, Svalbard, was no longer offered. This did not hold me back from going on with this thesis topic.

I would like to thank my supervisor Hayo Hendrikse for helping me to initiate this project from a very early stage (approx. 1 year ago). Moreover, for being involved throughout both my pre-thesis (NTNU) as my final thesis project. I would like to thank Knut Vilhelm Høyland, who was my supervisor throughout my pre-thesis project and during this work. Furthermore, for introducing me to ice engineering through the TBA4260 course at NTNU. Additionally, I would like to thank Raed Khalil Lubbad for joining my project as a co-supervisor. Helping me with the SAMS software and contributing to the biweekly feedback sessions. The feedback from all supervisors throughout this period was really useful and insightful. Finally, I want to thank Wenjun Lu for helping me with all possible questions regarding the SAMS software. Preventing me from getting stuck on software problems for to long.

On a personal note, I would like to thank my fellow EWEM students for all the good and fun times during the stay abroad. Making it a little less difficult to switch places every 6 months. Furthermore, I want to thank my family, friends and girlfriend for always supporting me no matter where I am. This support has helped me through the difficult times that are faced when studying and staying abroad.

Fabian Lambregts
Delft, June 2025

Summary

The greenhouse emissions caused by the energy sector must be significantly reduced to slow down the impact on climate. Therefore, a great shift towards renewable energy sources is of importance. A method of doing so is by using offshore wind energy. The development and growth of this renewable energy source introduce new challenges for the future. One of these challenges is designing offshore wind turbines for sea-ice loads. In Europe, the northern Baltic Sea is the main site of interest for the development of offshore wind farms (OWFs) that will be subjected to ice loads. However, little is known regarding how the ice behaves around these structures and how the presence of multiple turbines will influence the ice loads encountered. Therefore, the following research question is defined.

How is the ice loading on and ice drift around an offshore wind turbine influenced by it being part of an offshore wind farm?

First, an introduction to sea-ice terminology and ice action is given. This forms the theoretical framework for this thesis. Multiple methods are explored to analyse and summarise the ice loads experienced by a structure. These are later used to interpret the results obtained from simulations.

In this thesis, the main area of interest is the northern Baltic Sea (Bay of Bothnia). Therefore, the environmental conditions and sea-ice in this area have been thoroughly investigated. Image processing of ice fields over the years yields a starting point for generating ice fields that are used in the simulations. Furthermore, all relevant ice properties are considered and, when possible, adjusted for the lower salinity present in the Baltic Sea water. In addition, current and wind conditions are determined to determine in which way these play a role in the drift of the ice.

In this thesis, both the effect of the wind directions and ice concentration are investigated. Combining these results in 16 total simulation scenarios that will be modelled using the Simulator for Arctic Marine Structures (SAMS) software. In total, four different wind directions (0, 15, 30 and 45 degrees) and four different ice concentrations (50%, 60%, 70% and 80%) are used. The OWF used has a grid layout with 5x5 turbines and an ice field of 15x15 km. The ice field is simulated such that it drifts into the OWF, no ice is initially present in the wind farm. Due to computational limitations, for each scenario, 45000 seconds (12.5 hours) of data is simulated.

To analyse the obtained force data, the Ice Load Factor (ILF) and the Ice Load Contact Factor (ILCF) are defined. Both use rainflow counting to analyse the number of force cycles that occur over time. A lower threshold of 100 kN is used to focus on the higher impact interaction. In addition, an upper limit of 10.8 MN is used to eliminate numerical peaks from the results. Both factors use the sum from the product of each force bin and it's corresponding amount of cycles. Each load bin has a size of 0.5 MN and the average value of this bin is used in the product. Summing this over all load bins yields the numerator for both factors. The main difference between the factors is the denominator. For the ILF the total potential exposed time is used based on the free-drift velocity of the ice. Since this does not take into account the actual time that the interaction occurs, the ILCF uses the total contact time of the ice with the structure. Both fractions are multiplied by the total simulated time to obtain a unit of Newton in both factors.

Based on the obtained data one can analyse each individual turbines and also group them. In this thesis the term, "Lines of turbines" is used to refer the order in which the ice interacts with the OWTs. Hence, the first line of turbines represents the turbines that first interact with the ice field. Moving further downstream, the following up lines are defined and can be analysed for all wind directions. Analyses on these lines of turbines gains insight on how the ice action changes when moving further down the OWF.

For the lowest ice concentration (IC = 50%) the ILF decrease for all wind directions in the lines of turbines is approximately the same. Only when the ice concentration increases, a more clear difference is seen for changing wind directions. Since a higher IC results in more ice floes in the ice field. Therefore, it is more likely that a turbine interacts with an ice floe. This influences the drift in and around the wind farm. Generally, more sideward movement is caused by higher ice concentrations. This makes ice more likely to interact with turbines further downstream. For lower concentrations, the ice continues to move along the same streamline resulting in less ice-structure interactions. The mean ILF is decreases by >70% and the sum by >75% after interacting with the first line of turbines in all scenarios. Hence, a significant reduction is present in the wind farm.

The interaction times for a 0 and 15 degree heading decrease significantly more over the lines of turbines. Furthermore, these wind angles result in the lowest ILCF sum and mean values for all ice concentrations. Based on the ILCF, one can conclude that these two wind directions result in the best reduction of ice loads based on the total interaction time. Furthermore, one concludes that the 30 degree wind angle yields the lowest reduction in interaction time and therefore has the lowest ice-structure interaction blockage effect. This could potentially be caused by the fact that this angle has the highest offset in the position of the turbine in y-direction. Therefore, turbines in previous lines do not prevent other turbines further downstream to interact with the ice field.

The computational times of these kinds of simulations are found to be significant. Therefore, it is explored whether machine learning (ML) could be used to predict the encountered ice loads. This could greatly influence the pace with which different OWF layouts or ice conditions can be tested more thoroughly. From the data obtained, different ML regressors are trained and tested for their performance. The usage of a Random Forest Regressor resulted in the most accurate results. However, these result are found not to be accurate enough to use them for prediction purposes. Therefore, it is found that first more data need to be gathered to train and test these models more extensively, and the usage of more complex ML models could potentially also improve the performance. Doing so could greatly influence the speed with which different parameters of influence can be analysed.

Contents

List of Figures

List of Tables

Nomenclature

Abbreviations

Abbreviation	Definition
CDF	Cumulative Density Function
DNV	Det Norske Veritas
DTU	Danmarks Tekniske Universitet
DTR	Decision Tree Regressor
FFT	Fast Fourier Transform
FSD(s)	Floe Size Distribution(s)
FY	First-Year, refers to the age of the ice
GVF	Gradient Vector Flow
LR	Linear Regression
IEC	International Electrotechnical Commission
ILF	Ice Load Factor
ILCF	Ice Load Contact Factor
ISO	International Organization for Standardization
MCD	Mean Caliper Diameter
ML	Machine Learning
MSE	Mean Squared Error
NDEM	Non Discrete Element Method
OWF(s)	Offshore Wind Farm(s)
OWT(s)	Offshore Wind Turbine(s)
PDF	Probability Density Function
PSD	Power Spectral Density
RF	Random Forest
SAMS	Simulator for Arctic Marine Structures
SIC/IC	Sea Ice Concentration
SVR	Support Vector Regression
Var	Variance

Symbols

Symbol	Definition	Unit
A_i	Total ice area	[m^2]
A_N	Nominal contact area	[m^2]
c	Weibull shape parameter	[-]
C_a	Air skin friction coefficient	[-]
C_c	Current skin friction coefficient	[-]
C_e	Form drag on a single floe	[-]
C_i	Ice concentration	[%]
C_R	Ice strength coefficient	[Pa]
C_w^e	Water form drag coefficient	[-]
D	Accumulated fatigue damage	[-]
dF_i	Mean ice force for load bin i	[N]
E	Expected value	[-]
E	Elastic modulus or Young's modulus	[Pa]
f	Coriolis parameter	[rad/s]
f_{AR}	Factor that accounts for narrow structures	[-]
F_a	Driving force by wind	[N]
F_c	Driving force by current	[N]
F_d	Driving Forces	[N]
F_G	Global ice force	[N]
F_H	Total horizontal ice force	[N]
g	Gravitational acceleration	[m/s^2]
G	Strain energy release rate	[J/m^2]
h_1	Reference thickness of 1 meter	[m]
h_i	Ice thickness	[m]
$\mathbf{k}$	Unit vector for rotational motion	[-]
K_c	Fracture toughness	[Pa$\sqrt{\text{m}}$]
K_{1c}	Fracture toughness, first mode failure	[Pa$\sqrt{\text{m}}$]
L_x and L_y	Ice field domain length	[m]
m_i	Mass of the ice	[kg]
n_i	Number of load cycles for load bin i	[-]
p_a	Air pressure	[Pa]
p_G	Global ice pressure	[Pa]
r_{lat}	Resolution in latitude	[deg/px]
r_{long}	Resolution in longitude	[deg/px]
t	Time	[s]
$t_{contact}$	Total ice-structure contact time	[s]
t_{exp}	Total time that a turbine is exposed to ice	[s]
t_{sim}	Total simulated time	[s]
$\mathbf{u}$	Ice drift velocity vector	[m/s]
u_1	Current velocity at z = -1 m	[m/s]
u_{10}	Wind velocity at z = 10 m	[m/s]
V_N	Number of floe vertices	[-]
v_b	Brine volume	[m^3]
v_i	Ice velocity	[m/s]
v_T	Total porosity of ice	[ppt]
w or w_s	Projected width	[m]
α	Power law exponent	[-]
β	Sea surface slope	[°]
$\dot{\epsilon}$	Strain rate of ice	[1/s]
Γ_{xx}	Autocorrelation function	[-]
γ_{xx}	Self-correlation function	[-]
λ	Weibull shape parameter	[-]

Symbol	Definition	Unit
μ	Poisson's ratio	[1/m]
μ	Friction coefficient	[-]
ϕ	Latitude degree	[$^\circ$]
ρ_a or ρ_{air}	Air density	[kg/m^3]
ρ_i	Ice density	[kg/m^3]
ρ_w or ρ_{water}	Water density	[kg/m^3]
σ	Stress within the ice	[Pa]
σ	Standard error for power law	[-]
σ_c	Compressive strength of ice	[Pa]
σ_f	Flexural strength of ice	[Pa]
τ_a	Shear stress from wind	[Pa]
τ_c	Shear stress from current	[Pa]
ξ	Rayleigh separator value	[-]

1 Introduction

1.1. Research Motivation

The energy sector is the largest contributor to greenhouse gas emissions. Development and growth of the renewable energy sector is crucial to significantly reduce these emissions. The EU aims to become a climate neutral continent by 2050, with its success highly dependent on the production of renewable energy. Within Europe, five sea basins are present that have a large potential to harvest offshore wind energy. These basins will play an important role in the transition to renewable energy (European Commission, n.d.).

Expanding the number of offshore wind farms (OWFs) creates additional engineering challenges. The Baltic Sea has seen a great increase in offshore wind projects over the years. With projects moving to the northern Baltic Sea, new engineering challenges are encountered. In the Baltic Sea, sea-ice and icing on structures is one of these new challenges (Hendrikse, 2024).

Due to these new challenges, research has been conducted on the interaction of Offshore Wind Turbines (OWTs) and sea-ice. The main focus has been on the dynamic response of a wind turbine to ice loads. Which is studied mainly with scale model testing using ice tanks. This gives the possibility of combining dynamic loads of ice with the other dynamic loads on the turbine (Hammer et al., 2023). These tests are conducted mainly for level ice conditions using a single structure. In real application, there will be multiple turbines in the vicinity of another, subjected to either broken or level ice. This could potentially influence the drift of the ice floes in the wind farm. Blockage effects could reduce the loads on turbines further downstream.

The ice action and drift in Offshore Wind Farms (OWFs) is a new topic, and there has not been much research done yet. Some different load scenarios that could occur on individual wind farm structures are discussed in Gravesen et al. (2023). Furthermore, the presence of the OWF can influence environmental conditions, such as local wind speeds. All these possible scenarios are identified and initially discussed in the previous specialisation project performed (Lambregts, 2024). This is a starting point for this work, with the main goal of analysing the ice loads in an OWF.

1.2. Problem Statement

One of the main challenges in ice engineering is the lack of data. There are three main full-scale data sets obtained from the Molikpaq platform, Norströmsgrund lighthouse, and the Confederation bridge (Høyland, 2024). Therefore, it is difficult to validate the results obtained by simulating ice loads. For wind turbines, this forms an additional challenge since for this kind of flexible structure, no full-scale data is available. The main data collected on the structural responses of offshore wind turbines is gathered by scale model tests, see Figure 1.1a. However, an increase in installed wind turbine foundation in ice regions gives the possibility to gain more data, see Figure 1.1b (Yu et al., 2020). Doing so gives possibilities for the future to generate more data on this phenomenon.

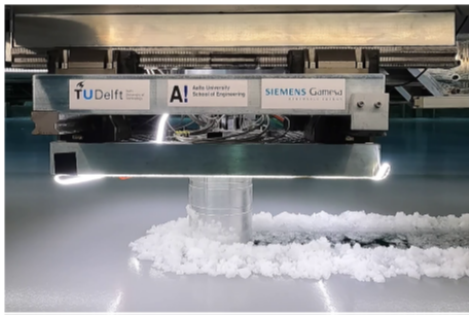

(a) An example of data gathering using scale model testing at the Aalto ice tank (Hammer et al., 2023).

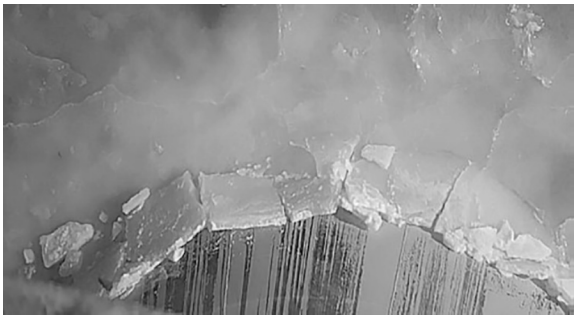

(b) An example of using field monitoring to gather full-scale data (Yu et al., 2020).

Figure 1.1: Different ways to gather data on structural response of offshore wind turbines in ice conditions.

The main novelty of ice engineering in wind farms is that the foundation structures are relatively close to each other. It is yet unknown how this will influence the ice field and the corresponding ice actions. The only known case with some similarities is when the ice passes the pillars of the Confederation Bridge, shown in Figure 1.2. However, the order of magnitude of the individual distance is significantly higher for OWTs. The distance between two piers for the confederation bridge is 250 m (Aïtcin et al., 2016), the typical distance between the turbines is four times larger. Furthermore, the structural properties of the pillars are fundamentally different from those of an OWT. This makes it difficult to compare them to each other.

Figure 1.2: Ice cut into geometric patterns by the Confederation Bridge captured by Paul Tymstra (Williams, 2018).

The design requirements for turbines in ice conditions are described in IEC 61400-3-1 (International Electrotechnical Commission, 2019). However, these only consider the presence of a single turbine. Therefore, for OWF design, it is vital to understand how the ice moves and behaves around the turbines.

1.3. Research Objective

The main goal of this research is to evaluate how and if the ice loads on individual turbines change when placed in a wind farm. To analyse multiple scenarios, both the wind direction and the ice concentration are varied. Wind has the greatest contribution to the drift speed of the ice (Leppäranta, 2005) and therefore has a significant impact on the ice drift in the farm. Furthermore, the wind direction influences the relative distance between the turbines encountered by the ice. Possibly changing the way the ice field interacts with the structures. In addition, the ice concentration is changed to see how this influences the ice action on the wind farm. Various other parameters can also influence the ice action and drift in a wind farm. Examples of these are the ice drift speed, ice thickness, floe size distribution and ridging. These are not taken into account as variable in this study but could be of interest for further research.

1.4. Research Questions

The main research question is stated as follows:

> *How is the ice loading on and ice drift around an offshore wind turbine influenced by it being part of an offshore wind farm?*

To answer this question, multiple sub-questions need to be answered first. Combining these will give an opportunity to answer the main research question. First, one needs to find an effective way to analyse the ice load time series. It is of importance to develop a method that makes it convenient to compare the loads experienced by each turbine. This leads to the first sub-question.

> Which methods can be developed to summarise and compare ice loads over time?

When this is defined, one can start to simulate different scenarios to see if there are consistent interaction patterns that can be identified. First, one will change the wind direction to change the relative distance between turbines and analyse how this influences the loads.

> How do the ice loads change over the wind farm for different wind directions?

After answering if a significant difference is observed, it is also of interest to see if there are differences for different ice concentrations. Therefore, this parameter is varied to answer the following question.

> What is the influence of the ice concentration on the ice loads experienced by each turbine in an OWF?

After doing so, one can use these simulations to see if a regressor predictor can be trained to predict the ice loads over the wind farm. Since the simulations are time consuming, it would be of interest to do an initial estimate using ML if these loads can be predicted accurately. Furthermore, analysing these regressors could help in validation or finding relationships between parameters. This leads to the final sub-question.

> In what ways can machine learning be used to accurately predict ice loads?

Answering these sub-questions will lead to answering the main research question.

1.5. Approach

To answer the main research question, data is generated using a simulation tool for ice loads. First, all simulation and import parameters are specified to ensure that a realistic simulation is performed. This ensures that the data obtained are based on realistic values. To guarantee that no numerical mistakes are included in these data, a filtering is done on the basis of theoretical values. The results from the different scenarios are compared using different new defined methods which summarises ice loads over time. Furthermore, the data is used to train multiple ML regressors to analyse their performance.

1.6. Scope

Since little is known about ice loads in OWFs, a scope is of importance to narrow down the abundant research possibilities. The main area of interest for this research will be the northern Baltic Sea. Within this area a significant growth in projects has been observed over the years and it has great potential for offshore wind (Hendrikse, 2024). Further relevant assumptions will be discussed throughout the thesis.

1.7. Thesis Outline

First, a literature study is performed that provides more insight into ice loads. This will include the driving forces, terminology, and failure mechanisms of the ice. Furthermore, the design of turbines under ice conditions is discussed. Also, different ways of representing loading time series are introduced to form a basis to answer the first sub-question.

Secondly, ice fields in the northern Baltic are analysed using image processing. In addition, insights on the properties of ice have been gained from literature studies. This gives the ability to simulate realistic ice conditions for the Northern Baltic. Combining this with discussing the simulation approach leads to the final simulations. The data gathered from these will be the main source of information to answer the main question.

Once the data is gathered, it will be analysed such that the sub-questions can be answered. First, all wind directions are discussed and compared for different ice concentrations. After obtaining all data, an introduction to different ML regressors is given. These different regressors are tested based on the obtained data and the performance is discussed.

2

Ice Classification and Loads

The main interest in this thesis is ice loads on structures. Therefore, in this chapter, the ice loads and important relevant aspects of these loads are discussed. Furthermore, different ways of analysing these loads are discussed on the basis of existing literature. The content of Section 2.1 and Section 2.2 is taken/edited from (Lambregts, 2024).

2.1. Ice Features and Classification

Types of ice can be categorised within certain subgroups and have different types of properties. All these types of ice are universally defined and subdivided into groups by the World Meteorological Organization (WMO) (JCOMM Expert Team on Sea Ice, 2009). In this work, the main focus will be on floating ice, or more specific sea-ice: *"Any form of ice found at sea which has originated from the freezing of sea water"*. The main investigated subgroups are the age of the ice and the ice feature. Where relevant definitions will be looked into and used throughout the report.

2.1.1. Classification of Ice by Age

Sea-ice can be present for different periods of time. The age of the ice can provide information about the properties of the ice. Two main categories are defined by the WMO (JCOMM Expert Team on Sea Ice, 2009):

- *"**First-year ice**: sea-ice of not more than one winter's growth, developing from young ice; thickness 30 cm - 2 m."*
- *"**Old ice:** sea-ice which has survived at least one summer's melt; typical thickness up to 3 m or more."*
  - *"**Second-year ice**: Old ice which has survived only one summer's melt; typical thickness up to 2.5 m and sometimes more."*
  - *"**Multi-year ice**: Old ice up to 3 m thick or more that has survived at least two summers' melt."*

In the Baltic Sea, only FY ice is present, as the ice does not survive the summer melt.

2.1.2. Classification by Location

Sea-ice can be classified into different categories, based on the distance from the shore it occurs. These zones are identified and shown in Figure 2.1.

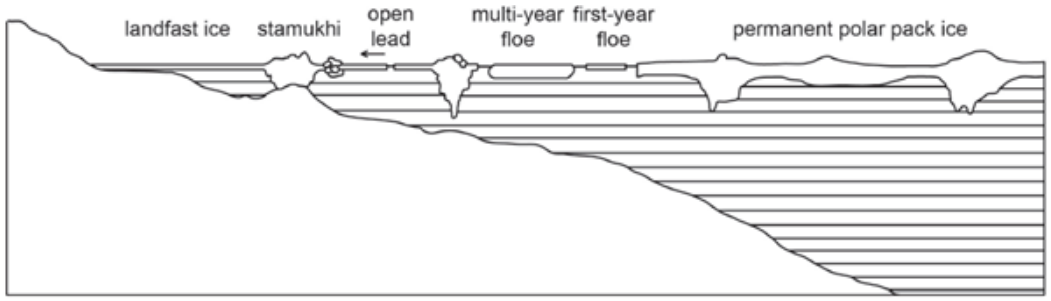

Figure 2.1: Classification of ice by position (Sanderson, 1988).

The most important types are listed below, all definitions are based on the WMO (JCOMM Expert Team on Sea Ice, 2009).

- ***"(Land) Fast Ice**: sea-ice which forms and remains fast along the coast. Fast ice may be formed in situ from sea water or by freezing of floating ice of any age to the shore, and it may extend a few metres or several hundred kilometres from the coast. Fast ice may be more than one year old and may then be prefixed with the appropriate age category."*
- ***"Floe**: Any relatively flat piece of sea-ice 20 m or more across."*
- ***"Drift/pack ice**: Term used in a wide sense to include any area of sea-ice other than fast ice no matter what form it takes or how it is disposed. When concentrations are high, i.e. 7/10 or more, drift ice may be replaced by the term pack ice"*

In this thesis Fast Ice will not be considered and the main focus will be on floes and drift/pack ice. Considered that the wind farms are located from a sufficient distance of the shore such that is is not connected to the shore.

2.1.3. Ice Features

The ice feature contains information about the thermomechanical properties and dimensions of the ice. Different features can lead to different ice actions. Therefore, this should be taken into account in the design process. The main features are defined below (JCOMM Expert Team on Sea Ice, 2009):

- *"**Level ice**: sea-ice which has not been affected by deformation."*
- *"**Deformed ice**: A general term for ice which has been squeezed together and in places forced upwards (and downwards)."*
  - *"**Rafted ice**: Type of deformed ice formed by one piece of ice overriding another."*
  - *"**Ridge**: A line or wall of broken ice forced up by pressure. May be fresh or weathered."*
  - *"**Hummock**: A hillock of broken ice which has been forced upwards by pressure."*
- *"**Standing floe**: A separate floe standing vertically or inclined and enclosed by rather smooth ice."*
- *"**Ram**: An underwater ice projection from an ice wall, ice front, iceberg or floe."*
- *"**Bare ice**: Ice without snow cover."*
- *"**Snow-covered ice**: Ice covered with snow."*

These ice features would naturally be occurring in ice fields. However, in this thesis it is assumed that most of these are not present. Mainly because of limited modelling possibilities and also to maintain uniformity when simulating. Interaction with these specific ice features could be further investigated in a later research stage.

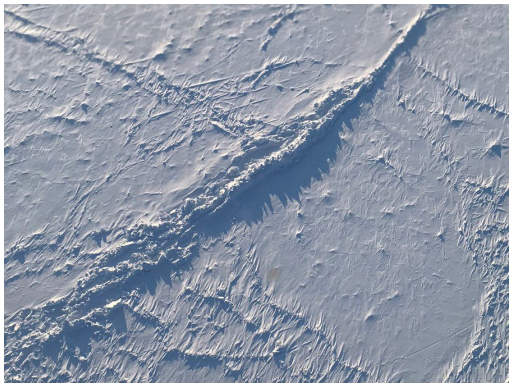

(a) A large sea-ice ridge (NASA Ice, 2018).

(b) Adélie penguins on ice floe in Newcomb Bay (Egan, n.d.).

Figure 2.2: Two examples of ice features.

2.1.4. Ice Parameters

The ice conditions can be defined using different kinds of parameters. Some of these are easily quantifiable while others might be more challenging to determine. However, that does not make these parameters less important. These parameters are used to describe the ice field that is present.

1. **Ice Concentration (SIC or C_i):** Refers to the area of sea-ice present relative to the total reference surface area.
2. **Ice Velocity (v_i):** The velocity of the ice depends mainly on the driving forces that act on it. The biggest contributions are generally made by wind and current velocity.
3. **Ice Thickness (h_i):** The thickness of the ice tells something about the age of the ice and the environmental conditions under which the ice is formed. This parameter is of great interest for defining the actions of ice in structures.
4. **Ridges:** The occurrence of ridges and the probability of ridging gives additional information about irregularities in the thickness of the ice field and the general conditions of the ice.
5. **Floe size and distribution:** This gives a description of the size range in which floes can occur and how often each size occurs.

2.2. Ice Action and Motion

Ice action is referred to as the force and structural response caused by ice moving into a structure. To understand the forces on the OWTs, the motion of the ice is important. The forces driving the ice eventually govern the type of load limiting mechanism occurring and can therefore influence the load experienced by the structure.

2.2.1. Ice Motion

Ice motion is caused by driving forces, which are important when calculating the ice action on a structure. The three primary natural driving forces are wind, current, and thermal expansion. A fourth (secondary) driving force is identified as a force from another ice mass that is driven by a primary force. The four driving forces are illustrated in Figure 2.3 (Sanderson, 1988).

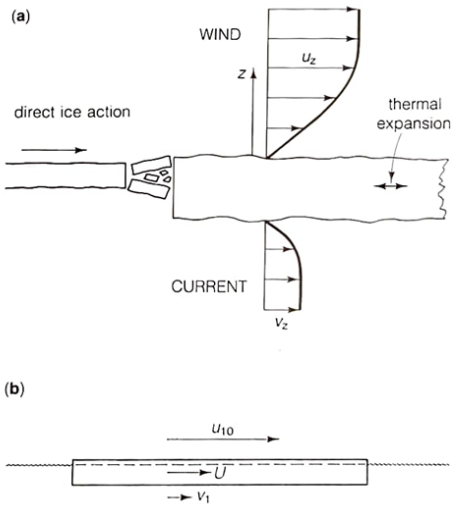

Figure 2.3: The four driving forces: (a) Primary: Wind, current and thermal expansion, and (b) Secondary: Ice mass (Sanderson, 1988).

Depending on the magnitude of these forces, the ice starts to move. The equation of motion, equation (2.1), is obtained using the stress in a 2D plane and integrating over the ice thickness. Two acceleration terms on the left-hand side are expressed in an Eulerian reference frame, the final term is the Coriolis acceleration (Leppäranta, 2005). On the right-hand side the external forces are expressed, consisting of: internal stress, shear stress from wind and current, the sea surface slope, and the atmospheric pressure.

$$\rho_i h_i \left[\frac{\partial \mathbf{u}}{\partial t} + \mathbf{u} \cdot \nabla \mathbf{u} + f\mathbf{k} \times \mathbf{u} \right] = \nabla \boldsymbol{\sigma} + \boldsymbol{\tau_a} + \boldsymbol{\tau_c} - \rho_i h_i g \boldsymbol{\beta} - h_i \nabla p_a \tag{2.1}$$

Solving this equation results in the motion of the ice subjected to a given forcing. The main contributions are air stress, internal friction, and water stress.

The shear stresses from wind and current can be determined using the velocity, drag factor, and density (Sanderson, 1988). Wind drag is determined on the basis of wind velocity at a height of 10 meters.

$$\tau_a = \rho_{air} C_a u_{10}^2 \tag{2.2}$$

The driving force of a current is determined in a comparable way. However, the viscosity of the water is higher and, therefore, the velocity at 1 m depth is taken.This results in Equation (2.3).

$$\tau_c = \rho_{water} C_c u_1^2 \tag{2.3}$$

2.2.2. Ice Loads

The highest ice load on a structure occurs when the ice crushes, also known as the limit stress mechanism. This force is defined as the global pressure multiplied by the nominal contact area Equation (2.4) (European Committee for Standardization, 2019).

$$F_G = p_G \cdot A_N = p_G \cdot h_i \cdot w \tag{2.4}$$

In general, the value of p_{G} is the most important for the design of structures. This pressure is influenced by the shape or aspect ratio of the contact area, the ice thickness, and the strength coefficient. It is an empirical formula and is defined in Equation (2.5).

$$p_G = C_R \left[\left(\frac{h_i}{h_1} \right)^n \left(\frac{w}{h_i} \right)^m + f_{AR} \right] \tag{2.5}$$

where

m is an empirical coefficient equal to -0.16;

n is an empirical coefficient, equal to $-0.50 + \frac{h_i}{5}$ for $h_i < 1.0$ m, and to -0.30 for $h_i \geq 1.0$ m;

$$f_{AR} = e^{-\frac{w}{3h_i}} \sqrt{1 + 5\frac{h_i}{w}} \tag{2.6}$$

The ice strength coefficient (C_R) is based on different regions and is defined in Table 2.1.

Table 2.1: Ice strength coefficient (C_R) in different regions (European Committee for Standardization, 2019).

$\mathbf{C_R}$ [MPa]	**Region**
2.8	Arctic FY and MY ice (e.g. Beaufort)
2.4	Subarctic (e.g. Okhotsk Sea — off north-east Sakhalin Island)
1.8	Temperate (e.g. Okhotsk Sea — Aniva Bay, North Caspian Sea, Cook Inlet, Baltic Sea, Bohai Sea)

2.2.3. Load Limiting Mechanisms

Three mechanisms have been identified that limit the forces of the ice (Frederking et al., 2014).

1. **Limit-Stress Mechanism**:
   - This is the force that results from the ice failing when in contact with the structure. It is caused by the driving forces being large enough to fail the ice.
   - Typically, this mechanism produces the highest ice force.
2. **Limit-Energy Mechanism**:
   - Occurs when the kinetic energy or momentum of the ice feature is dissipated, causing it to stop.
   - Key factors include the velocity and mass of the ice, resulting in the momentum.
3. **Limit-Force Mechanism**:
   - Occurs when the driving forces acting on the ice feature in contact with the structure are insufficient to cause failure. This can result in two different options.
     - The drive forces become small, making the ice floe stop.
     - The ice failure occurs at a location different from that of the structure wall. In this case, the ice fails through a ridging event.

These mechanisms have to be taken into account for each situation, and the active load limiting mechanisms contain information regarding the expected ice action.

2.2.4. Ice Failure Mechanisms

The way ice fails is dependent on how it interacts with the structure. Therefore, the type of structure matters; this can be a vertical or a sloping structure. In addition, the ice properties of the incoming ice, velocity, and thickness, also influence the type of failure. The main failure mechanisms are shown in Figure 2.4 (Sanderson, 1988).

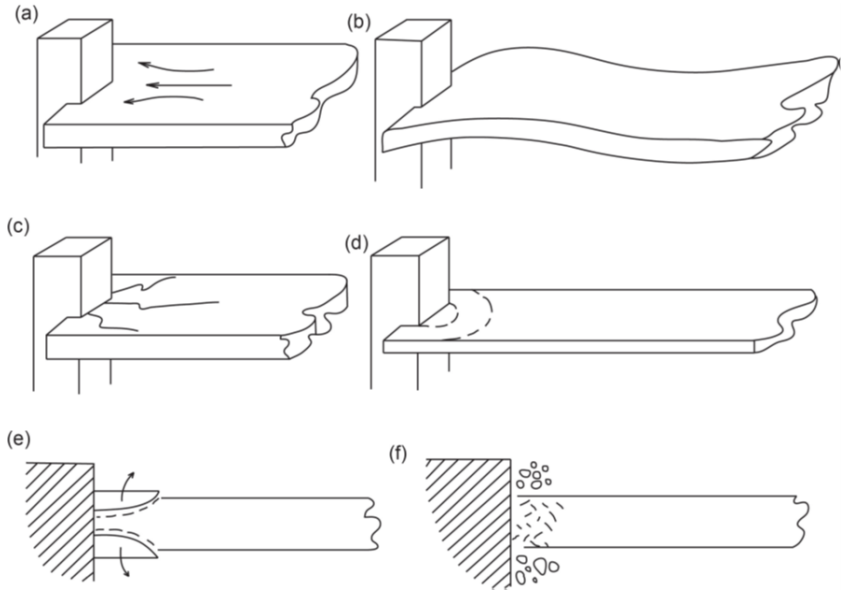

Figure 2.4: Failure modes for vertical structures a) Creep, b) Buckling, c) Radial cracking, d) Circumferential cracking, e) Spalling and f) Crushing (Sanderson, 1988).

All of these mechanisms represent failure modes against vertical structures. These are of importance for the ice action against the turbines.

2.3. Turbine Design Standards for Ice Loads

The main design code for structures in ice condition is ISO 19906 (European Committee for Standardization, 2019). For the general design of fixed offshore wind turbines, IEC 61400-3-1 is used (International Electrotechnical Commission, 2019). The latter defines the specific design conditions under ice conditions; see Figure 2.5. Relevant design situations are highlighted for this research scope.

Design situation	DLC	Ice condition	Wind condition	Water level	Type of analysis	Partial safety factor
Power production	D1	Horizontal load from temperature fluctuations	NTM $V_{hub} = V_r \pm 2$ m/s and V_{out} Wind speed resulting in maximum thrust	NWLR	U	N
	D2	Horizontal load from water level fluctuations or arch effects	NTM $V_{hub} = V_r \pm 2$ m/s and V_{out} Wind speed resulting in maximum thrust	NWLR	U	N
	D3	Horizontal load from moving ice at relevant velocities $h = h_{50}$ or largest value of moving ice.	NTM $V_{in} < V_{hub} < V_{out}$	NWLR	U	N
	D4	Horizontal load from moving ice at relevant velocities *Use values of h corresponding to expected history of moving ice occurring.*	NTM $V_{in} < V_{hub} < V_{out}$	NWLR	F	*
	D5	Vertical force from fast ice covers due to water level fluctuations	No wind load applied	NWLR	U	N
Parked	D6	Pressure from hummocked ice and ice ridges	EWM Turbulent wind model $V_{hub} = V_1$	NWLR	U	N
	D7	Horizontal load from moving ice at relevant velocities *Use values of h corresponding to expected history of moving ice occurring.*	NTM $V_{hub} < 0{,}7\ V_{ref}$	NWLR	F	*
	D8	Horizontal load from moving ice at relevant velocities $h = h_{50}$ or largest value of moving ice.	EWM Turbulent wind model $V_{hub} = V_1$	NWLR	U	N

Figure 2.5: IEC 61400-3-1 Design load cases (International Electrotechnical Commission, 2019).

The column ”type of analysis” refers to the type of loads that are investigated. Load cases D3 and D8 are the ultimate limit states. The maximum horizontal load is determined using Equation (2.4) from ISO19906. For the fatigue design load cases (D4 and D7) the loads over time are of main interest. This is done using the number of cycles of these loads and the corresponding magnitude.

The design code is mainly used in a later stage to determine which environmental and ice conditions are relevant for use for simulation. This will make the obtained data more relevant from a design perspective.

2.3.1. Fatigue Design

The fatigue design of offshore steel structures is described in DNV-RP-C203 (Det Norske Veritas, 2012). It can be determined using the S-N curve fatigue approach, based on the assumption of linear cumulative damage, commonly referred to as the Palmgren-Miner rule.

When the long-term stress range distribution is represented as a stress histogram, it consists of several constant stress range blocks, $\Delta\sigma_i$. Each block has a number of stress cycles, n_i. The damage criterion is given by:

$$D = \sum_{i=1}^{k} \frac{n_i}{N_i} = \frac{1}{\bar{a}} \sum_{i=1}^{k} n_i \cdot (\Delta\sigma_i)^m \leq \eta \tag{2.7}$$

where:

- D : accumulated fatigue damage
- $\bar{a}$: intercept of the design S-N curve with the log N axis
- m : negative inverse slope of the S-N curve
- k : number of stress blocks

- n_i : number of stress cycles in stress block i
- N_i : number of cycles to failure at constant stress range $\Delta\sigma_i$
- η : usage factor, defined as $1/$ Design Fatigue Factor

The amount of stress blocks used should be sufficient to obtain accurate results and should not be less than 20. When the damage equals one, the structure fails. The corresponding number of cycles from Equation (2.7) are determined by a rainflow count. This method is explained in more detail in Section 2.4.3.

2.4. Time Series Analysis of Ice Loads

There are numerous ways to describe and analyse the ice loads over time. Multiple methods are covered in this section. General statistics such as mean and standard deviation can already give valuable information about a time series. Three additional methods are introduced here giving the ability to describe the loads encountered over a longer time series more extensively. These methods will later be considered when comparing the ice loads for different scenarios.

2.4.1. Rayleigh Separation

This method is used to identify peak loads in a time series and is introduced by Kujala et al., 2009. Rayleigh separation involves comparing the minimum and maximum values. Initially, a Rayleigh separator value (ξ) is selected. Then, the first maximum value is identified from the time history. Maximum values are only identified once the time history values drop below the initially chosen Rayleigh separator value. If the time history values do not decrease below the chosen limit but instead rise again to exceed the initial value, the initial value is removed, and a new value is selected as the first maximum. An example of this method is illustrated in Figure 2.6.

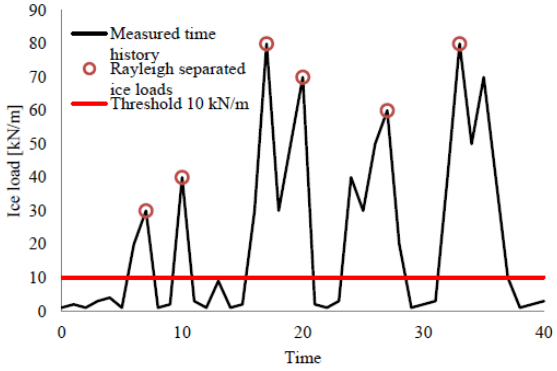

Figure 2.6: Rayleigh separation identifying peaks for an ice load event, using a separator value of $\xi = 0.5$ and a threshold of 10 kN/m (Suominen et al., 2017).

This method has previously been used for the analysis of full-scale data (Suominen et al., 2020) and for numerical simulations (Su et al., 2011). The Weibull distribution is found to fit the peak loads as the most accurate (Kujala et al., 2009) and suggests $c = 0.75$. It is described in the equations below, Probability Density Function (PDF, Equation (2.8)), Expected Value (E, Equation (2.9)), Variance (Var, Equation (2.10)) and the Cumulative Distribution Function (CDF, Equation (2.11)).

$$f(x) = c\lambda^c x^{c-1} e^{-(\lambda x)^c} \tag{2.8}$$

$$E[x] = \frac{1}{\lambda}\Gamma\left(1 + \frac{1}{c}\right) \tag{2.9}$$

$$Var[x] = \frac{1}{\lambda^2}\left\{\Gamma\left(1 + \frac{2}{c}\right) - \left[\Gamma\left(1 + \frac{1}{c}\right)\right]^2\right\} \tag{2.10}$$

$$F(x) = 1 - e^{-(\lambda x)^c} \tag{2.11}$$

Both λ and c can also be calculated using Equation (2.9) and Equation (2.10), given that the mean and variance of the data are known (Ochi, 1990). First, one can rewrite Equation (2.9), making λ a function of c as shown in Equation (2.12).

$$\lambda = \frac{\Gamma\left(1 + \frac{1}{c}\right)}{E[x]} \tag{2.12}$$

This formulation of λ can be invoked in Equation (2.10), resulting in c given the mean and variance of a dataset that solves Equation (2.13).

$$Var[x] = \left(\frac{E[x]}{\Gamma\left(1 + \frac{1}{c}\right)}\right)^2 \left[\Gamma\left(1 + \frac{2}{c}\right) - \left(\Gamma\left(1 + \frac{1}{c}\right)\right)^2\right] \tag{2.13}$$

This method combined with the Weibull distribution makes it possible to statistically describe the peak loads. The main parameters to select are the threshold and a Rayleigh separator value (ξ).

2.4.2. Power Spectral Density

The Power Spectral Density (PSD) displays the power of a signal, in this case the force, over a range of frequencies. In this case the ice force on the OWTs is a stationary stochastic process. Generally, the PSD can be determined given that $x(t)$ is a stationary random process (Lee et al., 2023). The corresponding self-correlation function $\gamma_{xx}(\tau)$ is expressed in Equation (2.14):

$$\gamma_{xx}(\tau) = E[x^*(t)x(t+\tau)] \tag{2.14}$$

where E denotes the statistical average.

Using the Wiener-Khintchine theorem, the Fourier Transform of the autocorrelation function yields the power spectrum:

$$\Gamma_{xx}(F) = \int_{-\infty}^{\infty} \gamma_{xx}(\tau) e^{-j2\pi Ft} dt. \tag{2.15}$$

It is important to note that there are different approaches to computing a PSD, three relevant ones will be discussed. The first method is known as the Fast Fourier Transform (FFT). This method computes the Discrete Fourier Transform of a time series. As the name already suggests, it is a faster method for performing a power spectrum analysis and is computationally efficient (Cochran et al., 1967). Another method applied to analyse a PSD of the ice load is the Blackman & Tukey method (Lee et al., 2023). This method creates a more smooth PSD using a moving weighted average and a Hamming process. Another common way to describe a PSD function is the Neumann spectrum (Neumann, 1952). This method has previously been applied for ice load spectra (Yue et al., 2007). This makes it the preferred method for computing a PSD for a time series of ice load.

2.4.3. Rainflow Counting

This method is used mainly for the analysis of structural component fatigue. The rainflow counting method is a widely accepted technique for characterising stress cycles in irregular load histories (Amzallag et al., 1994). It was developed to systematically analyse load time series into individual stress cycles. In the literature, multiple rainflow methods are proposed using 3 or 4 points (Lee et al., 2011). These methods are the most computationally efficient.

An example of such a four-point algorithm by Amzallag et al., 1994 is shown in Figure 2.7.

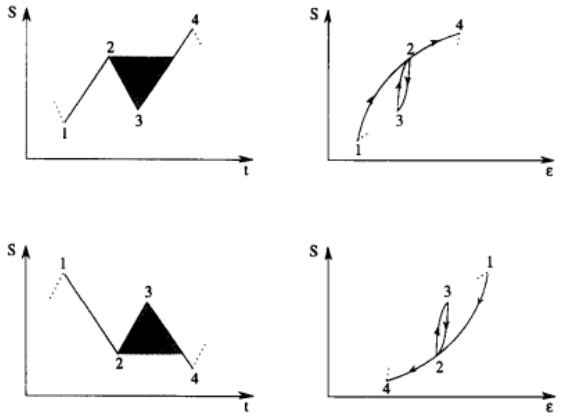

Figure 2.7: Cycle extraction principle using the Amzallag et al., 1994 algorithm.

The term ”rainflow” originates from an analogy between this method and the way rainwater flows down the edges of a pagoda roof (Lee et al., 2011). The general rainflow cycle counting procedure can be described as follows.

1. Rotate the load history by 90° so that the time axis is oriented vertically downward, making the load-time history resemble the roof of a pagoda.
2. Imagine rainwater flowing from each successive extremum point.
3. A loading reversal (half cycle) is defined by permitting each rainflow to continue to descend along these roofs until:
   (a) It encounters a larger peak (or a smaller trough) on the opposite side.
   (b) It intersects a previously descending flow.
   (c) It extends beyond the roof.
4. Identify complete hysteresis loops (cycles) by matching the counted reversals.

This general procedure is illustrated in Figure 2.8.

(a) Load time series.

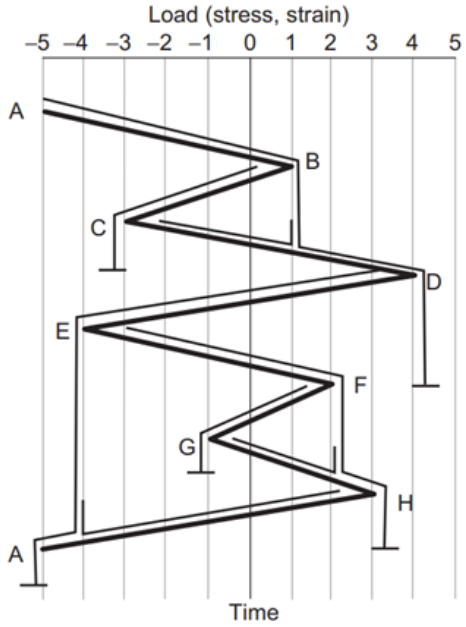

(b) Rainflow method applied on the load time series.

Figure 2.8: General rainflow procedure (Lee et al., 2011).

3

Analysing Ice Fields

The main parameters to analyse for a broken ice field are the thickness of the ice, mechanical properties, and the floe size distribution (FSD). In this section, all of these will be covered and will be used as input for the simulations. The main area of interest is the northern Baltic Sea.

3.1. Ice Thickness

The thickness of the ice strongly influences the forces on a structure, as can be seen in Equation (2.4). In the Baltic Sea, only first year ice is present, since all the ice melts during summer. This limits the thickness of the ice since it has to grow every winter over again. In this study, the ice field is assumed to have no ridges and a uniform ice thickness. Mainly because of simulation limitations and to create a uniform force relationship based on the ice thickness.

The thickness of ice in the Gulf of Bothnia has been studied in various locations by Tikanmäki, 2024. These locations with corresponding ice thickness data are shown in Figure 3.1.

(a) Studied locations in the Baltic.

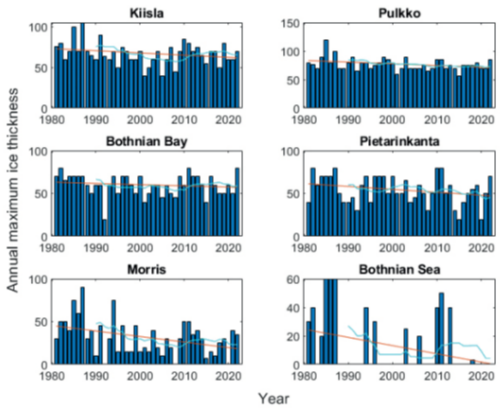

(b) Ice thickness annual maximum from 1980-2020, the red line indicates the regression.

Figure 3.1: Study locations with the obtained ice thickness data (Tikanmäki, 2024).

From these figures, it can be clearly seen that the maximum ice thickness can vary significantly over the years. Therefore, a representative ice thickness must be determined when designing structures in this area. The 50-year maximum ice thickness has been determined for all these locations. When determining this peak value, the selected time period can significantly influence the maximum thickness. This is shown in Table 3.1 for different reference periods.

Table 3.1: 50-year maximum ice thickness and trends at various locations (Tikanmäki, 2024).

Location	50-year max ice thickness (1981–2022)	50-year max ice thickness (1981–2010)	50-year max ice thickness (1981–2000)	50-year max ice thickness (1993–2022)	50-year max ice thickness (2003–2022)	Trend in annual maxima (cm/10 years)
Kisla	96	101	115	84	86	-2.7
Pulkko	105	113	115	94	95	-3.0
Bay of Bothnia, middle	79	76	70	82	86	-1.4
Pietarinkanta	84	85	81	82	85	-3.4
Morris	84	104	105	73	83	-6.5
Bothnian Sea, middle	62	64	62	50	52	-5.7

Based on IEC61400-3-1, shown in Figure 2.5, the 50-year thickness or the expected historic thickness should be used for the design. In this case using the 50-year thickness is a more conservative thickness, since the general trend is descending. Therefore, from a design and safety perspective, this value should be used. Based on the areas of interest analysed in Section 3.2, the ”Bay of Bothnia middle” is the best reference location. From the table, the most conservative value for a 50-year maximum is 86 cm. This value will be used in the simulations.

3.2. Floe Size Distribution

An ice field can consist of level ice or deformed ice, forming a broken ice field. The main focus of this thesis is on load analysis in broken ice fields. These can be described using a floe size distribution (FSD). Multiple studies have been conducted to analyse FSDs (Herman, 2010; Horvat & Tziperman, 2017; Rothrock & Thorndike, 1984), some of which consider thermodynamic properties and ice thickness, while others focus solely on size distribution. The floe sizes can, in general, be well described using a power law (Herman, 2010). Various experiments and approaches have been used to analyse the power law factor, α, for different locations and ice floe sizes observed, some of these results are shown in Table 3.2.

Table 3.2: Observed power-law sea-ice floe-size distributions (Herman, 2010).

Study	α	Ice Field
Rothrock and Thorndike, 1984	1.7–2.5	Ice floes larger than 100 m
Matsushita, 1985	2.16	Ice floes larger than 100 m
Kergomard, 1989	1.0–1.8	1.0: internal ice zone 1.8: marginal ice zone
Lensu, 1990	1.36, 1.56	Values obtained with two methods
Holt and Martin, 2001	1.8–2.9	
Toyota and Enomoto, 2002	2.1–2.5	
Weiss, 2003	2.5	
Inoue et al., 2004	1.5–2.1	1.5: internal ice zone 2.1: marginal ice zone
Toyota et al., 2006	1.15–1.87	α larger for larger floes
Steer et al., 2008	1.83–2.36	Floe width 20–50 m
	0.91–0.94	Floe width 2–20 m

A FSD is in general displayed using a log-log plot; the distribution can either be cumulative or non-cumulative. The latter results in a straight line, while the cumulative plot will result in a concave downward line (Denton & Timmermans, 2022).

The non-cumulative power law is generally described by Equation (3.1).

$$p(x) = C \cdot x^{-\alpha} \tag{3.1}$$

Given that the distribution has an upper limit (x_{max}) and a lower limit (x_{min}), C is obtained by integrating $p(x)$ and solving for $p(x) = 1$, Equation (3.2). This equation holds under the assumption that $\alpha > 1.0$

(Buckley et al., 2024). The complete derivation is given in Appendix B.

$$C = \frac{1-\alpha}{x_{max}^{1-\alpha} - x_{min}^{1-\alpha}} \tag{3.2}$$

Furthermore, the standard error for α is determined using Equation (3.3) by Clauset et al., 2009, given that n represents the sample size.

$$\sigma = \frac{\alpha - 1}{\sqrt{n}} + O(1/n) \tag{3.3}$$

This will be used when the distribution is analysed to determine what error can be expected.

3.3. Image Processing

The ice fields at different locations can be analysed using image processing. Accurately processing and analysing these images is a complex procedure. Different advanced methods are developed for different purposes (Denton & Timmermans, 2022; Zhang & Skjetne, 2014; Zhou et al., 2023). In this study, the method and algorithm covered in Zhang and Skjetne, 2014 is used. This code is open source and is obtained from Zhang and Skjetne, 2018. It uses multiple techniques for edge detection and gives the ability to adjust the algorithm. The main steps of this algorithm are as follows.

1. **Ice Pixel Extraction**
    - Ice pixels are extracted using a threshold; this method mainly identifies the ”light Ice”. This is bright white ice detected from the threshold used.
    - To determine the difference between water and ”Dark Ice” a k-means method is used. Dividing the image into different clusters. The water is considered to be identified by the cluster with the lowest average intensity.
    - The darker ice is extracted by subtracting the threshold method from the k-means method.
2. **Ice Edge Detection**
    - One of the main challenges is separating floes that are near or partially connected. Initially, these boundaries are not always identified.
    - A GVF snake algorithm is used to detect these edges. This method identifies weaker boundaries in the greyscale image and is an extension of the algorithm from Kass et al., 1988.
3. **Ice Shape Enhancement**
    - Due to noise, there might be holes or small ice pieces inside a floe. The output of the previous steps generally gives a rough shape identification.
    - To shape the floes, morphological cleaning (Soh et al., 1998) is applied to smooth contours.
    - The morphological cleaning is combined with a disk shape procedure (Gonzalez et al., 2003) resulting in the final shape of the identified floes.

The data obtained from this processing method are the area, position, vertices, and perimeter of all identified floes. These values are given in units of pixels; these need to be transformed into meters before the FSD can be obtained. The Copernicus Browser provides a deg/px resolution in both latitude and longitude. These are used for conversion to metric units.

For latitude, a commonly accepted approximation is that one degree corresponds to approximately $111\,320$ meters. If one denotes the latitude resolution as a generic variable r_{lat} (in deg/px), then the conversion for latitude is given by:

$$\text{Meters per pixel (lat)} = r_{\text{lat}}\,\text{(deg/px)} \times 111\,320\,\text{(m/deg)}.$$

For longitude, the linear distance corresponding to one degree varies with latitude ϕ (northern Baltic Sea $\approx 64^\circ$ N). At any latitude, one degree of longitude is approximately:

$$1^\circ \text{ longitude} \approx 111\,320 \times \cos(\phi)$$

Thus, if r_{long} represents the longitude resolution in deg/px, the conversion for longitude is:

$$\text{Meters per pixel (long)} = r_{\text{long}}\,\text{(deg/px)} \times 111\,320\,\text{(m/deg)} \times \cos(\phi).$$

These conversion factors and methods are based on Snyder, 1987.

3.4. Satellite Image Analysis

In this section, the previously covered image processing algorithm is used to extract a FSD based on satellite data. sea-ice can be observed using the Sentinel-2 satellite. These images can be extracted using the Copernicus Browser. In this application, one can select an area of interest and filter dates based on the cloud coverage. To obtain clear images, a limit of 5% cloud coverage is used. As mentioned in the previous section, it also provides a resolution to transform pixels into meters. Three different areas are analysed with different sizes to gain general insight. The FSDs of these will be compared and used to determine the simulation input. The sizes of these areas are approximately 6100 km^2, 2500 km^2 and 1500 km^2.

The most northern part of the Baltic is analysed for this study in the area around Vaasa, Oulu, Luleå, and Umeå.

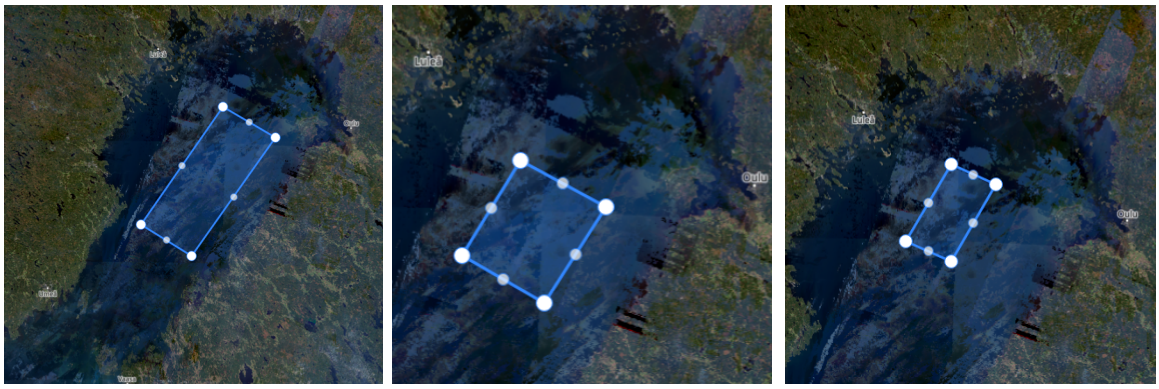

(a) 6100 km^2 study area. **(b)** 2500 km^2 study area. **(c)** 1500 km^2 study area.

Figure 3.2: The three different sized areas of interest for studying the FSD.

For each area of interest, the ice field for five different years at a different dates is analysed. Note that 2020 is not included in this analysis; this year had no clear ice field present and therefore not included. The corresponding images of the ice fields are shown in Appendix A. These images are processed using the image processing algorithm described in Section 3.3 from (Zhang & Skjetne, 2014). The MCD is calculated on the basis of the shape and size of the floes using the data from the vertices obtained from the image processing.

This data is fitted using a non-cumulative power law to determine the power law coefficient. The fit is performed using the power law Python package (Alstott et al., 2014) similar to Buckley et al., 2024. The fit is done using logarithmically spaced bins, 10 bins are used ensuring that each bin consists of at least 2 data points (Denton & Timmermans, 2022). This results in the following FSDs, Figure 3.3.

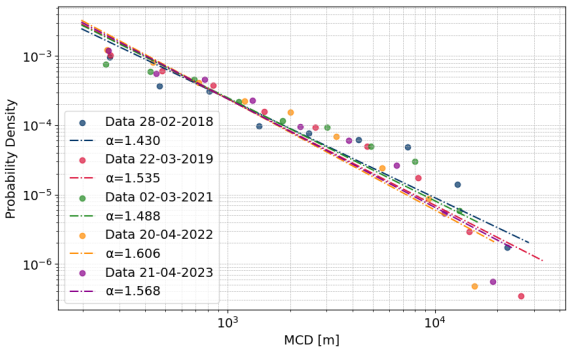

(a) FSD for the 6100 km^2 study area.

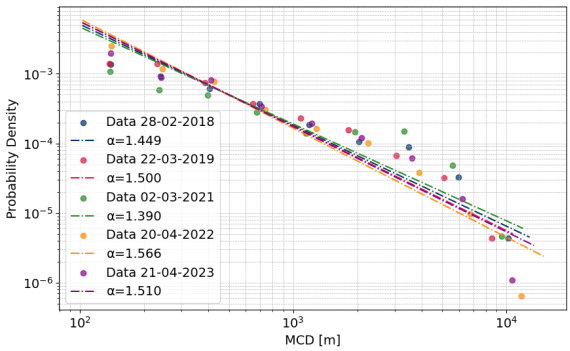

(b) FSD for the 2500 km^2 study area.

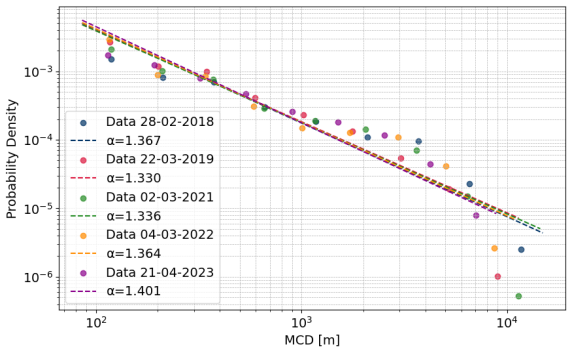

(c) FSD for the 1500 km^2 study area.

Figure 3.3: Three different FSD based on different areas of interest with different sizes.

From these figure one can observe that generally the larger floes are over-fitted by the power law. Various reasons can be given for this observation. First, one uses a specified area of the ice that might cut off larger floes. Therefore, their full size is not captured, resulting in a possible lower probability of large floes. Furthermore, the size distribution will never follow an exact power law and, therefore, offsets are to be expected. Moreover, the image processing algorithm can also influence the accuracy of these floes being detected. Generally, all obtained floe data are fitted with sufficient accuracy for this purpose.

A statistical summary of all distributions of the studies is given in Table 3.3. This table will be used to compare the results obtained and conclude the characteristics of the ice field present in the Baltic that can be used for simulations.

Table 3.3: Statistical summary for the floe size distribution obtained from image processing, all data is describing the Mean Caliper Diameter (MCD) in meters.

Area	Date	Mean	Min	Max	Std.	α	Standard Error
6100 km^2	28-02-2018	4184.43	196.54	28358.04	4650.87	1.43	0.02
	22-03-2019	2426.03	196.54	33050.03	3180.56	1.54	0.01
	02-03-2021	2851.06	196.54	16225.62	3121.85	1.49	0.02
	20-04-2022	1829.86	196.54	19290.50	2238.63	1.61	0.01
	21-04-2023	2107.57	196.54	23861.70	2659.24	1.57	0.01
2500 km^2	28-02-2018	1855.15	102.52	12869.49	2104.13	1.45	0.02
	22-03-2019	1446.82	102.52	10734.11	1730.92	1.50	0.01
	02-03-2021	2276.97	102.52	11961.61	1971.86	1.39	0.02
	20-04-2022	1202.45	102.52	14963.21	1616.53	1.57	0.01
	21-04-2023	1386.55	102.52	13477.53	1644.58	1.51	0.01
1500 km^2	28-02-2018	2002.35	85.72	14897.39	2278.17	1.41	0.02
	22-03-2019	1059.13	85.72	11372.01	1318.85	1.54	0.01
	02-03-2021	1489.45	85.72	14499.88	1732.18	1.46	0.01
	04-03-2022	1499.59	85.72	10906.71	1697.31	1.48	0.02
	21-04-2023	1369.40	85.72	8851.51	1492.07	1.47	0.01

The minimal MCD changes for each studied area; this value is limited by the number of pixels in the image. Since the resolution of all images is similar, the obtained minimal MCD decreases for a smaller ice field area. For the 6100 km^2 area, one can clearly see that the maximal MCD is significantly higher compared to the other two. This confirms that, for smaller areas of interest, large floes are less likely to occur or are cut out of the image. It also shows that there is a higher variability of floe sizes on the basis of the standard deviation being larger. Furthermore, the standard error for all analysed ice fields is consistent and between 0.01 and 0.02.

The fitted power law factors, α, vary both over the years and for different areas analysed. Therefore, a statistical analysis is performed on the observed years and different areas. This data is summarised in Figure 3.4.

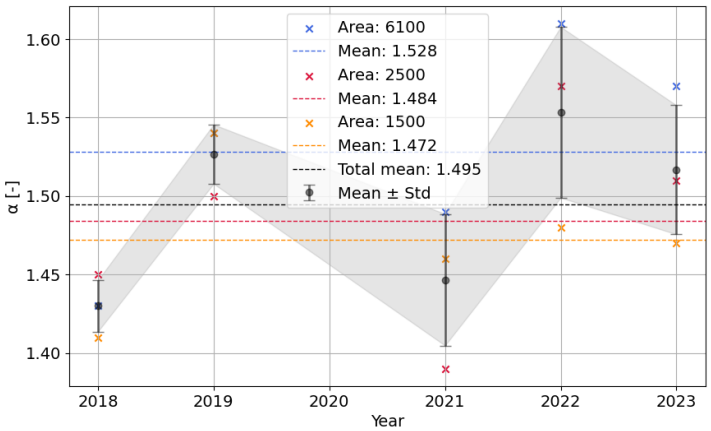

Figure 3.4: Statistical analysis of the power law exponent α over the years for different areas of interest.

In this figure, the mean and standard deviation for α for each year are first determined. One can notice that in general the mean value of α decreases over a decreasing area. Furthermore, in 2018 and 2019 the coefficients are close to one another, while for the other three years a more noticeable difference is observed. The total mean of all values is used to generate the ice field for simulations. This coefficient is equal to $\overline{\alpha} = 1.495$ and is in line with the expected range found in the previous literature Table 3.2.

3.5. Ice Properties

The properties of the ice define the behaviour of the ice and affect the forces that will be exerted on the turbines. In this section, the main parameters of importance for modelling the ice will be discussed. These final parameters are shown in Table 3.4, each value will be discussed on the basis of the available literature. As mentioned previously, only first-year ice is present in the Baltic. Therefore, all properties will be based on FY ice and will assume no ridges.

Table 3.4: Ice Properties for First Year (FY) ice in the Northern Baltic.

Parameter	Value
Ice density [$\mathrm{kg/m^3}$]	910
Crushing specific energy [Pa]	$2.0 \cdot 10^6$
Young's modulus [Pa]	$5.0 \cdot 10^9$
Poisson's ratio [-]	0.3
Fracture toughness [$\mathrm{Pa \cdot m^{0.5}}$]	$115 \cdot 10^3$
Flexural strength [Pa]	$1.0 \cdot 10^6$
Tensile strength [Pa]	$5.0 \cdot 10^5$
Friction coefficient ice-ice [-]	0.15
Friction coefficient ice-structure [-]	0.14
Friction coefficient ice-wall [-]	0.15
Water skin friction coefficient [-]	$3.0 \cdot 10^{-3}$
Water form drag coefficient [-]	$(0.001, 0.001, 0.5)$
Ice-air skin friction coefficient [-]	$0.6 \cdot 10^{-3}$

Ice Density

The density of the ice is important since it determines the weight of the ice. Hence, it influences the momentum of the ice. It is also important when a buoyancy force acts on a structure such as a ship. In the application for loads on monopiles, the ice is not able to be submerged under the structure. Therefore, the main importance for this application is the weight and corresponding momentum (Timco & Weeks, 2010).

The density of ice can be determined with four different techniques: mass/volume, specific gravity, displacement, and using the freeboard combined with the ice thickness. A summary of the results obtained using different methods is given in Table 3.5. Based on these results, an average ice density of $\rho_i = 0.91\ \mathrm{Mgm^{-3}}$ ($\rho_i = 910\ \mathrm{kgm^{-3}}$) is obtained (Timco & Frederking, 1996).

Table 3.5: Density measurements of first-year sea-ice from various studies (Timco & Frederking, 1996).

Investigator	Measurement Technique	Density Range (Mg m^{-3})	Density (above waterline) (Mg m^{-3})	Density (below waterline) (Mg m^{-3})	Brine Drainage
(Malmgren, 1927)	–	0.914 to 0.924	–	0.914 to 0.924	NO
(Butkovich, 1956)	mass/volume	0.78 to 0.92	0.85 to 0.92	0.88 to 0.92	YES
(Weeks & Lee, 1958)	mass/volume	0.77 to 0.96	–	0.86 to 0.91	YES
(Langleben, 1959)	mass/volume	0.84 to 0.90	0.84 to 0.90	0.90 to 0.93	NO
(Pounder & Little, 1959)	specific gravity	0.81 to 0.91	–	–	YES
(Pounder & Stalinski, 1960)	specific gravity	0.943 ± 0.02	–	–	YES
(Brown & Kingery, 1963)	specific gravity	0.92	–	–	NO
(Langleben & Pounder, 1963)	displacement	0.884 to 0.91	0.884	0.91	YES
(Kohnen, 1972)	mass/volume	0.90 to 0.92	–	0.90 to 0.92	NO
(Nakawo, 1983)	displacement	0.88 to 0.92	0.88 to 0.91	0.90 to 0.92	NO
(Timco & Frederking, 1983)	mass/volume	0.904	–	0.904	NO
(Sinha, 1984)	mass/volume	0.90	0.90 to 0.91	–	NO
(Sinha, 1986)	mass/volume	0.90 to 0.91	0.90 to 0.91	0.90 to 0.91	NO
(Timco & Frederking, 1986)	mass/volume	0.76 to 0.89	–	–	YES
(Urabe & Inoue, 1988)	mass/volume	0.75 to 0.88	0.75	0.88	YES

Crushing Specific Energy

This parameter represents the compressive strength of the ice. In general, ice failing in compression gives the highest force on the structure. The compressive strength has been measured in numerous studies. It can depend on internal and external factors. Some of these internal factors are temperature, density, and salinity. External parameters are mainly related to the test setup and can be adjusted when testing the ice. Examples of these are sample size, loading rate, and loading direction.

The uniaxial compressive strength of first-year sea-ice has been studied by (Timco & Frederking, 1990, 1991). From this, a formula for the uniaxial compressive strength is derived. For vertical structures that interact with ice, a horizontally loaded ice column is of interest. The uniaxial strength in this case is given by Equation (3.4).

$$\sigma_c \;=\; 37\,(\dot{\epsilon})^{0.22}\Big[1 \;-\; \sqrt{\tfrac{v_T}{270}}\Big], \tag{3.4}$$

Here, $\dot{\epsilon}$ is the strain rate, and v_T is the total porosity in parts per thousand (‰ or ppt). In general, a value range of 0.5 to 5 MPa is obtained using either the above equation or by performing tests (Timco & Weeks, 2010).

In the software used to simulate the interaction of the ice, a value of 2 MPa has previously been used to model the interaction of the ice structure (Lubbad, Løset, et al., 2018a, 2018b; Tsarau et al., 2018). The compressive strength in such simulations generally depends on the loading/strain rate; however, this factor is not taken into consideration in the software. Therefore, this study will use the same value as reported in previous literature.

Young's Modulus

This parameter describes the ratio between stress and strain, also known as the Elastic Modulus (E). It can be determined with in situ seismic determinations. Measurements of Weeks and Assur, 1968 vary from approximately 1.7 GPa to 5.7 GPa when measured by flexural waves, and from 1.7 GPa to 9.1 GPa when measured by body wave velocities.

In various studies a significant increase in the elastic modulus value E has been found with decreasing temperature and brine volume (Anderson, 1958; Peschanskii, 1960). This is relevant for the Baltic Sea because it has a lower salinity compared to the arctic oceans.

The elastic modulus of sea-ice can be approximated by a linear relationship with respect to the volume of the brine v_b, Equation (3.5) (Timco & Weeks, 2010).

$$E = 10 \;-\; 0.0351\,v_b \quad \text{(GPa)}. \tag{3.5}$$

Since accurate data on the brine volume for Baltic sea-ice is not available, the default value of 5 GPa is used.

Poisson's Ratio

Poisson's ratio (μ) represents the ratio of lateral strain to longitudinal strain in a homogeneous material under uniaxial loading. Despite its importance, little is known and investigated about this parameter. In sea-ice, viscoelastic effects influence Poisson's ratio, similar to Young's modulus. Therefore, unless measured at high frequencies to capture only the elastic response, the values obtained should be referred to as the effective Poisson ratio (Timco & Weeks, 2010).

High-frequency measurements of sea-ice are typically conducted using seismic methods on ice covers or ultrasonic measurements of ice cores. Langleben and Pounder, 1963 measured pulse velocity and resonance in sea-ice cores, applying elasticity theory to calculate the Poisson ratio, obtaining an average value of 0.295 ± 0.009. In previous studies using SAMS a value of 0.3 is used, based on the obtained measurement this value is validated.

Fracture Toughness

Fracture toughness (K_c) is a material property that quantifies the stress needed to propagate a crack of known size. It is related to the strain energy release rate (G) by the equation for plane strain:

$$K_{1c}^2 = \frac{GE}{(1-\mu)^2} \tag{3.6}$$

where E is Young's modulus and μ is Poisson's ratio. The "1" in the equation refers to mode 1 failure, where the crack surfaces open in a direction normal to the crack faces.

The fracture toughness of first-year sea-ice has been extensively studied by various researchers (DeFranco et al., 1991; Shen & Lin, 1988; Timco & Frederking, 1983; Urabe et al., 1980). This toughness is influenced by factors such as loading rate and ice type, with temperature and grain size showing minimal impact. Typical values for K_{1c} in small samples range around 115 kPa·m$^{0.5}$ (Timco & Weeks, 2010). Therefore, this value is used within the simulations.

Flexural Strength

This parameter is an important parameter for ice failure in bending. The flexural strength can be obtained using two approaches: simple beam testing and cantilever beam testing. Testing the flexural strength creates a non-uniform stress field in the sea-ice. Assumptions are needed regarding the behaviour of the material to obtain the flexural strength.

The measured flexural strength can be influenced by the loading rate, the size of the beam, the type of test, and the direction of loading. Furthermore, Timco et al., 1994 showed that the data for first-year sea-ice could be described by Equation (3.7).

$$\sigma_f = 1.76 \exp\left(-5.88\sqrt{v_b}\right) \tag{3.7}$$

Where σ_f is the fracture stress and v_b represents the volume fraction of the brine. Generally, the flexural strength of sea-ice is approximately 1 MPa and can decrease as the volume of the brine increases. Considering that the Baltic Sea has low salinity, a flexural strength of 1 MPa will be used (Timco & Weeks, 2010).

Tensile Strength

The tensile strength represents the maximum tensile stress the ice can withstand before failure. Large-scale observations of sea-ice frequently reveal numerous open leads, which form as a result of tensile failure. This property plays a role in the prediction of both large-scale ice dynamics and local ice conditions. It is also a critical factor to understand how ice fails when it interacts with offshore structures.

Only a limited number of studies have investigated the tensile strength of first-year sea-ice (Dykins, 1967; Kuehn et al., 1990; Menge & Jones, 1993; Peyton, 1963, 1966). In general, performing these tensile strength tests is time-consuming and requires precise test setups. The tensile strength for the first year ice ranges between 0.2 and 0.8 MPa for ice sheet that are loaded in horizontal direction (Timco & Weeks, 2010). Therefore, in this study, a value of 0.5 MPa is used since it represents the mean value of this range.

Friction Coefficient

Different friction coefficients are used as input to describe the interaction of ice-ice and ice-structure. Additionally, ice-wall friction describes the friction experienced when using a confinement wall.

Measurements have been performed to analyse the friction between the ice sliding on itself. From these experiments, it shows that for this interaction, Coulomb's law is valid. Hence, shear stress increases proportionally with normal stress at the interface, whereas cohesion has minimal impact on friction resistance. The friction coefficients obtained from the smooth ice range from $\mu = 0.15 - 0.76$ (Schulson & Fortt, 2012). In this study, the lowest value for ice-ice friction, $\mu = 0.15$, is used in the simulations.

The ice-structure friction is mainly used when ice moves along a sloping structure. Frederking and Barker, 2002 tested the friction of sea-ice on steel using different speeds. From this study, it is found

that the coefficient is greatly dependent on the ice speed. Furthermore, the use of painted steel resulted in significantly lower friction compared to the use of corroded steel. Since the monopile is not a sloping structure, this parameter will not have a significant impact on the accuracy of the simulations. However, it is decided to use the value obtained from the corroded steel, which results in a kinetic friction coefficient of 0.14.

The ice-wall coefficient refers to the friction experiment when using a confined domain. This confinement can represent a coastal boundary or it can represent the ice field out of the simulated domain. Since this value has not been particularly studied for this software, the default value used in (Lubbad, Løset, et al., 2018a, 2018b; Tsarau et al., 2018) will also be used in this study.

Water and air skin friction

Water skin friction is a shear force resulting from the viscosity of water and air. These forces were previously defined in Equation (2.2) and Equation (2.3). The drag coefficients C_a and C_c are mainly dependent on the roughness of the surface. In the Arctic, these values are found to be $C_w = 5 \cdot 10^{-3}$ and $C_a = 1.2 \cdot 10^{-3}$ [-]. However, in the Baltic, these values tend to be 25-50% smaller (Leppäranta, 2011). Furthermore, the ratio $C_a/C_c \approx 0.19$ is found by Leppäranta and Omstedt, 1990. Given that no ridges are used for this simulation, C_a is assumed to be 50% lower than the values found in the Arctic. This results in $C_a = 0.6 \cdot 10^{-3}$ [-], preserving the approximate ratio found for the Baltic, $C_c = 3 \cdot 10^{-3}$ [-] is determined.

Water form drag coefficient

The force exerted on the ice floe by water is not only dependent on the skin friction. It also consists of the drag form of the floe edges and the form drag of the keel from ice ridges. Since no ridges are assumed in this simulation, this value is zero.

The form drag acting on the floe edge can be described as the normal force acting on the leading face of a floe while it moves. Its coefficient can be expressed with Equation (3.8).

$$\begin{aligned} \tau_e &= \frac{F_e}{L + D_s} = \frac{\rho_w C_e D}{2(L + D_s)} (V_i - V_w)^2 \Gamma_e \\ \Rightarrow C_w^e &= \frac{\tau_e}{\rho_w (V_i - V_w)^2} = \frac{C_e A D}{2L} \left[1 - \left(\frac{A}{1 - A} \cdot \frac{D}{L} \right)^{1/2} \right]^2 \end{aligned} \tag{3.8}$$

In this equation, C_e represents the form drag on a single floe edge, A represents the ice concentration and D/L is the floe aspect ratio. Using $C_e = 1.0$ (Hoerner, 1965), the range of the form drag coefficient $C_w^e = 10^{-2} - 10^{-4}$ is found for an ice concentration of 70-90%. The smaller the aspect ratio D/L the higher this coefficient is (Lu et al., 2011). The ice field in the simulation consists mainly of medium to large floes, therefore $C_w^e = 10^{-3}$ is used. This value is valid in both the x and y directions. However, for a movement in the z direction, this drag will be significantly larger. For this a value of 0.5 is used as previously used in Lubbad, Løset, et al., 2018a.

4

Simulation Approach

In this chapter, the software that is used to simulate the ice loads on the OWTs is introduced. Furthermore, the Offshore Wind Farm Layout used in the simulations is discussed. Finally, the simulation input is covered. The ice and environmental conditions are based on the northern Baltic Sea. In Section 4.1 and Section 4.2, parts of Lambregts, 2024 are used and adjusted for this specific case.

4.1. Simulator for Arctic Marine Structures - SAMS

The software used to model the ice-OWF interaction is called SAMS (Lubbad, Løset, et al., 2018a). It is developed by Arctic Integrated Solutions AS (ArcIso), a spin-off from NTNU. By incorporating a novel implicit time-stepping approach and an enhanced contact model, SAMS enables general viscoelastic interactions. It categorises contacts into two types: rigid and compliant. In the case of rigid contacts, no upper limit is used on the contact force, making the model computationally efficient. Although this approach provides a reliable estimate of the average contact force, it does not capture the exact details of contact behaviour. Figure 4.1 shows the main properties and modules of the SAMS software.

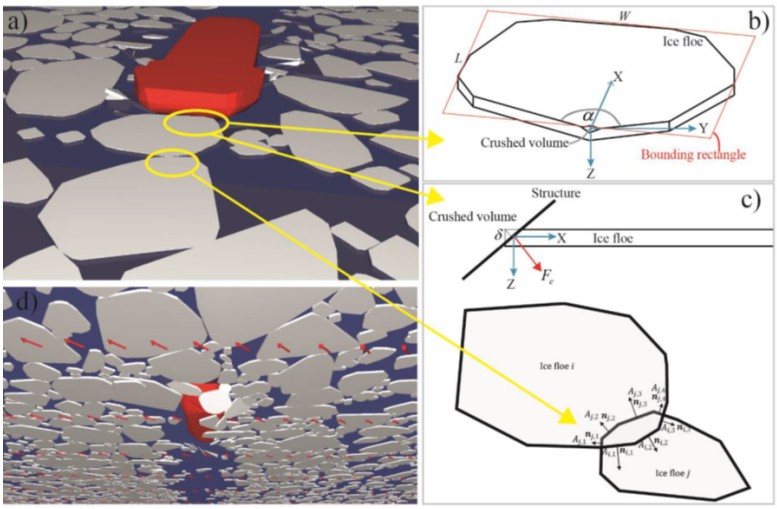

Figure 4.1: a) Simulation environment; b) Fracture model; c) NDEM or multi-body dynamic module; d) Fluid domain showing flow (Lubbad, Løset, et al., 2018a).

In Lambregts, 2024 a more basic (demo) version of the software has been used. In this version, it was not possible to analyse the forces on multiple structures. For his report a more advanced version is used, giving the opportunity to analyse the loads on each turbine. Furthermore, one can more accurately control how the simulation is performed using a main configuration file. This file can be used to prescribe a certain velocity, trajectory, or other variables to the simulated structure.

4.2. Offshore Wind Farm Layout

Within this research, a single OWF layout is used to investigate the ice action on each OWT monopile support structure. This limits the number of simulations that must be performed.

In general, the individual distance between the OWTs is approximately 5 times the diameter of the rotor (Yong & Shengli, 2016). This distance is used to ensure safe operations and to minimise wake and energy losses. One will use a DTU 10 MW turbine, all details regarding this turbine are publicly available. With a rotor diameter of 178 m (Bak et al., 2013), this results in an individual spacing of 890 m from the centre of each pile. However, a more general value of 1000 m is used, reducing energy losses even further.

The maximum diameter of the tower is 8.5 m at the bottom of the turbine (Bak et al., 2013). A monopile driven into the seabed forms the foundations for this OWT. The ice interacts with this support structure, and therefore the diameter of the monopile foundations is most relevant to determine the ice loads. Based on a previous study (Velarde, 2016) and considering both the water depth and the added horizontal load of the ice, the diameter of the monopile is assumed to be 10 m. This monopile (cylinder) is modelled using the Blender software so that it satisfies the object requirements of SAMS.

For this simulation, the OWF layout is chosen as a grid-like layout. This layout is convenient when analysing different wind directions. Furthermore, it performs well on power production when the wind direction varies. Which is studied in Zhang and Qian, 2016 and referred to as the ”WindMax layout” representing a grid OWF.

The size of the OWF is an important factor to take into account considering the computational times of SAMS. A larger OWF requires a larger ice field with a larger number of ice floes. This significantly increases the computational time for every simulation. In this case, a 5x5 layout will be used to simulate ice actions in an OWF. The layout is visualised in Figure 4.2. Creating a clear inner and outer region in the wind farm which could lead to clear blockage effects.

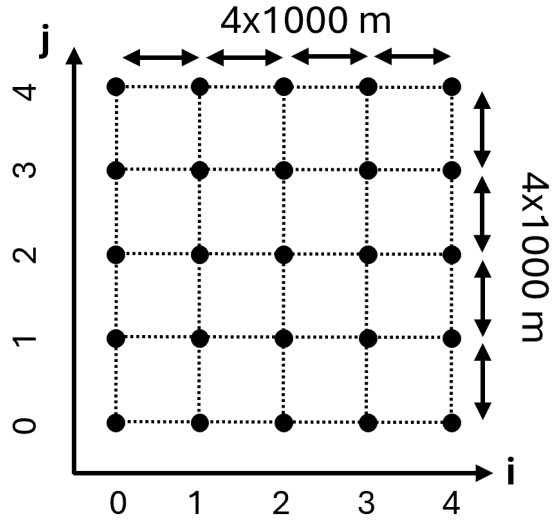

Figure 4.2: Schematic overview of the 5x5 grid layout with individual spacing of 1000 m.

The axes are labelled using i, j so that the turbines can be referred to as OWT_{ij}. Inflow of the ice will occur in the positive j direction. For different wind directions the wind farm will be rotated in clockwise direction. Given that the layout is symmetric, a rotation range of 0-45 $^\circ$ covers all possible inflow angles.

4.3. Environmental Conditions

The main environmental conditions of interest for this study are the direction and speed of the wind in the northern Baltic. Combining this with the current, the drift velocity of the ice is determined. This is of importance for the ice-OWF interaction.

4.3.1. Wind

The wind conditions of interest are the wind speed and direction at a height of $z = 10$ m. This value is used to determine the shear drag on the ice floes as given in Equation (2.2). Wind speed data in the northern Baltic can be found using the Global Wind Atlas (Davis et al., 2023). Data at $z = 10$ m is of interest for drift velocity, the data at $z = 100$ m is of interest for the power production. Both are shown in Figure 4.3.

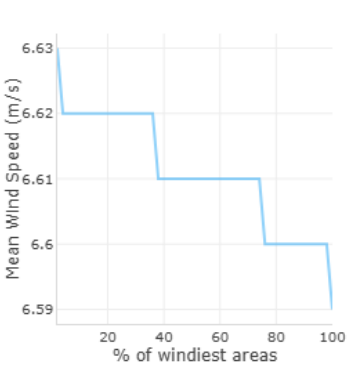

(a) Mean wind speed at $z = 10$ m.

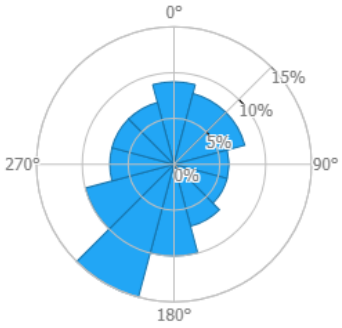

(b) Wind directions and occurrence at $z = 10$ m.

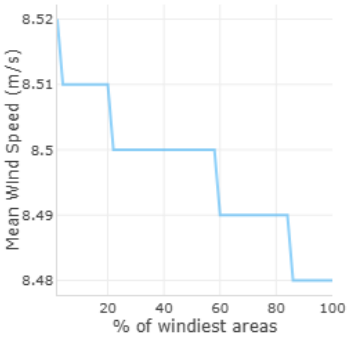

(c) Mean wind speed at $z = 100$ m.

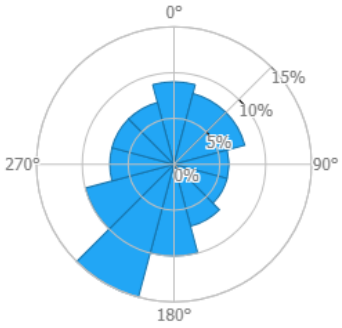

(d) Wind directions and occurrence at $z = 100$ m.

Figure 4.3: Mean wind speed and directions for $z = 10$ m and $z = 100$ m (Davis et al., 2023).

From these figures, one can clearly conclude that the wind directions are varying. Therefore, this area is interesting for investigating ice loads on a wind farm using different wind directions. The mean wind speed at $z = 10$ m is approximately $\overline{u_{10}} = 6.6$ m/s. At the hub height of the turbine, approximately $z = 100$ m, the mean wind speed is sufficient to generate energy. This ensures that the area of interest could be a potential OWF location.

4.3.2. Current

The main current of interest for ice drift is the near-surface current. Based on Equation (2.3), the drag force on the ice can be determined. To determine the force, the velocity one metre below the surface is used. The Baltic Sea experiences variable near-surface currents primarily driven by wind, air pressure differences, and density variations between water masses. Unlike the oceans, the Baltic Sea lacks permanent currents; instead, its currents vary with changing weather conditions. Typically, surface flow velocities range from 5 to 10 cm/s, but during severe storms, they can reach 50 cm/s. In

narrow straits between basins, currents can exceed 1 m/s. In general, southwestern winds are most common in the Baltic; this was also previously found in Figure 4.3. Due to the rotation of the Earth and this direction of the wind, the current generally has a circular pattern in the counter-clockwise direction (Finnish Meteorological Institute, 2025).

4.4. Generated Ice Field

The ice field present in the Baltic Sea must be accurately modelled within the simulation. Previously, the FSD has been determined using satellite images in Section 3.4. Furthermore, all relevant ice properties are discussed in Section 3.5. In this section, the method for generating an ice field in SAMS is covered. Furthermore, the size of the field and the usage of confinement are discussed.

4.4.1. Ice Floe Shapes

The shape of the ice floes has a significant impact on the mean ice loads. This effect is reported to be higher for circular structures than for rectangular structures. Therefore, the shape of the floes is of great relevance when modelling loads on monopiles. In general, predicting ice loads using square floes results in overly conservative forces. However, the use of circular floes might lead to a low prediction of ice loads (van den Berg et al., 2019).

The shapes of the floes that are used need to vary sufficiently such that it represents a real floe shape. Using a Matlab code one can control the floe shape based on two parameters. First, one can adjust the degree of polygon for the floe field. This is done using a minimum and maximum value; this value adjusts the number of vertices for each ice floe. Furthermore, one can adjust the aspect ratio of the floes. This gives the ratio between the length and the width of an ice floe, values in the range of 1.6-1.9 are given based on Toyota et al., 2011. In this study, the average of these values, 1.75 will be used to represent the floe aspect ratio.

To ensure sufficiently varying shapes, it is found that the maximal amount of vertices should be kept relatively low. Increasing this number results in a floe field dominated by circular shapes. Furthermore, to prevent floes from being to rectangular, the minimum degree of the polygon is found to be at least six.

4.4.2. Creating Ice Fields

The ice field is generated using Matlab and IceMaker, which is part of the SAMS software. Ice floes are created and placed using a Matlab code. The input for this code is given in Table 4.1.

Table 4.1: Ice Field Generator Matlab Input.

Parameter	Variable	Value	Unit
Domain length in x-direction	L_x	15000	m
Domain length in y-direction	L_y	15000	m
Minimal number of vertices	$V_{N,min}$	6	-
Maximal number of vertices	$V_{N,max}$	14	-
Aspect Ratio		1.75	-
Minimal MCD	MCD_{min}	85	m
Maximal MCD	MCD_{max}	20000	m
Power law coefficient	α	1.495	-
Ice Thickness	$\mathrm{h_i}$	0.86	m

The generated floe field should follow the FSD obtained before. To establish this, one uses the inverse transform sampling, also known as inverse transform algorithm (Ross, 2022). Applying this method on the previous defined power law, the floe MCDs are generated preserving the power law distribution. Given $p(x)$ this yields Equation (4.1), the full derivation is given in Appendix B.

$$MCD = \left(u\left(MCD_{\mathrm{max}}^{(1-\alpha)} - MCD_{\mathrm{min}}^{(1-\alpha)}\right) + MCD_{\mathrm{min}}^{(1-\alpha)}\right)^{\frac{1}{1-\alpha}} \tag{4.1}$$

In this equation u represents a uniform distribution and gives a value ranging from 0 to 1.

Furthermore, the previously discussed parameters for the floe shape are invoked as input parameters. For the FSD, the minimum MCD of the 1500 km^2 study area from image processing is used. The maximum value is based on an iterative process finding which values lead to realistic ice fields. Using a smaller maximum MCD generally leads to very little small floes caused by the inverse transform sampling used. Increasing the maximum limit gives a more realistic ice field given the used ice field generator algorithm. However, the maximal MCD exceeds the simulated ice field domain. This makes that floes from this size will not be placed in the simulated domain.

The main steps of the Matlab code are as follows:

1. **Domain and Ice Field Parameters:** A square domain of size $L_x \times L_y$ is defined, which results in a total area. The target ice concentration is also set, which results in the total ice area that needs to be generated.
2. **Floe Size Distribution:** Floe sizes follow a power-law distribution. The MCD is randomly sampled between 85 m and 20000 m using inverse transform sampling.
3. **Floe Placement Algorithm:**
   - Generate a polygonal floe with a random number of vertices.
   - Scale it to match the sampled MCD.
   - Attempts to place it randomly within the domain.
   - Ensures that it does not overlap with existing floes.

   If placement fails after a maximum number of attempts (1000), the floe is discarded.
4. **Output Files:** The script produces a configuration file (`.ini`) storing floe properties. This file is used in the IceMaker application to finalise the creation of the ice field.

It is important to note that the FSD is not completely satisfied. This is mainly dependent on the possibilities to place a floe of a certain size. If a generated floe of a specific size does not fit in the domain, it will be discarded. Therefore, larger floes are undersampled compared to the given power-law coefficient. For higher IC, it is more difficult to place the floes. Therefore, larger differences in the power law factor are expected for higher ice concentrations. The ice field domain has been selected such that larger floes can still be present. However, it is important to limit computational times, which is partially dependent on the number of floes. Considering these factors an ice field of 15x15 km has been used.

The `.ini` file created by the Matlab code is imported in the SAMS `IceMaker.exe`. Using this application, the remaining overlaps in the floe field are resolved and the ice field is exported for a given ice thickness. This results in a `.ice` file that is used to run the simulations.

In total, four ice fields are created using IC = 50%, 60%, 70%, 80%. These ice fields (`.ice`) are shown in Figure 4.4

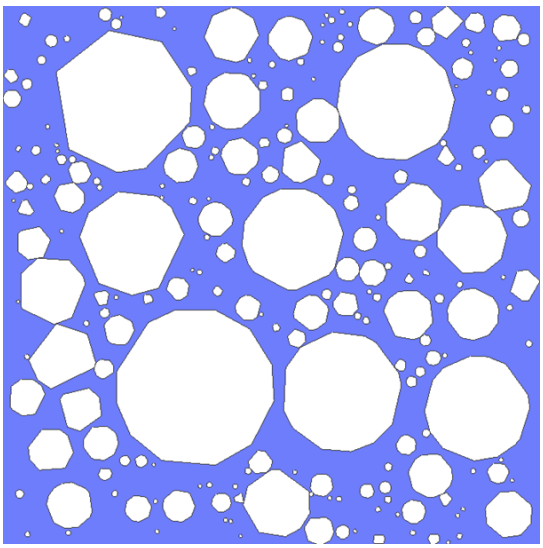

(a) SAMS Ice Field IC = 50%.

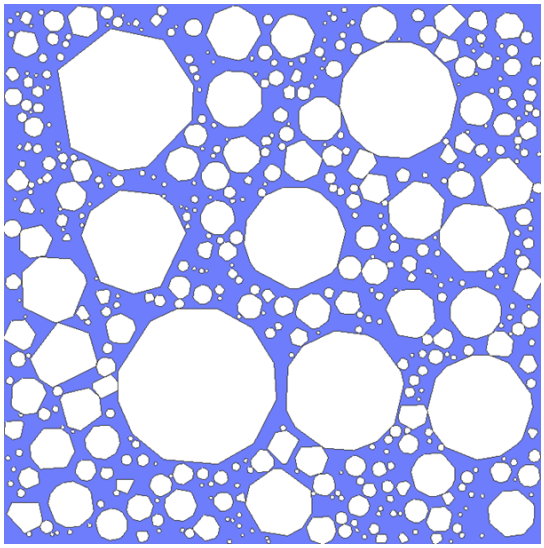

(b) SAMS Ice Field IC = 60%.

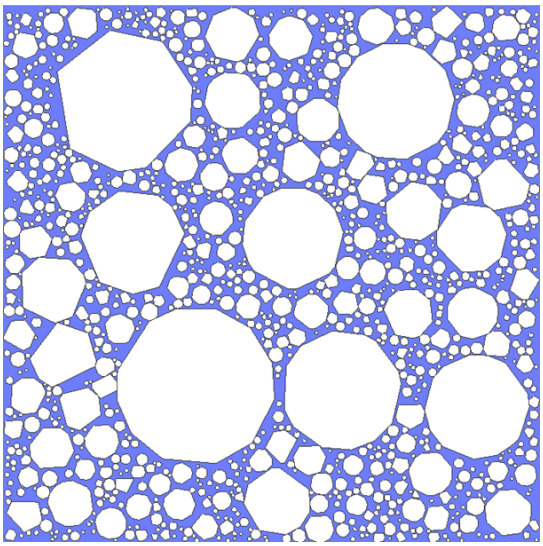

(c) SAMS Ice Field IC = 70%.

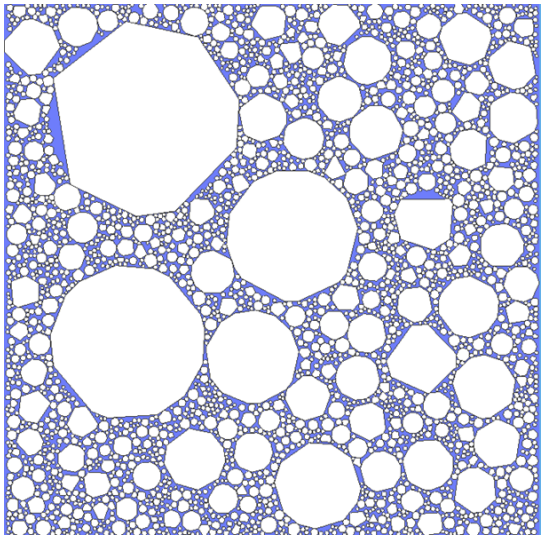

(d) SAMS Ice Field IC = 80%.

Figure 4.4: SAMS generated ice fields.

From these ice fields one can see that both circular and more rectangular shaped floes are present. This is importance for accurate results of the ice forces as previously mentioned in Section 4.4.1. Furthermore, the larger floes for IC 50%, 60% and 70% are placed similar, while for IC = 80% some more clear differences in the ice field are observed. This is mainly due to the randomness in the size and positioning method that is used.

4.4.3. Confinement

To simulate a more realistic environment while minimising the amount of floes, confinement is used. The generated ice field only takes into account the ice present in and around the windfarm. However, in a real-life scenario, the ice field is not limited to this size. Adding confinement walls to the simulation ensures that the effect of surrounding ice is taken into account so that the floes cannot freely drift out of the domain.

Multiple test simulations are performed to analyse the effect of this confinement. Without confinement, it is clearly visible that many floes move out of the ice field after interacting with the first structures. However, placing the confinement close to the OWF edges makes the ice very restricted to move, especially

for higher ice concentrations. Therefore, the ice field has been extended to 5 km on both sides of the wind farm. These walls are rigid and, therefore, can still obstruct the ice movement. In reality, larger floes would be able to push the ice on the boundaries away. This is not the case with confinement since it is modelled using rigid walls. For a more accurate representation either the confinement should be non-rigid or a larger ice domain should be used. The first option is not yet possible in SAMS, secondly, a larger ice field gives longer computational times and is therefore not feasible within this thesis.

4.5. Simulation Scenarios

To analyse the effect of the wind direction on the loads, four different wind directions are used. The OWF is rotated around the centre turbine to simulate different wind directions. Furthermore, different ice concentrations are investigated to determine whether the effect of the wind direction also depends on the ice concentration present. In total, there will be 16 simulated scenarios, the simulated angles are 0, 15, 30, 45 degrees. These are referred to as scenario x.1, x.2, x.3, x.4, respectively. The ice concentrations used are 50%, 60%, 70%, 80% and are referred to as 1.x, 2.x, 3.x, 4.x. The ice field will drift into the offshore wind farm, no initial ice is present.

The movement of the ice is governed by wind and current velocity. From Section 4.3.2, it is found that the current velocity is commonly around 5-10 cm/s. For these simulations, 5 cm/s will be used. The circular pattern of the current cannot be invoked in the software. To take this into account, the lowest current velocity has been selected to minimise the influence of this modelling simplification.

Furthermore, the wind speed at a height of 10 m is of interest. Section 4.3.1 shows that the mean wind velocity is around 6.6 m/s. However, from a design perspective, different wind speeds could be of interest according to Figure 2.5 the rated wind speed is of main interest Figure 2.5. The rated wind speed of the DTU 10MW turbine is 11.4 m/s at hub height (Bak et al., 2013). Given that the wind speed reduces over height, a wind speed of 10 m/s will be used in the simulations. This is based on assuming a decrease in wind speed over the height, no exact wind profile is used. Mainly because fluctuations over time will occur which are not taken into account. Therefore, an arbitrary value is used based on the rated wind speed of the turbine.

The simulations will be performed with a frequency of 10 Hz. Furthermore, to limit computational times, only 45.000 seconds are simulated. During the simulations, it was found that running a simulation can take a significant amount of time. Since SAMS is not optimised for GPU usage, running it on a supercomputer was not beneficial. For some parts of the simulations, computing 0.1 s takes 5-10 seconds or longer. To complete the used dataset, a total of 2 weeks of simulations have been performed. Due to limited time within this project the simulations are therefore limited to 45.000 seconds, while the initial idea was to run the simulations until the entire ice field had moved passed the OWF. However, there were no options to speed up the simulation process, which made it impossible to do so.

5

Simulation Results

In this section the results are discussed, first the ice load data is discussed, and a new analysis method is introduced. Moreover, the ice loads for each wind direction and ice concentration are discussed and compared.

5.1. Ice Load Analysis

An introduction will be given on how to interpret the ice loads in SAMS. A filtering technique will be applied to give realistic force values. Furthermore, a new load parameter is introduced, which makes it possible to compare the ice forces over time based on a single value.

5.1.1. Ice Loads in SAMS

In SAMS, different load components are determined and stored. For each structure (turbine), the following force components are given in the x, y and z directions:

- Ice breaking force [N]
- Ice rubble force [N]
- Ice torque [Nm]

The main parameter of interest for the general ice load analysis is the ice breaking force. An upper limit for this force is determined using the global pressure formula from ISO19906. Theoretically, ice crushing gives the highest possible force. Therefore, every force that exceeds this limit could possibly be a numerical instead of a physical result. It is important to note that within SAMS a different method is used to calculate the loads. However, since the highest force for design is determined using the ISO19906 formula, this will also be used as the upper limit. Using an ice thickness of 86 cm, a structure width of 10 m and using $C_R = 1.8$ [MPa] (Baltic Sea), first f_{AR} is calculated using Equation (5.1);

$$f_{AR} = e^{-\frac{w}{3h_i}}\sqrt{1+5\frac{h_i}{w}} = e^{-\frac{10}{3\cdot 0.86}}\sqrt{1+5\cdot\frac{0.86}{10}} \approx 0.024 \text{ [-]} \tag{5.1}$$

Invoking this into Equation (5.2), results in the global pressure:

$$\begin{aligned} p_G &= C_R\left[\left(\frac{h_i}{h_1}\right)^n\left(\frac{w}{h_i}\right)^m + f_{AR}\right] \\ &= 1.8\times 10^6\left[\left(\frac{0.86}{1}\right)^{-0.33}\left(\frac{10}{0.86}\right)^{-0.16} + 0.024\right] \\ &\approx 1.26\times 10^6 \text{ Pa} \end{aligned} \tag{5.2}$$

Multiplying p_G by the nominal area, Equation (5.3), results in the crushing force:

$$F_G = p_G \cdot h_i \cdot w = 1.26 \times 10^6 \cdot 0.86 \cdot 10 = 1.08 \times 10^7 \text{ N} \tag{5.3}$$

From this calculation, it can be concluded that peaks that are significantly larger than 10.8 MN are numerical peaks and should therefore be discarded in the force analysis.

The forces in SAMS are given in the x, y, and z directions. Therefore, the total force is computed to compute the total horizontal force acting on the structure. This is done using Equation (5.4), the force component in z direction is not of interest for this analysis. Generally, these forces are also less relevant for vertical structures and mainly are of significance for sloping structures.

$$F_H = \sqrt{F_x^2 + F_y^2} \tag{5.4}$$

5.1.2. Ice Load Comparison Method

One of the main challenges is to compare different ice load time series with another. From the literature, the methods of Rayleigh Separation, Power Spectral Density, and Rainflow Counting are found to be of possible use.

The Rayleigh-separated values generally fit a Weibull curve best, resulting in a shape and scale parameter. This curve gives little insight in the actual loads but mostly about the PDF based on a certain time period. Furthermore, it gives two parameters and a general error in the fit, which makes it complicated to compare all curves with another. Using another type of distribution, for example an exponential distribution, to fit the peaks could resolve this issue partially. However, inaccuracies in this fit might lead to misinterpreting the data since generally the error of the fit will not be considered or corrected for when comparing. Therefore, this method will not be used for this purpose.

The use of spectral density analysis for ice loads is found to have potential based on previous literature. Neumann's method gives a clear PSD function over the load frequency range. However, this method can be difficult to compare with different turbines, since it requires comparing multiple curves to another. Furthermore, it gives little insight in the magnitude of the forces that are present. These magnitudes are the main interest of the analysis. Therefore, this method can be used to gain more information about the force data but is not useful to analyse the magnitudes of the forces that occur.

Finally, the rainflow method could be used to interpret and compare the time series. The main goal is to express how many ice interactions have occurred and with what magnitude. Therefore, rainflow counting is the perfect method to use.

This method uses rainflow counting to count the number of force cycles in a time series. A lower limit (100 kN) is used to filter out all small values. The use of this threshold is inspired on the Rayleigh method; in this method, however, no separator value is used. In this way, all higher loads are selected instead of only load peaks. The rainflow algorithm will count the amount of load cycles present and determine the corresponding amplitude, after this the lower and upper thresholds are applied to the obtained data. All data is assigned to load bins with a size of 0.5 MN and a corresponding count for each bin is obtained. These will be assigned using an i amount of load bins. Which results in a histogram as shown in Figure 5.1.

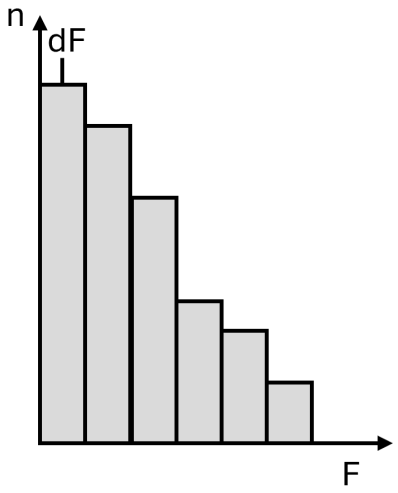

Figure 5.1: Force cycles obtained from rainflow counting.

From the data, it is imported to note that not all turbines are exposed to sea-ice for the same amount of time. Since the sea-ice drifts into the wind farm, certain turbines are exposed to the ice for a shorter time period compared to the ones further upstream. Therefore, t_{exp} is defined referring to the total time that a turbine can be exposed to ice. The time is calculated based of the location of the turbine and the free drift velocity of the ice. This velocity is determined using Equation (5.5).

$$v_i = \sqrt{\frac{\rho_a C_a}{\rho_c C_c}} v_a + v_c \tag{5.5}$$

This formula assumes no ice deformation, neglects sea surface tilt and air pressure gradients. It can generally be used when the ice concentrations are below 80% (Høyland, 2024). Using the previously defined parameters an ice drift of $v_i = 0.2$ m/s is found. It does not take into account the fact that the free-drift speed inside the wind farm will be different because of a blockage effect of the turbines.

This variable only takes into account the time frame in which a potential interaction could occur based on the drift speed. It does not take into account any blockage effects in the OWF or the duration of the load. Therefore, it is mainly useful if one wants to obtain an estimate of how the ice loading for a longer period of time would be like.

From the rainflow count, each bin n_i is multiplied by the average load from the corresponding bin dF_i [N]. A sum is taken over all bins to combine all the loads and counts, it is divided by the total exposed time and multiplied by the simulated time (=45000 s). This leads to a variable, referred to as the Ice Load Factor (ILF, Equation (5.6)), which is used to compare the loads for each turbine and wind farm.

$$\text{ILF} = \frac{\sum_i n_i \cdot dF_i}{t_{exp}} \cdot t_{sim} \tag{5.6}$$

The ILF takes into account the sum of the rainflow cycle count multiplied by the force and corrects for the exposed time to the ice for each turbine. The unit is in Newton's giving an insight into the forces that can be expected within the time interval.

5.2. Prediction of Ice-OWF Interaction Scenarios

In Section 2.2 the basic ice-structure interactions are explained theoretically. Before looking into the simulation results, one can assess possible outcomes of the interaction scenarios based on this theory. Doing so can help to understand what kind of interaction or limiting mechanism might occur.

5.2.1. Limiting Mechanisms

The three load-limiting mechanisms are introduced in Section 2.2.3. Limit stress yields the highest ice force, as the ice crushes against the structure. It occurs when the driving forces are larger than the global force, also called the crushing force. The driving force based only on wind and current is calculated using Equation (5.7)

$$F_d = F_a + F_c = \tau_a A_i + \tau_c A_i = \left(\rho_{air} \cdot C_a \cdot u_{10}^2 + \rho_{water} \cdot C_c \cdot u_1^2\right) A_i \tag{5.7}$$

The limit stress condition is given by $F_d > F_G$, which results in Equation (5.8).

$$\left(\rho_{air} C_a u_{10}^2 + \rho_{water} C_c u_1^2\right) A_i > C_R \left[\left(\frac{h_i}{h_1}\right)^n \left(\frac{w}{h_i}\right)^m + f_{AR}\right] \cdot h_i \cdot w \tag{5.8}$$

The right-hand side has previously been obtained from Equation (5.3). Using the other simulation parameters, one finds Equation (5.9)

$$\begin{aligned} \left(\rho_{\text{air}} C_a u_{10}^2 + \rho_{\text{water}} C_c u_1^2\right) A_i &> 1.08 \times 10^7 \\ \left(1.04 \cdot 0.6 \times 10^{-3} \cdot 10^2 + 1005 \cdot 3 \times 10^{-3} \cdot 0.05^2\right) A_i &> 1.08 \times 10^7 \\ 0.06994\, A_i &> 1.08 \times 10^7 \\ A_i &> \frac{1.08 \times 10^7}{0.06994} \approx 154.35\,\text{km}^2 \end{aligned} \tag{5.9}$$

Assuming a circular floe, this would result in an MCD of approximately 7 km. Considering the size of the simulated ice field, individual floes of this size will not be present. However, when floes accumulate this amount of ice area can be reached, which results in sufficient driving forces to crush the ice. Therefore, limit stress can occur, most likely for higher ice concentrations, so sufficient ice can accumulate.

Limit force occurs when the driving forces are not sufficient to fail the ice. Failing ice can consist of multiple mechanisms and is not limited to ice crushing. Therefore, it is more complex to analyse analytically in which cases this will occur. The same holds for the limit energy scenario. However, one could predict that for very large floes, they would interact with multiple turbines at once. The resistance of these turbines is likely to be causing one of these two mechanisms to occur.

5.2.2. OWF Resistance

The turbines in the wind farm contribute to giving a certain resistance to the movement of sea-ice. This resistance can be expressed in different ways, such as how it slows down the ice field or what kind of forces are needed to get passed the structures.

The first line of turbines the ice field encounters could be seen as the main resistance. These structures will always interact with floes larger than the turbine spacing. This will mainly impact and reduce the floe sizes further downstream the OWF. Therefore, the first line of turbines can be seen as the first and main resistance to the ice field. Consequently, it is also expected that these turbines will experience the highest forces and the most number of interactions.

When not including failure through fracture, one can determine the resistance of the turbine using the crushing specific energy. Using the nominal area, one finds that approximately 10.8 MN is needed to fail the ice in crushing against the structure. So, this is the resistance each turbine offers when a floe is driven into it by the driving forces. Only if these forces exceed the resistance, the ice will fail and move passed the turbine. For larger floes, interaction with multiple turbines is possible, increasing this limit even further.

5.3. Wind Direction Effect

In this section the effect of wind direction is analysed for different ice concentrations. For each turbine, the ILF parameter is determined, giving insight into the experienced loads. The effect of wind direction is first analysed for each ice concentration.

Note that there will be referred to as the first, second, etc. Line of turbines from this part onwards. This should be seen as the first line of turbines that the ice encounters. For a zero-degree wind direction this is equal to the row at x = 0. However, for other angles, it consists of the 9 turbines on the outer 'layer' of the OWF. This is visualised in Figure 5.6.

5.3.1. IC = 50%

The ILF is determined for each wind direction given an ice concentration of 50%, the results are shown in Figure 5.2.

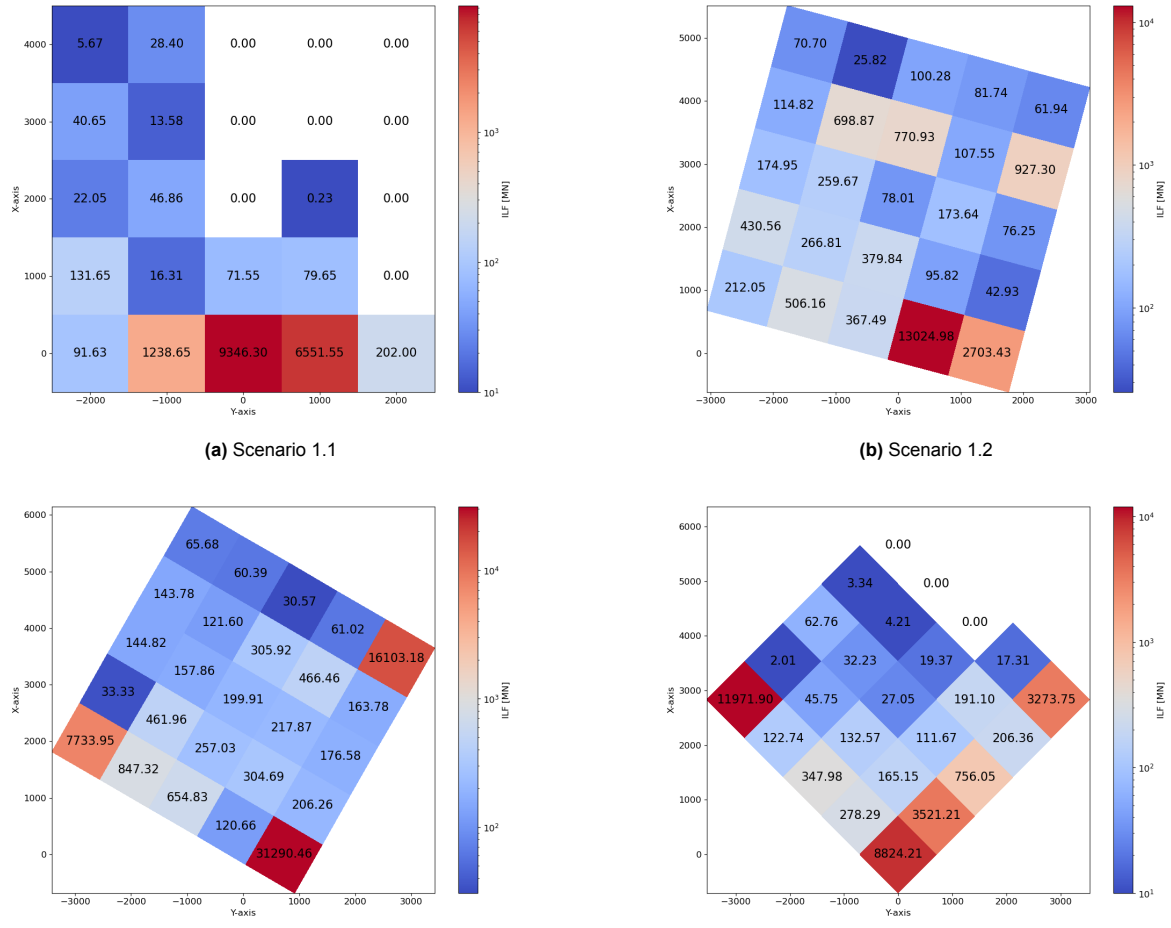

(a) Scenario 1.1

(b) Scenario 1.2

(c) Scenario 1.3

(d) Scenario 1.4

Figure 5.2: Heatmap of ILF [MN] over the OWF with changing wind directions for IC = 50%.

From these figures, it can generally be concluded that the highest ILF factor is always present at the first line of turbines. This was previously predicted in Section 5.2.2, considering that these turbines are the first resistance encountered by the ice field. In both Figure 5.2a and Figure 5.2d turbines are present that do not have ice forces higher than the threshold. This is mainly due to the low ice concentration resulting in little or none ice-structure interaction. Once the ice is split by previous turbines, it moves further downstream without moving in the y direction, resulting in fewer interactions with the ice.

A statistical summary of ILF is given in Table 5.1. For this ice concentration, a wind angle of zero results in the lowest sum and mean ILF value. Scenario 1.3 has the highest sum over the wind farm and also the highest peak for a single turbine. The peak is significantly larger compared to the other wind directions. The main cause of this is that limit force occurs when a large floe interacts with the turbine. After some time, radial and circumferential cracking starts to occur. This leads to many load cycles and therefore to a high ILF.

Table 5.1: Statistical analysis of ILF [MN] values for IC = 50%.

Dataset	Min	Max	Mean	Std Dev	Sum
Scenario 1.1	0	9.35×10^3	715.47	2.18×10^3	1.79×10^4
Scenario 1.2	25.82	1.30×10^4	870.10	2.54×10^3	2.18×10^4
Scenario 1.3	30.57	3.13×10^4	2.41×10^3	6.80×10^3	6.03×10^4
Scenario 1.4	0	1.20×10^4	1.20×10^3	2.89×10^3	3.01×10^4

5.3.2. IC = 60%

The ILF for different wind directions given that IC = 60% are shown in Figure 5.3.

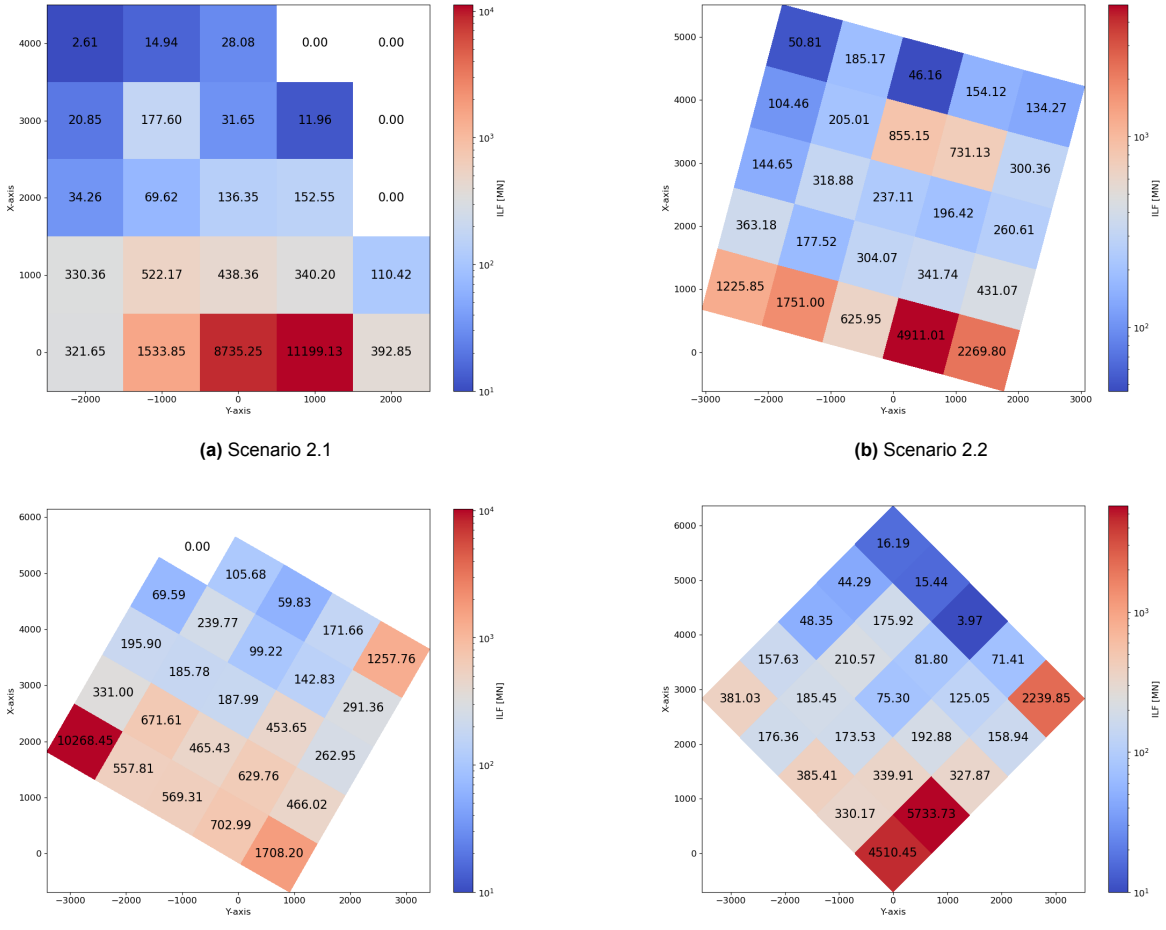

(a) Scenario 2.1

(b) Scenario 2.2

(c) Scenario 2.3

(d) Scenario 2.4

Figure 5.3: Heatmap of ILF [MN] over the OWF with changing wind directions for IC = 60%.

For this case, the previous conclusion, the first line of turbines has the highest ILF, still holds. In Figure 5.3a and Figure 5.3d one notices that there are fewer turbines with a zero ILF compared to scenario 1.1 and 1.4. Since more ice floes are present, the ice has more momentum in the y-direction, which causes the ice to drift sideward after interacting with the first line of turbines. Furthermore, in Figure 5.3c, a clear shift in the maximum ILF is observed to the left side of the OWF. From visual inspection it is clear that this is caused by the different ice fields. A large floe is present on the left-hand side of the ice field. Just like in the previous case this causes limit force to occur. This is followed by radial and circumferential cracks once other pieces of ice provide extra driving forces. The failure mechanism of radial and circumferential cracks gives a high amount of load peaks and therefore a high ILF.

From the statistical data given in Table 5.2, fundamental differences are observed compared to IC = 50%. The main difference is that in this case a wind angle of 45 degrees (Scenario 2.4) results in the lowest sum and mean of ILF. Furthermore, Scenario 2.1 has the highest number of interactions. These are mainly concentrated at the first two lines of turbines that the ice encounters. A significant decrease is observed further downstream.

Table 5.2: Statistical analysis of ILF [MN] values for IC = 60%.

Dataset	Min	Max	Mean	Std Dev	Sum
Scenario 2.1	0	1.12×10^4	984.19	2.69×10^3	2.46×10^4
Scenario 2.2	46.16	4.91×10^3	653.02	1.02×10^3	1.63×10^4
Scenario 2.3	0	1.03×10^4	803.78	1.97×10^3	2.01×10^4
Scenario 2.4	3.97	5.73×10^3	646.46	1.40×10^3	1.62×10^4

5.3.3. IC = 70%

The ILF for different wind directions given that IC = 70% are shown in Figure 5.4.

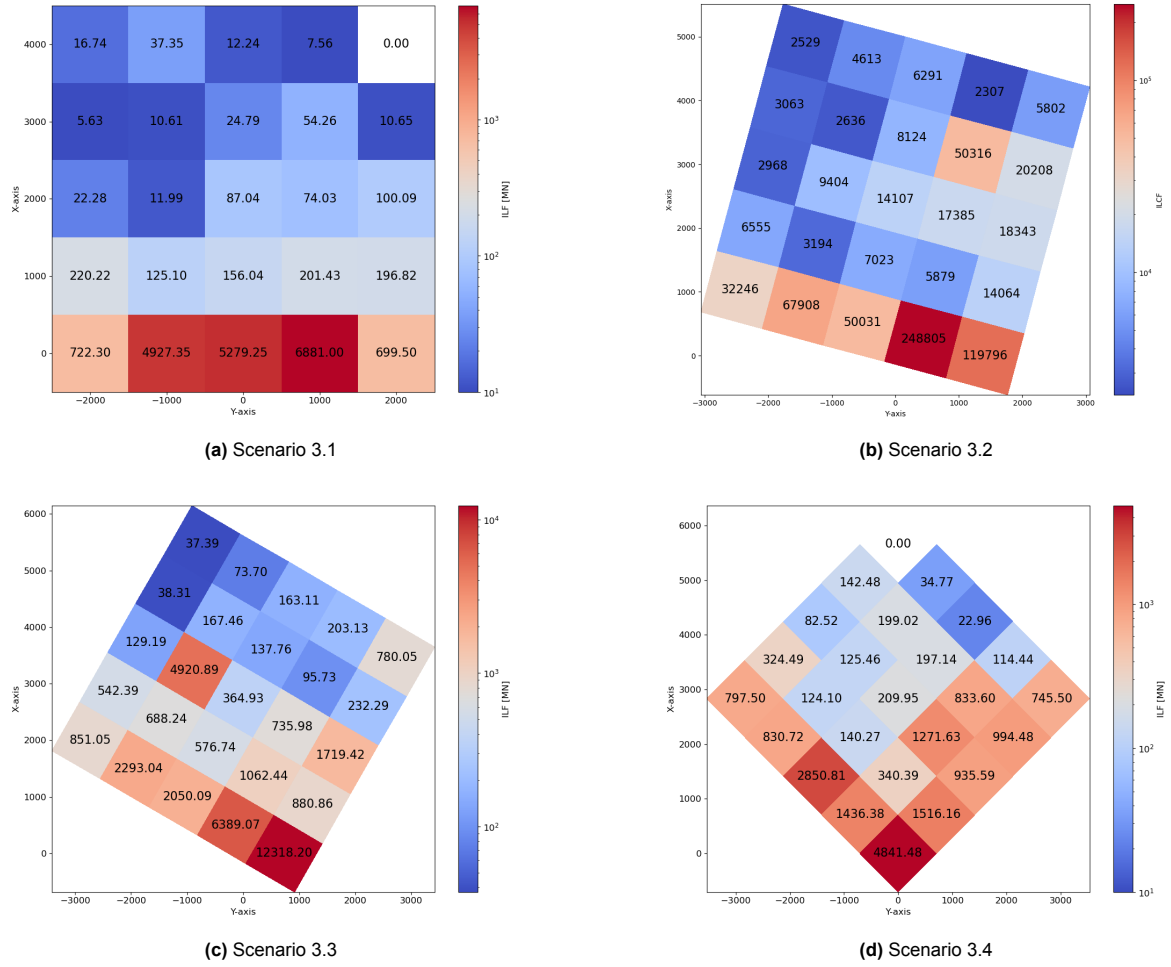

(a) Scenario 3.1 **(b)** Scenario 3.2

(c) Scenario 3.3 **(d)** Scenario 3.4

Figure 5.4: Heatmap of ILF [MN] over the OWF with changing wind directions for IC = 70%.

As noted previously, the number of turbines that experience ILF = 0 decreases as the concentration of ice increases. This statement is still valid considering the above results. Only in Figure 5.4a and Figure 5.4d is a turbine that does not interact with the ice. Most ice interactions are observed in the first line of turbines.

Furthermore, from Table 5.3 it is found that the scenario with a wind angle of 45 degrees has the lowest sum and mean ILF. This result is similar to that found for IC = 60%. However, for this ice concentration, a wind angle of 30 degrees (Scenario 3.3) results in the highest sum, unlike previously.

Table 5.3: Statistical analysis of ILF [MN] values for IC = 70%.

Dataset	Min	Max	Mean	Std Dev	Sum
Scenario 3.1	0	6.88×10^3	795.37	1.84×10^3	1.99×10^4
Scenario 3.2	103.81	1.12×10^4	1.30×10^3	2.34×10^3	3.26×10^4
Scenario 3.3	37.39	1.23×10^4	1.50×10^3	2.67×10^3	3.75×10^4
Scenario 3.4	0	4.84×10^3	764.47	1.05×10^3	1.91×10^4

5.3.4. IC = 80%

The ILF for different wind directions given that IC = 80% are shown in Figure 5.5.

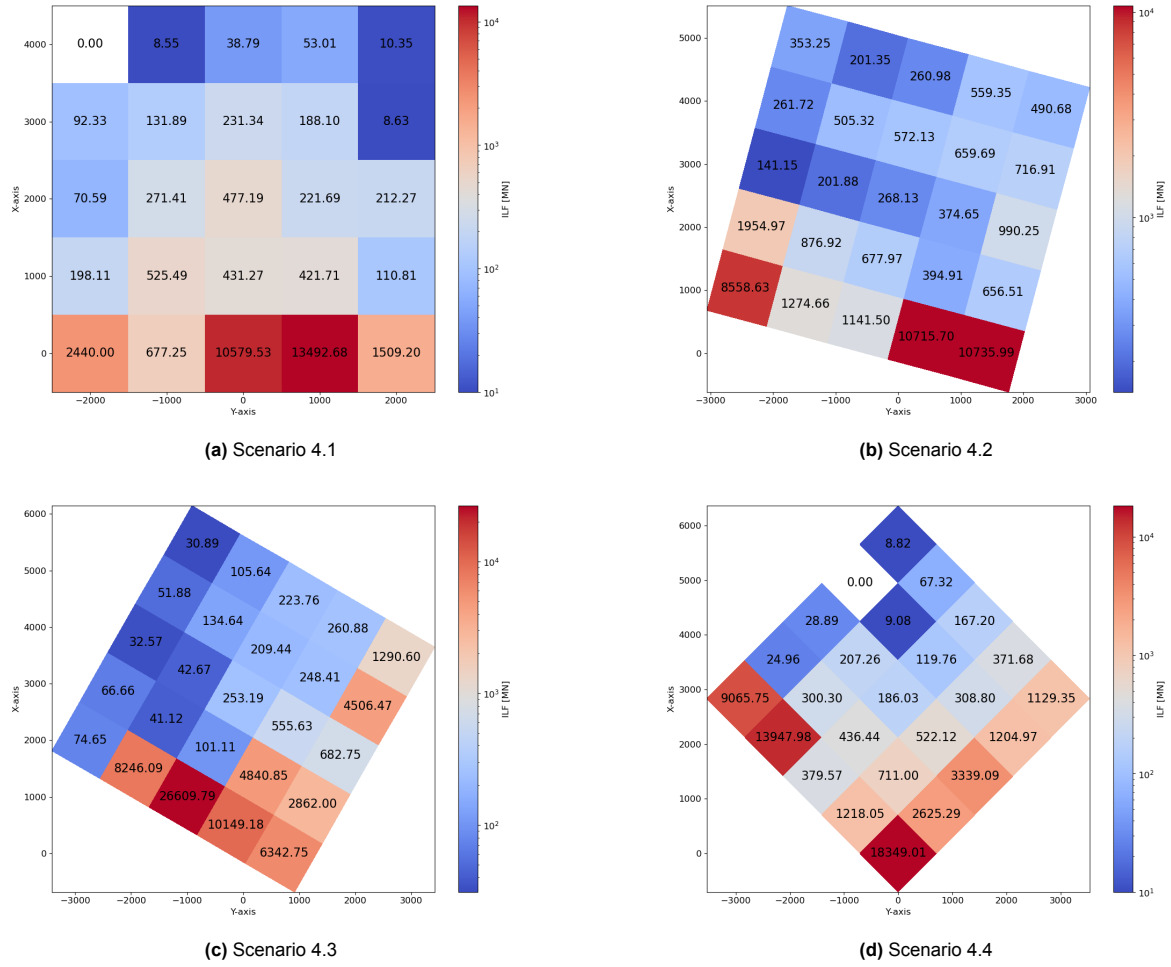

(a) Scenario 4.1

(b) Scenario 4.2

(c) Scenario 4.3

(d) Scenario 4.4

Figure 5.5: Heatmap of ILF [MN] over the OWF with changing wind directions for IC = 80%.

Similarly to IC = 70%, turbines with a zero ILF are present for a wind angle of 0 and 45 degrees. However, in this case the position of the turbines is different. Furthermore, maximal values are present at the outer line of the turbines as previously found for other ice concentrations.

Based on Table 5.4, one finds that a zero degree wind angle gives the lowest sum and mean ILF. Furthermore, it is found that the sum of scenario 4.3 and 4.4 are considerately higher than 4.1 and 4.2. This is governed by the significant higher peak value observed for these scenarios.

Table 5.4: Statistical analysis of ILF [MN] values for IC = 80%.

Dataset	Min	Max	Mean	Std Dev	Sum
Scenario 4.1	0	1.35×10^4	1.30×10^3	3.24×10^3	3.24×10^4
Scenario 4.2	141.15	1.07×10^4	1.74×10^3	3.10×10^3	4.35×10^4
Scenario 4.3	30.89	2.66×10^4	2.72×10^3	5.62×10^3	6.80×10^4
Scenario 4.4	0	1.83×10^4	2.19×10^3	4.55×10^3	5.47×10^4

5.4. Lines of Turbines Analysis

The ”Lines” of turbines have previously been defined. From the previous section, one can see that the ILF reduction over these lines can be significant. Therefore, this will be analysed in more detail. To clarify the definition of these lines, they are indicated for each wind direction in Figure 5.6.

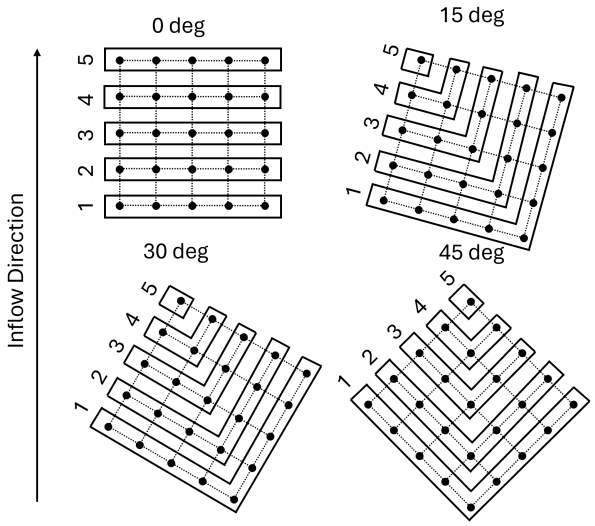

Figure 5.6: ”Lines” of turbines visualised for all four wind directions.

Analysis of these lines gives insight into how the ice action changes when the ice moves through the wind farm. A statistical analysis is performed for each simulation and is shown in Appendix C. The ILF over each line generally decreases as the ice moves further downstream of the OWF. The only exception to this is for Scenario 3.3, in this case the sum in line 3 is higher than in line 2. This is mainly because at OWT_{23} limit momentum occurs followed by radial and circumferential cracking. Which leads to an increase in the force cycles in this turbine, which also influences the sum in this line.

The percentage decrease of the sum over the turbine lines is shown in Table 5.5. Based on this, one can determine how the ice loads decrease while moving down the wind farm. The first line of turbines is used as reference to calculate the percentual decrease. From this one can clearly see that for a wind angle of zero degrees, the decrease in ice loads is generally established the fastest. Only for IC = 80% the 45 degree performs slightly better, this difference is however very small. Furthermore, a wind angle of 15° and 30° is found to be the least effective at reducing ILF for the second line of turbines.

Table 5.5: Percentual decrease compared to the ILF [MN] sum of the first line for each IC.

Line	IC = 50			
	0°	15°	30°	45°
Line 2	-98.28	-91.43	-96.85	-97.73
Line 3	-99.60	-92.28	-98.54	-99.52
Line 4	-99.69	-95.32	-99.43	-99.97
Line 5	-99.80	-99.61	-99.89	-100.00
Line	**IC = 60**			
	0°	15°	30°	45°
Line 2	-92.15	-80.96	-82.18	-91.25
Line 3	-98.23	-86.55	-95.47	-97.05
Line 4	-98.91	-95.85	-97.42	-98.35
Line 5	-99.79	-99.57	-100.00	-99.89
Line	**IC = 70**			
	0°	15°	30°	45°
Line 2	-95.14	-83.95	-85.81	-78.94
Line 3	-98.40	-92.92	-79.23	-95.73
Line 4	-99.43	-98.21	-98.98	-97.48
Line 5	-99.60	-99.56	-99.86	-100.00
Line	**IC = 80**			
	0°	15°	30°	45°
Line 2	-94.12	-84.42	-89.94	-94.78
Line 3	-95.63	-95.91	-98.75	-98.62
Line 4	-97.73	-97.26	-99.52	-99.85
Line 5	-99.61	-99.00	-99.95	-99.98

For the lowest ice concentration (IC = 50%) the decrease for all wind directions is approximately the same. Only when the ice concentration increases, a more clear difference is seen for changing wind directions. Since a higher IC results in more ice floes in the ice field. Therefore, it is more likely that a turbine interacts with an ice floe. This influences the drift in and around the wind farm. Generally, more sideward movement is caused by higher ice concentrations. This makes ice more likely to interact with turbines further downstream. For lower concentrations, the ice continues to move along the same streamline resulting in less ice-structure interactions.

To gain a better understanding, the mean of the ILF will also be considered. Since some lines contain fewer turbines, this might give a bias in the analysis. Therefore, the percentual decrease for the mean value is given in Table 5.6. This table confirms the previous finding, since the mean load also decreases the fastest for a zero-degree wind angle. Furthermore, it is found that the mean ILF is decreased by >70% and the sum by >75% after interacting with the first line of turbines in all scenarios. Hence, significant reduction over the wind farm is present.

Table 5.6: Percentual decrease compared to the ILF [MN] mean of the first line for each IC.

Line	IC = 50			
	0°	15°	30°	45°
Line 2	-98.28	-88.98	-95.96	-97.08
Line 3	-99.60	-86.10	-97.36	-99.13
Line 4	-99.69	-85.95	-98.29	-99.92
Line 5	-99.80	-96.45	-98.97	-100.00
Line	**IC = 60**			
	0°	15°	30°	45°
Line 2	-92.15	-75.51	-77.09	-88.75
Line 3	-98.23	-75.79	-91.85	-94.69
Line 4	-98.91	-87.54	-92.26	-95.04
Line 5	-99.79	-96.16	-100.00	-98.98
Line	**IC = 70**			
	0°	15°	30°	45°
Line 2	-95.14	-79.36	-81.75	-72.92
Line 3	-98.40	-87.25	-62.61	-92.32
Line 4	-99.43	-94.64	-96.95	-92.45
Line 5	-99.60	-96.06	-98.78	-100.00
Line	**IC = 80**			
	0°	15°	30°	45°
Line 2	-94.12	-79.96	-87.06	-93.29
Line 3	-95.63	-92.63	-97.74	-97.51
Line 4	-97.73	-91.77	-98.56	-99.55
Line 5	-99.61	-90.99	-99.54	-99.85

5.5. Ice Load Contact Factor (ILCF)

The previously defined ILF takes into account the total time that interactions could occur. However, it is not given that during this full time period ice interaction always occurs. Therefore, the contact factor of the ice load is introduced and defined. This factor is based on the same principles as the ILF and uses the same load threshold. The key difference is that only the number of seconds is used when the interaction occurs. Hence, $t_{contact}$ counts when the load is above 100 kN and sums up all these data points, giving it the number of seconds in which interactions have occurred. It is defined using Equation (5.10).

$$\text{ILCF} = \frac{\sum_i n_i \cdot dF_i}{t_{contact}} \cdot t_{sim} \tag{5.10}$$

In Appendix D both the ILCF and $t_{contact}$ are shown for each scenario. Furthermore, all statistical data is also provided for each scenario and line of turbines.

First, one analyses the new defined parameter $t_{contact}$. This parameter gives the total amount of time that the ice force is above the lower threshold (100 kN). The percentual change in interaction time is shown in Table 5.7 and Table 5.8. Generally, one can see a significant decrease in interaction time over the lines of turbines. This reduction in interaction was already identified using ILF and is confirmed by this observation. A decrease in interaction time yields an increase in ILCF if the ice loads would stay constant. Therefore, a decrease in ILCF generally shows lower ice loads and a lower occurrence.

Table 5.7: Percentual change compared to the $t_{contact}$ [s] sum of the first line for each IC.

Line	IC = 50			
	0°	15°	30°	45°
Line 2	-97.75	-86.99	-52.87	-58.58
Line 3	-99.41	-92.22	-74.87	-91.72
Line 4	-99.82	-94.19	-91.05	-99.97
Line 5	-99.89	-99.81	-97.67	-100.00
Line	**IC = 60**			
	0°	15°	30°	45°
Line 2	-88.24	-83.30	-9.71	-33.55
Line 3	-98.23	-90.23	-68.59	-82.88
Line 4	-99.18	-96.96	-81.32	-92.25
Line 5	-99.87	-99.87	-100.00	-99.97
Line	**IC = 70**			
	0°	15°	30°	45°
Line 2	-96.00	-81.64	-36.11	-55.49
Line 3	-98.92	-89.98	-54.97	-79.11
Line 4	-99.61	-97.29	-86.74	-93.51
Line 5	-99.76	-99.70	-97.96	-100.00
Line	**IC = 80**			
	0°	15°	30°	45°
Line 2	-92.97	-75.23	-43.51	-54.97
Line 3	-95.63	-95.99	-71.30	-87.36
Line 4	-98.09	-97.42	-85.03	-99.55
Line 5	-99.76	-99.35	-98.72	-99.98

Table 5.8: Percentual change compared to the $t_{contact}$ [s] mean of the first line for each IC.

Line	IC = 50			
	0°	15°	30°	45°
Line 2	-97.75	-83.27	-39.40	-46.75
Line 3	-99.41	-86.00	-54.77	-85.10
Line 4	-99.82	-82.58	-73.15	-99.92
Line 5	-99.89	-98.28	-79.01	-100.00
Line	**IC = 60**			
	0°	15°	30°	45°
Line 2	-88.24	-78.53	16.09	-14.56
Line 3	-98.23	-82.41	-43.46	-69.18
Line 4	-99.18	-90.89	-43.95	-76.76
Line 5	-99.87	-98.79	-100.00	-99.73
Line	**IC = 70**			
	0°	15°	30°	45°
Line 2	-96.00	-76.40	-17.86	-42.78
Line 3	-98.92	-81.96	-18.95	-62.39
Line 4	-99.61	-91.86	-60.22	-80.52
Line 5	-99.76	-97.29	-81.60	-100.00
Line	**IC = 80**			
	0°	15°	30°	45°
Line 2	-92.97	-68.16	-27.36	-42.10
Line 3	-95.63	-92.78	-48.34	-77.24
Line 4	-98.09	-92.25	-55.09	-98.65
Line 5	-99.76	-94.13	-88.44	-99.85

The interaction times for a 0 and 15 degree heading decrease significantly more. Furthermore, these wind angles result in the lowest ILCF sum and mean values for all ice concentrations. Therefore, based on the ILCF one can conclude that these two wind directions result in the best reduction of ice loads based on the total interaction time. Furthermore, one concludes that the 30 degree wind angle yields the lowest reduction and therefore has the lowest ice-structure interaction blockage effect. This could potentially be caused by the fact that this angle has the highest offset in the position of the turbine in y-direction. Therefore, turbines in previous lines do not prevent other turbines further downstream to interact with the ice field.

Furthermore, in Appendix D one can see that the mean and sum of ILCF is lowest for a zero-degree wind direction for lower ice concentrations (IC = 50% and IC = 60%). For higher ice concentrations (IC = 70% and IC = 80%), a 15 degree wind direction results in the lowest values. The highest value for ILCF is always obtained for a 30 degree wind direction. As previously found, this wind direction generally also shows the smallest percentual decrease in interaction time over the lines of turbines. Therefore, one can conclude that the turbines for this wind angle are generally the most exposed to ice loads and that the least blockage effects occur.

If the ILCF decreases over the lines of turbines this generally implies a lower ice loads and a lower occurrence. Considered that the interaction time in most cases decreases the same is needed for the product of the load bins and mean force in order for ILCF to decrease. However, from the obtained results no consistent ILCF decrease for a specific IC or wind direction is observed.

5.6. Ice Load Return Period

In the previous analysis performed, force and occurrence are combined as a factor. To gain a better understanding of the occurrence of each load, the return period can provide useful information on the ice loads at the wind farm. The return period is calculated using the previously defined t_{exp} in combination with the count n_i. This gives the return period of the load in the time that a potential ice-OWT could have occurred. The return period for each load bin is calculated using Equation (5.11). For every scenario, the results are shown in Appendix E. For design purposes, a return period is usually given so that a certain load can be expected once every x years. However, for these ice loads it is not possible to perform an analysis like this. This would also involve the probability of all environmental data, making it more complex. Therefore, this analysis focusses on the return period based on the simulations performed. Doing so gives the number of seconds that a certain load can be expected.

$$T_i = \frac{t_{exp}}{n_i} \tag{5.11}$$

From these figures, one can generally conclude that the return period for smaller forces decreases when the ice concentration increases. Given that more ice is present in these scenarios automatically yields a higher occurrence of ice-structure interaction. These figures show that this increase in occurrence is mainly for lower ice loads.

Generally, it can be observed that ice loads greater than 5-6 MN rarely occur. The exception is for turbines present in the first line of turbines that interact with the largest ice floes. Moving further downstream reduces the floe sizes and therefore also the ice loads that occur. The ice loads that occur with a high frequency for most turbines is generally limited to around 3.5 MN. From this return period analysis one can conclude that most ice forces occur most in the lower part of the defined force range. Force ranging above 6 MN is rare for most turbines, especially further down the wind farm.

6

Application of Machine Learning Regressors

The main purpose of this chapter is to explore the possibilities of using machine learning (ML) to predict ice loads in an OWF. Based on the obtained simulation data, different regression models will be trained and tested. The main objective is to see if a regressor can be used to give a prediction of the ILF value. If this is the case, it could be used for optimisation purposes as well.

6.1. Machine Learning Models

This study utilizes a variety of regression models from the `scikit-learn` Python library (Pedregosa et al., 2011). Each method offers a different approach to capturing relationships between the parameters (features) and the solution (target). The functionality and performance of each of these ML models will be tested based on the obtained data.

6.1.1. Linear Regression (LR)

Linear Regression is one of the most basic and widely used regression techniques. It assumes a linear relationship between the input variables (X) and the target (y). This model attempts to fit a hyperplane that minimizes the residual sum of squares between the observed and predicted values (Hastie et al., 2009). The regressor is described by Equation (6.1).

$$y = \beta_0 + \beta_1 x_1 + \beta_2 x_2 + \cdots + \beta_n x_n \tag{6.1}$$

6.1.2. Decision Tree Regression (DTR)

A Decision Tree Regressor models the data by learning simple decision rules inferred from the data features. Splits the data set into subsets based on characteristic values, ultimately forming a tree where each leaf represents a predicted value (Breiman et al., 1984).

6.1.3. Random Forest Regression (RFR)

Random Forest regression is introduced by Breiman, 2001. They consist of a collection of tree predictors with each tree depending on the values of an individually sampled vector. In general, this method is effective for a small amount of data while dealing with multiple variables (Grömping, 2009).

6.1.4. Support Vector Regression (SVR)

SVR is an extension of Support Vector Machines (SVM) for regression problems. It aims to fit the best line (or hyperplane in higher dimensions) within a threshold (ϵ) so that most of the data points fall within this margin (Drucker et al., 1997).

6.2. Dataset Creation and Model Evaluation

To evaluate and compare different regression models, a dataset is generated and analysed using Python. The process involved generating data, splitting it into training and test sets, training models, and evaluating them.

6.2.1. Data Set Preparation

The following parameters are selected for training the regression models:

- (x,y) for each turbine for every wind angle orientation.
- IC of the used ice field in percentage.
- Ice Load Factor for each turbine every scenario.

Combining these data gives a complete data set to test and train the regressors.

The feature matrix X contains the variables `x`, `y` and `IC` while the target y corresponds to the `ILF` values.

The data set is divided into training and testing sets using the `train_test_split` function from `sklearn.model_selection`, with 80% of the data used for training and 20% for testing. One uses a random state of 42 to ensure that for each method the same training and test data is selected. In Table 6.1 is shown how many data point are used for each ice concentration.

Table 6.1: IC Value Counts in Training and Testing Sets.

IC Value	Training Set Count	Testing Set Count
50	74	26
60	82	18
70	82	18
80	82	18

From this table one notices that not all ice concentrations occur the same amount of time in the training and test set. Since all data is gathered in one data base the total is equal to a 80/20 training test principle. In this case IC = 50% has a different training/test ratio, it is however unknown yet how and if this influences the regressors performance.

6.2.2. Comparison of Regressor Performance

The performance of each regressor is compared using the Mean Square Error (MSE). In total 80 data points are tested, given that the full database consist of 400 entries. The exact prediction for each regressor model and the absolute error is shown in Table F.1. Furthermore, the comparison for each model is given in Table 6.2. Based on the MSE the regressors are sorted, which results in the random forest regressor performing the best. Across other indicators, it also performs the best with the only exception being a slightly higher mean relative error.

In general, the fits are not that accurate, and the errors are significant. This is mainly due to large mismatches in the extreme ILF values. Such as zero values and very high peaks that are not approximated correct. To make a better performing regressor, more data is needed or more advanced machine learning methods. The SVR method is clearly not suitable for this kind of purpose, as it performs worse than using the mean value of all data, given that R^2 is negative.

Table 6.2: Error Overview Across Regression Models.

Model	MSE	RMSE	R^2	Total Abs Error	Mean Rel Error
Random Forest	1.17×10^7	3.42×10^3	0.0638	7.35×10^4	4.84×10^{10}
Decision Tree	1.19×10^7	3.44×10^3	0.0494	7.59×10^4	3.08×10^{10}
Linear Regression	1.19×10^7	3.45×10^3	0.0475	1.38×10^5	5.99×10^{11}
Support Vector Regression	1.33×10^7	3.65×10^3	-0.0654	8.34×10^4	1.34×10^{11}

Analysing the estimates made by each regressor in Table F.1, one can notice some interesting differences between the methods. The SVR method tends to produce very similar predictions in all the testing results because it fits a relatively flat regression plane, which leads to minimal variations. Linear regression is the only model that predicts negative values, the exact definition of this regressor is shown in Equation (6.2). From this one can see that negative values can be obtained depending on the value of x and y encountered. Since the value of y can be negative, resulting in a negative contribution to ILF. Moreover, the factor for x is also negative, since x is always positive, this will always lead to a negative contribution to ILF. From a physical perspective, a negative ILF is never possible. However, this regressor is unable to capture that amount of detail. The Decision Tree regressor is the only one that predicts zero values. In total, it predicts an ILF of zero six times, of which one is correct. The random forest performs the best on predicting, it does not predict any zero values but it moves along the most accurate with the actual ILF values found.

6.2.3. Parameter Importance Evaluation

For the linear regression and random forest regression, information can be extracted on how the ML method obtains its results or which feature is found to be of importance. Therefore, these two methods will be analysed based on the obtained findings. Moreover, these two are also found to be the most accurate based on MSE and therefore could contain interesting information.

The coefficients of the linear regression model are extracted to derive an explicit formula to predict ILF [MN]:

$$y = 17717.77 + (-0.9404) \cdot x + 0.0022 \cdot y + 0.8067 \cdot IC \tag{6.2}$$

In this formula, the negative factor for x confirms what has been previously found. The further the turbines are downstream, the lower ILF. However, this formula does not take into account that this only holds when a turbine is placed behind another. Therefore, it is important to note that this only holds in the given domain of x that is used throughout the simulations. In this formula, y has a relatively small factor. This is mainly because the variation along y for the same x is smaller further down the wind farm. The factor for IC might be higher, but the term has a smaller contribution. Since the value range of IC if from 50-80% the overall difference in the estimate is smaller compared to x and y.

Additionally, feature importances from the random forest regressor are extracted to understand which variables influenced the prediction the most. The importance of the characteristic are: x: 43%, y: 39% and IC = 18%. This clearly shows that the position of the turbine in the farm is more important than the concentration of ice. Important to note is that this again only holds for the given domain and taken into account the owf layouts. The findings from these regressor models do align with the conclusion drawn when analysing the ILF, ILCF and return period. Therefore, one can conclude that these regressors are good at identifying this relationship between parameters. However, the accuracy of the predictions still leaves room for improvement. A better prediction could be made if more data is available or by using more complex ML methods such as neural networks and deep learning methods.

7

Discussion and Recommendations

This chapter will discuss the decisions that are made throughout this thesis. First, the environmental conditions used from the Baltic Sea are discussed. Then the performed simulation in SAMS are considered followed by the processing of the force data. Finally, all obtained results are summarised and recommendations for further research are given.

7.1. Sea-Ice and Environmental Conditions in the Northern Baltic Sea

An important part of this thesis is to obtain a realistic ice field that is used for ice load simulations. To establish this first the environmental conditions are considered and the ice fields in this area are analysed.

First, based on image processing, different FSDs can be determined. In this thesis, multiple ice field sizes are used to gain a better general understanding of the distribution present in the northern Baltic Sea. This shows that the FSD can greatly vary over time, not only over the years but also over the months. Therefore, it is difficult to capture or define one sea-ice state as it is an evolving process. By using different years and different area sizes, this is taken into account, giving a general power law factor which is usedc in simulations.

Image processing of sea-ice is a complicated process, as it can be challenging to identify cracks and lighter ice. Therefore, an existing image processing algorithm has been used to ensure accurate results. Ideally, the input for these kind of methods is very high-resolution images, which enhance the accuracy of the used method. However, since the main interest in the floe fields was on the bigger floes, it is decided to use a normal resolution. This means that generally the larger floes are identified accurately, which is of main importance on the scales that are worked with.

The velocity of the ice with which it moves into the OWF is mainly governed by the wind and current. Therefore, obtaining these environmental conditions is important to ensure a realistic ice drift speed. The current in the Baltic is found to be highly varying in both direction and magnitude. It is decided to assume a relatively low current velocity in the same direction as the wind. However, in reality, the wind and current direction rarely align. Generally, the influence of the current on the magnitude and direction of the ice drift is less than that of the wind. Nevertheless, adding a varying current could potentially provide some sideward momentum to the ice floes after interacting with turbines. Potentially influencing the number of interactions that occur.

Wind data from the northern Baltic Sea provides information regarding the mean velocity and direction. Considering the varying directions of the wind in this area, one can see that this is a potential factor of interest. The mean wind speed is found to be relatively low, therefore the wind speed for the simulation is based on the relevant design code. Given the rated wind speed for the turbine, an estimate of 10 m/s wind speed at 10 m above the ice is used. A more accurate approach would be to use the exponential decay of the wind profile. This would yield lower wind speeds than now simulated. Furthermore, a

constant wind speed and direction is now assumed for the full simulation duration (12.5 hours). This is not a realistic assumption in reality, from an engineering perspective it can be used prescribing a single wind speed. However, for gaining insight into a more realistic ice-OWF interaction, varying wind speed and direction could be of interest.

7.2. SAMS Simulation Considerations

After obtaining more insight into the environmental conditions in the northern Baltic Sea, the simulation criteria are defined. First, the ice field is generated on the basis of the previous FSD found. The power-law factor is defined on the basis of the average of all the analysed ice fields. For generating an ice field the minimum MCD of the smallest ice field that is studied is used. Considering the ice field generating algorithm, using the maximum value of this field was not satisfactory. The usage of inverse transform sampling generally would yield mostly smaller floes. Therefore, a maximal MCD is determined using multiple iterations. It is important to note that the maximal MCD used (20 km) is larger than the simulated ice field (15x15 km). However, using this value does influence the floe sizes that are generated using the floe size generator, leading to more satisfactory results similar to the results obtained from image processing.

The size of the ice field is found to be an important parameter. First, it has an impact on the number of floes that are present in the ice field. Generally, more floes result into an increase in computational times since more total interactions are occurring. Which becomes even more significant for higher ice concentrations. Furthermore, the size of the field is relevant for the confinement that is used. If the confinement is placed very close to the OWF edges, the ice is more locked into place than would naturally be the case. When this occurs, the ice is significantly restricted in its movement, which influences the drift in and around the OWF. These considerations eventually resulted in using an ice field of 15x15 km. Smaller ice fields are found to be more heavily influenced by the confinement restricting the ice movement significantly. This was clearly noticeable when initially using a 10x10 km ice field.

As previously mentioned, the floe size generator uses a higher maximal MCD than is physically possible for the created ice field. This size generator uses inverse transverse sampling to create floe sizes stochastically. There are some downsides to this method that are important to consider. This method of creating the ice field does not take into account the dimensions of the ice field. Therefore, when generating floe sizes, it is possible that floes are generated that cannot be placed in the ice field. This is mainly the case for higher ice concentrations. Eventually, this leads to the placement of more smaller floes in the generated field. Since floes that do not fit into the domain are discarded. This yields a higher power law factor then initially used for sampling the floe sizes. Therefore, this method creates a difference in the actual FSD compared to the power law factor that is desired to generate. Since the FSD generally changes over time and is not a constant factor over time this is considered to be acceptable. The range of these new values for alpha are still in line with the values found from literature and therefore not considered as problematic or unrealistic.

To ensure realistic ice-ice and ice-structure interaction, the ice properties are of great importance. One of the governing parameter for ice forces is the ice thickness, this value is determined using historical data and taking the 50 year value as suggested from a design perspective. The ice thickness is uniform for each floe, which in reality is not the case. Fluctuating ice thickness over the ice floes could influence the ice movement, since the mass of the floes is not uniformly distributed with the size. The significance of this effect depends mainly on the magnitude of thickness fluctuations. Since it is assumed that there are no ridges, these fluctuations in ice thickness are likely to be small and are not relevant for this research scope. Furthermore, it should be noted that global warming effects could influence the ice thickness in the future. Therefore, using an ice thickness based on historical data might not give accurate prediction for future expected ice loads. However, this is considered beyond the scope of this project and should be considered individually in design codes.

The other ice properties used in this simulation are based on common ice engineering values and field measurement. One of the key differences in the Baltic Sea compared to the Arctic is a considerably lower water salinity. This lower salinity in the Baltic Sea also influences the salinity of the ice, which affects various ice properties. However, little data are available on these ice properties or ice salinity in the Baltic. This makes it difficult to adjust each ice property accurately. More data and testing of the

ice properties in the Baltic could improve the precision of the results obtained.

To simulate the ice forces on the structure, the structure itself is also of importance. In this case these are individual turbines placed in a grid-like layout. The turbine support structures have a diameter of 10 m as found in previous studies. They are modelled as fully rigid and therefore do not deform or deflect. In reality, this would be the case. For a more realistic ice-structure interaction this could be taken into account. However, this is beyond the scope of this thesis. Moreover, this would increase the computational times even more making it more time consuming to obtain data.

One of the main limitations encountered during the simulations was the computational time of the simulations in SAMS. This is the reason to limit the simulation time to 45.000 s. Initially, the entire ice field passing through the OWF was of interest. However, this was not feasible considering the computational speed of SAMS. This influences the result since only a part of the ice field has interacted with the OWF. Therefore, certain interaction phenomenon might not have been captured or only partially.

From analysing the simulation times it was found that the computational time is not solely governed by the ice concentration or the amount of floes. Another influential factor is the ice-structure interaction that occurs. When limit force occurs, it is found to slow down the simulation. The same holds when radial and circumferential cracking is initiated for larger floes. Furthermore, it was found that SAMS does not use all available computational power, which can lead to longer computational times. Optimising it for GPU usage could therefore lead to more efficient computing. Combining this with the usage of super computers would be beneficial and positively impact the modelling opportunities.

7.3. Processing of the Obtained Force Data

After completing all the simulations, the results are processed and need to be compared to each other. The main data of interest are the force time series in the horizontal plane (x,y direction). Previous literature has been studied to find potential ways of analysing and summarising these time series such that they are easy to compare and interpret. None of these methods was fully sufficient for this specific purpose. Therefore, a combination of methods has been used.

First, a threshold of 100 kN is used to filter out all low values. This value is selected to filter out all less significant load peaks that occur in the time series. One could decide to reduce this threshold depending on the key interest for analysis. In this study, the main interest is studying the general loads but also focussing on higher load peaks and how often these peaks occur at different locations in the wind farm. Inspired by the Rayleigh Separation method, this threshold is decided to result in a good balance in analysing general loads over time while not taking into account every small interaction or load.

Furthermore, when analysing the time series, one can observe high spikes in the forces. Some of these force spikes are not physical forces but the result of solving for momentum balance. Therefore, an upper limit of the forces is calculated based on the ISO norm. The SAMS software uses a different method to compute the forces. However, since the ISO formula is used to determine the highest peak loads, this formula is also used to determine the upper limit of the simulated forces. The application of this upper bound limit gives a greater certainty that the forces are physically accurate and are not based on solving numerically for the impulse.

After filtering all force data with an upper and lower bound. The data is summarised on the basis of a new defined factor. It uses the product of the number of cycles and the average load experienced. The number of cycles is determined using a rainflow counting method. It's the main goal is to describe the magnitudes and occurrences of forces over time. Therefore, time is involved in the two defined factors (ILF and ILCF). Both take into account the total amount of simulated seconds compared to either the total contact time or the time a turbine is potentially exposed to the ice field. This shows that these factors are interpretable as a force factor with a unit in Newton. It cannot be used directly for engineering purposes, but it is a starting point to compare loads in the OWF and for different scenarios.

It is important to note that the force data obtained from SAMS cannot be validated since no data is available for these kinds of conditions. The SAMS software has previously been validated for other use cases and simulations and is accurate. However, validation of ice loads on an OWF is currently not possible. Therefore, predictions are initially made based on a theoretical framework, and these are

looked at in more detail using the obtained data. Most important for this research objective is that the ice-structure interaction and movement is precise. The exact load levels are important on a general level. However, small errors in these loads will not greatly influence the obtained conclusions.

7.4. Summary of the Obtained Results

Based on the results obtained, some key findings are used to summarise all the results obtained. These will be elaborated on in Chapter 8.

- From the ILF one can conclude that the sum of the forces is reduced by at least 75% after interacting with the first line of turbines. The mean value is reduced by at least 70%. Therefore, a significantly lower ILF can be expected in turbines further downstream of the OWF for all ice concentrations and wind directions.
- Based on the actual interaction time ($t_{contact}$), it can be concluded that a wind angle of 0 and 15 degrees performs the best in reducing the interaction time with the turbines. These two angles result in the lowest mean and sum of the ILCF and additionally show the largest percentual decrease over contact time.
- Generally, one can conclude that an increase in ice concentration results in a decrease of turbines that have an ILF/ILCF of zero. Higher ice concentrations could lead to higher blockage effects, but also add more momentum to the ice field. This effect could be further investigated using different floe size ranges for different simulations. Moreover, by analysing the movement and velocities of the floes to gain more insight into the blockage effect.
- The usage of ML regressors is not found to be accurate enough to predict ice loads or optimise an OWF layout. More advanced methods and more data could make this more accurate and useful for the future of ice load prediction in OWFs.

7.5. Further Research and Recommendations

Since ice loads in offshore wind farms is a relative new research topic, various further research options are of interest.

First, one could perform more simulations with different ice fields. The main interesting parameter to change would be the floe sizes to see how this impacts the drift and ice action within the wind farm. In addition, one could change the environmental conditions to analyse different ice drift speeds. Furthermore, the rotational movement of the current can be used, as well as varying wind conditions over time. This simulates a more realistic environment and therefore more realistic ice drift.

Moreover, it could be of interest to investigate how the SAMS simulations can be optimised so that the simulation times get reduced. Optimising the software for GPU efficiency could give the opportunity to perform simulations using supercomputers. This would gain significantly more data giving more modelling opportunities to investigate the influence of different parameters and wind farm layouts. However, one could also explore the usage of physics-based machine learning methods to make faster predictions regarding the ice loads under different conditions. However, having sufficient training data would be a limiting factor in doing so.

One of the main challenges remains the lack of quality data. Therefore, for further research, it would be of interest to obtain data from model scale tests or full-scale data from load cells on existing wind turbines. This is the only way to validate the data obtained from simulations like these to ensure accuracy.

8

Conclusion

In this chapter, all sub-questions will be discussed and answered leading to the main conclusion.

Which methods can be developed to summarise and compare ice loads over time?

In literature, multiple methods are described to analyse load time series. In this thesis, three methods are discussed: Rayleigh Separation, Power Spectral Density (PSD) and Rainflow Counting. The PSD method is less useful since it does not give insight into the magnitude of the forces directly. Furthermore, it is more complex to compare these PSDs for each turbine for every scenario. Rayleigh Separation focusses mainly on identifying peaks in the load time series, the distribution of these peaks can then be analysed using a Weibull curve. However, for this fit, two parameters are obtained, making it difficult to compare the result from a physical perspective.

Rainflow counting gives a good starting point for developing a new method to analyse ice load time series. First, this method is applied to count the number of load cycles that occur. After doing so, an upper and lower threshold are set. Doing so ensures physical results and gives a main focus on ice interactions with a force higher than 100 kN. From these data, a load histogram is made with bins given a bin size of 0.5 MN. Combining the mean of this force bin and the number of rainflow counts gives insight into how much and how often forces are experienced. This is combined into the Ice Load Factor (ILF) and the Ice Load Contact Factor (ILCF).

Generally, the ILF sums up the product of the mean force and the number of cycles and divides these by the time the turbine could be exposed to the ice. This time is based on the free-drift speed of the ice and the position of the turbine. Multiplying with the total simulated time yields a unit of N for this factor. Generally, the exposed time decreases further down the wind farm. Therefore, a decrease in ILF always implies a decrease in the sum of the mean force and cycles. This decrease can be caused by either the magnitude of the force or the number of interactions that occur.

However, it does not give information on the actual interaction time that occurs. Therefore, the ILCF is defined using a similar approach. The main difference is that it divides by the sum of the contact time. This factor helps to gain insight into the actual interaction time of the ice with the turbines.

How do the ice loads change over the wind farm for different wind directions?

To analyse this, the wind farm has been rotated so that a different wind angle is simulated. This changes the individual spacing of the turbines, which could affect the ice interaction with the structures. Since the distance governs the sizes of the ice floes that can move through the first line of turbines. It is important to note that only the grid layout is investigated and that a change in wind direction for different layouts might lead to different results.

From the ILF results, it is very clear that the highest ice loads are encountered at the first line of turbines regardless of the wind direction. Moreover, for a wind heading of zero degrees the ice loads reduce the fastest for the next line of turbines for most ice concentrations. Furthermore, for a wind angle of 0 and 45 degrees, it occurs that the turbines are behind another. This leads to certain turbines not

experiencing ice loads above the specified threshold of 100 kN. Since there is no sufficient sideward movement to the ice after a previous interaction, no significant loads are experienced by these turbines.

From the ILCF one concludes that the sum is the highest for a 30 degree wind angle. This wind angle also shows the lowest decrease in interaction time over the lines of turbines. Taking into account that the ILF sum is also highest for most of these wind angles (except scenario 2.3). It is concluded that the 30 degree wind angle gives the highest overall ice load on the wind farm. This could physically be caused by the turbines having the largest offset in the y-direction from one another. This makes it more likely that the ice that moves through the first line of turbines will interact again with the lines further downstream.

Furthermore, analysing the total contact time of the ice structure, it is concluded that a wind angle of 0 and 15 degrees performs the best in reducing the interaction time when moving further downstream. Generally, this yields considerate lower interaction times, which is of importance when designing for ice interaction. The ILCF sum and mean for these wind directions are generally the lowest. It can also be concluded that the least ice-interaction occurs over the windfarm for this wind angle.

What is the influence of the ice concentration on the ice loads experienced by each turbine in an OWF?

Increasing the ice concentration for the simulation increases the amount of floes. When interacting with the OWF this leads to possible more ice-structure interactions. Furthermore, the presence of more ice provides more sideward momentum for the ice movement after interacting with a structure. This means that the ice is pushed back behind the streamline of a structure faster for a higher ice concentration.

In general, an increase in ice concentration leads to a shorter return period for small ice loads. Since more ice is present, more interactions occur and they occur more frequently. Furthermore, one can also notice that the number of turbines that do not exceed the ice load threshold decreases as the ice concentration increases.

In what ways can machine learning be used to accurately predict ice loads?

The use of machine learning is limited to using regression models. In total, four different regressors are used and evaluated on their performance.

The random forest regressor is found to perform the best in predicting the ILF value. It performs the best according to MSE, RMSE, R^2 and total absolute error. However, significant errors are still encountered. This is potentially caused by the limited size of the dataset used for training and testing (400 data points). However, analysing the parameter importance obtained from both linear regression and the random forest regressor gives similarities to previously drawn conclusions. Therefore, it is found that it might not accurately predict the ILF, but it does give a general representation of the parameters that are important to influence this factor.

Generally, one can conclude that the random forest regressor is a good starting point but is not accurate enough to replace simulations. Training this regressor with more data could improve its accuracy. Furthermore, using more advanced ML methods, such as neural networks or physical-based methods, could improve accuracy.

Finally, the conclusion can be drawn to the main research question.

How is the ice loading on and ice drift around an offshore wind turbine influenced by it being part of an offshore wind farm

This question can be answered using the data of the simulated scenarios and the defined ILF and ILCF.

The force data obtained from the simulations clearly show that the ice loads change when moving further down the wind farm. To analyse this effect, the so-called ”Lines” of turbines are defined. The first line of turbines represents the main resistance to the ice field. All ice floes that are larger than the turbine spacing will interact with a structure and can only move passed after deformation occurs. From all simulations it is found that the mean ILF is decreased by >70% and the sum by >75% after interacting with the first line of turbines in all scenarios. Hence, significant reduction over the wind farm is present.

The first lines of turbines provide a shielding effect for the other turbines. This is mostly noticeable at a wind angle of 0 and 45 degrees for low ice concentrations. Given that there are turbines that do not encounter ice loads higher then the stated threshold of 100 kN. This effect is less strong when increasing the ice concentration since more blockage occurs and the amount of ice-ice interactions increase resulting in more sidewards momentum in the ice movement.

From the total contact time, $t_{contact}$, one can also clearly conclude that the interaction time significantly reduces over the wind farm when the ice moves further downstream. In general, this effect is the most present for a 0 and 15 degree wind heading. Furthermore, one concludes that the 30 degree wind angle yields the lowest reduction and therefore has the lowest ice-structure interaction blockage effect. This could potentially be caused by the fact that this angle has the highest offset in the position of the turbine in y-direction. Therefore, turbines in previous lines do not prevent other turbines further downstream to interact with the ice field.

The usage of ML regressors shows a similar relationship between the analysed parameters. The position of the turbines is the most important parameter when analysing the ILF and is generally reducing further downstream. Additionally, it is found that the ice concentration has a less significant impact.

References

Aïtcin, P.-C., Mindess, S., & Langley, W. (2016). 8 - the confederation bridge. In M. G. Alexander (Ed.), *Marine concrete structures* (pp. 199–214). Woodhead Publishing. https://doi.org/https://doi.org/10.1016/B978-0-08-100081-6.00008-8

Alstott, J., Bullmore, E., & Plenz, D. (2014). Powerlaw: A python package for analysis of heavy-tailed distributions. *PLoS One*, *9*(1), e85777.

Amzallag, C., Gerey, J., Robert, J., & Bahuaud, J. (1994). Standardization of the rainflow counting method for fatigue analysis. *International Journal of Fatigue*, *16*(4), 287–293. https://doi.org/https://doi.org/10.1016/0142-1123(94)90343-3

Anderson, D. (1958). Preliminary results and review of sea ice elasticity and related studies. *Transactions of the Engineering Institute of Canada*, *2*(3), 116–22.

Bak, C., Zahle, F., Bitsche, R., Kim, T., Yde, A., Henriksen, L. C., Natarajan, A., & Hansen, M. H. (2013). *Description of the dtu 10 mw reference wind turbine* (tech. rep. No. DTU Wind Energy Report-I-0092). DTU Wind Energy. Roskilde, Denmark. https://backend.orbit.dtu.dk/ws/portalfiles/portal/55645274/DTU_10MW_Reference_Turbine.pdf

Breiman, L. (2001). *Machine Learning*, *45*(1), 5–32. https://doi.org/10.1023/a:1010933404324

Breiman, L., Friedman, J. H., Olshen, R. A., & Stone, C. J. (1984). *Classification and regression trees*. Wadsworth International Group.

Brown, J. H., & Kingery, W. (1963). Elasticity and strength of sea ice. *Ice and snow*, 79–106.

Buckley, E. M., Cañuelas, L., Timmermans, M.-L., & Wilhelmus, M. M. (2024). Seasonal evolution of the sea ice floe size distribution in the beaufort sea from 2 decades of modis data. *The Cryosphere*, *18*(11), 5031–5043. https://doi.org/10.5194/tc-18-5031-2024

Butkovich, T. R. (1956). *Strength studies of sea ice* (Vol. 20). Snow Ice; Permafrost Research Establishment, Corps of Engineers, US Army.

Clauset, A., Shalizi, C. R., & Newman, M. E. J. (2009). Power-law distributions in empirical data. *SIAM Rev. Soc. Ind. Appl. Math.*, *51*(4), 661–703.

Cochran, W., Cooley, J., Favin, D., Helms, H., Kaenel, R., Lang, W., Maling, G., Nelson, D., Rader, C., & Welch, P. (1967). What is the fast fourier transform? *Proceedings of the IEEE*, *55*(10), 1664–1674. https://doi.org/10.1109/PROC.1967.5957

Davis, N. N., Badger, J., Hahmann, A. N., Hansen, B. O., Mortensen, N. G., Kelly, M., Larsén, X. G., Olsen, B. T., Floors, R., Lizcano, G., Casso, P., Lacave, O., Bosch, A., Bauwens, I., Knight, O. J., Potter van Loon, A., Fox, R., Parvanyan, T., Krohn Hansen, S. B., … Drummond, R. (2023). The global wind atlas: A high-resolution dataset of climatologies and associated web-based application. *Bull. Am. Meteorol. Soc.*, *104*(8), E1507–E1525.

DeFranco, S., Wei, Y., & Dempsey, J. (1991). Notch-acuity effects on the fracture toughness of saline ice. *Annals of Glaciology*, *15*, 230–235.

Denton, A. A., & Timmermans, M.-L. (2022). Characterizing the sea-ice floe size distribution in the canada basin from high-resolution optical satellite imagery. *The Cryosphere*, *16*(5), 1563–1578. https://doi.org/10.5194/tc-16-1563-2022

Det Norske Veritas. (2012). *DNV-RP-C203: Fatigue Design of Offshore Steel Structures* (tech. rep.). Det Norske Veritas (DNV). Høvik, Norway. https://rules.dnv.com/docs/pdf/DNV/codes/docs/2012-10/RP-C203.pdf

Drucker, H., Burges, C. J., Kaufman, L., Smola, A., & Vapnik, V. (1997). Support vector regression machines. *Advances in Neural Information Processing Systems*, 155–161.

Dykins, J. (1967). Tensile properties of sea ice grown in a confined system. *Physics of Snow and Ice, Bunyeido Printing Co., Japan*, *1*, 523–537.

Egan, T. (n.d.). Adélie penguins on ice floe in newcomb bay.

European Committee for Standardization. (2019, August). *Petroleum and natural gas industries Arctic offshore structures* (Standard). European Committee for Standardization. Brussels, BE.

European Commission. (n.d.). Renewable energy. https://energy.ec.europa.eu/topics/renewable-energy_en

Finnish Meteorological Institute. (2025). Sea currents in the baltic sea. https://en.ilmatieteenlaitos.fi/seacurrents

Frederking, R. J., & Barker, A. (2002). Friction of sea ice on steel for conditions of varying speeds. *Proceedings of the 12th International Offshore and Polar Engineering Conference*, ISOPE-I-02–118. https://onepetro.org/ISOPEIOPEC/proceedings-pdf/ISOPE02/All-ISOPE02/ISOPE-I-02-118/1880928/isope-i-02-118.pdf

Frederking, R., Shkhinek, K., & Barker, A. (2014). An overview of ice loads on structures. *Proceedings of the 22nd IAHR International Symposium on Ice*.

Gonzalez, R. C., Woods, R. E., & Eddins, S. L. (2003). *Digital image processing using matlab*. Prentice-Hall.

Gravesen, H., Jørgensen, L. B., Høyland, K. V., & Bicker, S. (2023). Ice drift and ice action on offshore wind farm structures. *Proceedings of the International Conference on Port and Ocean Engineering under Arctic Conditions*.

Grömping, U. (2009). Variable importance assessment in regression: Linear regression versus random forest. *The American Statistician*, *63*(4), 308–319. https://doi.org/10.1198/tast.2009.08199

Hammer, T. C., Willems, T., & Hendrikse, H. (2023). Dynamic ice loads for offshore wind support structure design. *Marine Structures*, *87*, 103335. https://doi.org/https://doi.org/10.1016/j.marstruc.2022.103335

Hastie, T., Tibshirani, R., & Friedman, J. (2009). *The elements of statistical learning: Data mining, inference, and prediction* (2nd). Springer.

Hendrikse, H. (2024). Ice engineering challenges for offshore wind development in the baltic sea. *27th IAHR International Symposium on Ice*.

Herman, A. (2010). Sea-ice floe-size distribution in the context of spontaneous scaling emergence in stochastic systems. *Phys. Rev. E*, *81*, 066123. https://doi.org/10.1103/PhysRevE.81.066123

Hoerner, S. (1965). *Fluid dynamic drag, practical information on aerodynamic drag and hydrodynamic resistance*. Hoerner Fluid Dynamics.

Holt, B., & Martin, S. (2001). The effect of a storm on the 1992 summer sea ice cover of the beaufort, chukchi, and east siberian seas. *J. Geophys. Res.*, *106*(C1), 1017–1032.

Horvat, C., & Tziperman, E. (2017). The evolution of scaling laws in the sea ice floe size distribution. *Journal of Geophysical Research: Oceans*, *122*(9), 7630–7650. https://doi.org/https://doi.org/10.1002/2016JC012573

Høyland, K. V. (2024). Ice actions on structures - tba4260 - compendium.

Inoue, J., Wakatsuchi, M., & Fujiyoshi, Y. (2004). Ice floe distribution in the sea of okhotsk in the period when sea□ice extent is advancing. *Geophysical Research Letters*, *31*(20). https://doi.org/10.1029/2004gl020809

International Electrotechnical Commission. (2019, April). Wind energy generation systems. *International Electrotechnical Commission*.

JCOMM Expert Team on Sea Ice. (2009). Wmo sea-ice nomenclature, wmo/omm/вмо - no.259 suppl.no.5. linguistic equivalents [WMO No. 259, Suppl. 5]. https://doi.org/10.25607/OBP-1530

Kass, M., Witkin, A., & Terzopoulos, D. (1988). Snakes: Active contour models. *International Journal of Computer Vision*, *1*(4), 321–331.

Kergomard, C. (1989). Analyse morphométrique de la zone marginale de la banquise polaire au nordouest du spitsberg à partir de l'imagerie spot panchromatique. *Bulletin de la Société Française de Photogrammétrie et de Télédétection*, *115*, 17–20.

Kohnen, H. (1972). Seismic and ultrasonic mesasurements on the sea ice of eclipse sound near pond inlet, nwt, on northern baffin island. *Polarforschung*, *42*(2), 66–74.

Kuehn, G. A., Lee, R. W., Nixon, W. A., & Schulson, E. M. (1990). The structure and tensile behavior of first-year sea ice and laboratory-grown saline ice. *Journal of Offshore Mechanics and Arctic Engineering*, *112*(4), 357–363. https://doi.org/10.1115/1.2919878

Kujala, P., Suominen, M., & Riska, K. (2009). Statistics of ice loads measured on mt uikku in the baltic. *Proceedings of the International Conference on Port and Ocean Engineering Under Arctic Conditions 2009, POAC*, *09-51*.

Lambregts, F. (2024). *Interaction effects between sea-ice and offshore wind farm foundations; a preliminary study on the ice engineering challenges* (tech. rep.). Norwegian university of science and technology.

Langleben, M. P., & Pounder, E. (1963). *Elastic parameters of sea ice*. Massachusetts Institute of Technology.

Langleben, M. (1959). Some physical properties of sea ice. ii. *Canadian journal of Physics*, *37*(12), 1438–1454.

Lee, S. J., Jung, K. H., Ku, N., & Lee, J. (2023). A comparison of regression models for the ice loads measured during the ice tank test. *Brodogradnja*, *74*(3), 1–15.

Lee, Y.-L., Barkey, M. E., & Kang, H.-T. (2011). Metal fatigue analysis handbook. Butterworth-Heinemann.

Lensu, M. (1990). The fractality of sea ice cover. *Proceedings of IAHR Ice Symposium*, 300–313.

Leppäranta, M. (2005). *The drift of sea ice*. Springer Berlin Heidelberg. https://doi.org/10.1007/b138386

Leppäranta, M. (2011, January). *The drift of sea ice* (2nd ed.). Springer.

Leppäranta, M., & Omstedt, A. (1990). Dynamic coupling of sea ice and water for an ice field with free boundaries. *Tellus A*, *42*(4), 482.

Lu, P., Li, Z., Cheng, B., & Leppäranta, M. (2011). A parameterization of the ice□ocean drag coefficient. *J. Geophys. Res.*, *116*(C7).

Lubbad, R., Løset, S., Lu, W., Tsarau, A., & van den Berg, M. (2018a). Simulator for arctic marine structures (sams). *Volume 8: Polar and Arctic Sciences and Technology; Petroleum Technology*. https://doi.org/10.1115/omae2018-78592

Lubbad, R., Løset, S., Lu, W., Tsarau, A., & van den Berg, M. (2018b). An overview of the oden arctic technology research cruise 2015 (OATRC2015) and numerical simulations performed with SAMS driven by data collected during the cruise. *Cold Reg. Sci. Technol.*, *156*, 1–22.

Malmgren, F. (1927). On the properties of sea-ice: Norwegian north polar expedition with the maud, 1918-1925, sci.

Matsushita, M. (1985). Fractal viewpoint of fracture and accretion. *J. Phys. Soc. Jpn.*, *54*(3), 857–860.

Menge, J. R., & Jones, K. (1993). The tensile strength of first-year sea ice. *Journal of Glaciology*, *39*(133), 609–618.

Nakawo, M. (1983). Displacement method for determining sea ice density. *Cold Regions Science and Technology*, *9*, 45–50.

NASA Ice. (2018). A large sea ice ridge casts a shadow on the ice.

Neumann, G. (1952). *On wind generated ocean waves with special reference to the problem of wave forecasting* [Prepared under a contract sponsored by the Office of Naval Research, Washington, D.C. ; Preliminary distribution]. New York University, College of Engineering, Dept. of Meteorology. https://doi.org/10.5962/bhl.title.39389

Ochi, M. (1990). *Applied probability & stochastic processes in engineering & physical sciences*. John Wiley & Sons.

Pedregosa, F., Varoquaux, G., Gramfort, A., Michel, V., Thirion, B., Grisel, O., Blondel, M., Prettenhofer, P., Weiss, R., Dubourg, V., Vanderplas, J., Passos, A., Cournapeau, D., Brucher, M., Perrot, M., & Duchesnay, É. (2011). Scikit-learn: Machine learning in python. *Journal of Machine Learning Research*, *12*, 2825–2830.

Peschanskii, I. (1960). Arctic and antarctic sea ice (r). *Problemy Arktiki i Antarktiki*, *4*, 111–129.

Peyton, H. (1963). Some mechanical properties of sea ice. In W. Kingery (Ed.), *Ice and snow-processes, properties and applications* (pp. 107–113). MIT Press.

Peyton, H. (1966). *Sea ice strength* (tech. rep. No. UAG-182). University of Alaska, Geophysical Institute. Fairbanks, AK, USA.

Pounder, E. R., & Little, E. (1959). Some physical properties of sea ice. i. *Canadian Journal of Physics*, *37*(4), 443–473.

Pounder, E., & Stalinski, P. (1960). General properties of arctic sea ice. *Paper to be presented to International Union of Geodesy and Geophysics*, 25–34.

Ross, S. M. (2022, December). *Simulation* (6th ed.). Academic Press.

Rothrock, D. A., & Thorndike, A. S. (1984). Measuring the sea ice floe size distribution. *Journal of Geophysical Research: Oceans*, *89*(C4), 6477–6486. https://doi.org/https://doi.org/10.1029/JC089iC04p06477

Sanderson, T. (1988). *Ice mechanics and risks to offshore structures*. Springer Netherlands.

Schulson, E. M., & Fortt, A. L. (2012). Friction of ice on ice. *J. Geophys. Res.*, *117*(B12).

Shen, W., & Lin, S.-Z. (1988). Fracture toughness of bohai bay sea ice. *J. Offshore Mech. Arct. Eng. Trans. ASME*, *110*(4), 409–413.

Sinha, N. K. (1986). Young arctic frazil sea ice: Field and laboratory strength tests. *Journal of Materials Science*, *21*, 1533–1546.

Sinha, N. K. (1984). Uniaxial compressive strength of first-year and multi-year sea ice. *Canadian Journal of Civil Engineering*, *11*(1), 82–91.

Snyder, J. P. (1987). *Map projections: A working manual*. U.S. Geological Survey Professional Paper 1395.

Soh, L.-K., Tsatsoulis, C., & Holt, B. (1998). Identifying ice floes and computing ice floe distributions in SAR images. In *Analysis of SAR data of the polar oceans* (pp. 9–34). Springer-Verlag.

Steer, A., Worby, A., & Heil, P. (2008). Observed changes in sea-ice floe size distribution during early summer in the western weddell sea. *Deep Sea Research Part II: Topical Studies in Oceanography*, *55*(8–9), 933–942. https://doi.org/10.1016/j.dsr2.2007.12.016

Su, B., Riska, K., & Moan, T. (2011). Numerical simulation of local ice loads in uniform and randomly varying ice conditions. *Cold Regions Science and Technology*, *65*(2), 145–159. https://doi.org/https://doi.org/10.1016/j.coldregions.2010.10.004

Suominen, M., Kujala, P., Romanoff, J., & Remes, H. (2017). Influence of load length on short-term ice load statistics in full-scale. *Marine Structures*, *52*, 153–172. https://doi.org/https://doi.org/10.1016/j.marstruc.2016.12.006

Suominen, M., Li, F., Lu, L., Kujala, P., Bekker, A., & Lehtiranta, J. (2020). Effect of maneuvering on ice-induced loading on ship hull: Dedicated full-scale tests in the baltic sea. *Journal of Marine Science and Engineering*, *8*(10). https://doi.org/10.3390/jmse8100759

Tikanmäki, M. (2024). Trends in ice conditions in the gulf of bothnia: Case study with channel markers. *27th IAHR International Symposium on Ice, 2024*.

Timco, G. W., & Weeks, W. F. (2010). A review of the engineering properties of sea ice. *Cold Reg. Sci. Technol.*, *60*(2), 107–129.

Timco, G. W., & Frederking, R. M. W. (1983). Flexural strength and fracture toughness of sea ice. *Cold Regions Science and Technology*, *8*(1), 35–41.

Timco, G. W., & Frederking, R. M. (1986). Confined compression tests: Outlining the failure envelope of columnar sea ice. *Cold Regions Science and Technology*, *12*(1), 13–28.

Timco, G., et al. (1994). Flexural strength equation for sea ice. *Cold regions science and technology*, *22*(3), 285–298.

Timco, G., & Frederking, R. (1990). Compressive strength of sea ice sheets. *Cold Regions Science and Technology*, *17*(3), 227–240.

Timco, G., & Frederking, R. (1991). Seasonal compressive strength of beaufort sea ice sheets. *Ice-Structure Interaction: IUTAM/IAHR Symposium St. John's, Newfoundland Canada 1989*, 267–282.

Timco, G., & Frederking, R. (1996). A review of sea ice density. *Cold Regions Science and Technology*, *24*(1), 1–6. https://doi.org/10.1016/0165-232x(95)00007-x

Toyota, T., & Enomoto, H. (2002–December 6). Analysis of sea ice floes in the sea of okhotsk using adeos/avnir images. *Ice in the Environment: Proceedings of the 16th IAHR International Symposium on Ice*.

Toyota, T., Haas, C., & Tamura, T. (2011). Size distribution and shape properties of relatively small sea-ice floes in the antarctic marginal ice zone in late winter. *Deep Sea Res. Part 2 Top. Stud. Oceanogr.*, *58*(9-10), 1182–1193.

Toyota, T., Takatsuji, S., & Nakayama, M. (2006). Characteristics of sea ice floe size distribution in the seasonal ice zone. *Geophysical Research Letters*, *33*(2). https://doi.org/10.1029/2005gl024556

Tsarau, A., van den Berg, M., Lu, W., Lubbad, R., & Løset, S. (2018). Modelling results with a new simulator for arctic marine structures – sams [Paper No. OMAE2018-78593]. *Proceedings of the ASME 2018 37th International Conference on Ocean, Offshore and Arctic Engineering (OMAE2018)*.

Urabe, N., & Inoue, M. (1988). Mechanical properties of antarctic sea ice. *J. Offshore Mech. Arct. Eng. Trans. ASME*, *110*(4), 403–408.

Urabe, N., Iwasaki, T., & Yoshitake, A. (1980). Fracture toughness of sea ice. *Cold Regions Science and Technology*, *3*(1), 29–37.

van den Berg, M., Lubbad, R., & Løset, S. (2019). The effect of ice floe shape on the load experienced by vertical-sided structures interacting with a broken ice field. *Mar. Struct.*, *65*, 229–248.

Velarde, J. (2016). NTNU Open: Design of Monopile Foundations to Support the DTU 10 MW Offshore Wind Turbine — hdl.handle.net.

Weeks, W., & Assur, A. (1968). The mechanical properties of sea ice. *Proceedings, Conference on Ice Pressures Against Structures*, 25–78.

Weeks, W. F., & Lee, O. S. (1958). Observations on the physical properties of sea-ice at hopedale, labrador. *Arctic*, *11*(3), 134–155.

Weiss, J. (2003). Scaling of fracture and faulting of ice on earth. *Surv. Geophys.*, *24*(2), 185–227.

Williams, N. (2018). 'Never seen anything like that': Ice cut into patterns by P.E.I.'s Confederation Bridge.

Yong, Z., & Shengli, Q. A Practical Optimization for Offshore Wind Farm Layout. In: In *Wind Europe 2016*. 2016.

Yu, S., Zhang, D., Wang, S., Wang, G., Wang, G., Yue, Q., & Li, G. (2020). Field Monitoring of Offshore Wind Turbine Foundations in Ice Regions. *Journal of Coastal Research*, *104*(sp1), 343–350. https://doi.org/10.2112/JCR-SI104-063.1

Yue, Q., Qu, Y., Bi, X., & Tuomo, K. (2007). Ice force spectrum on narrow conical structures. *Cold Regions Science and Technology*, *49*(2), 161–169. https://doi.org/https://doi.org/10.1016/j.coldregions.2007.02.002

Zhang, Q., & Skjetne, R. (2014). Image processing for identification of sea-ice floes and the floe size distributions. *IEEE Transactions on geoscience and remote sensing*, *53*(5), 2913–2924.

Zhang, Q., & Skjetne, R. (2018). *Sea ice image processing with matlab®* [First edition]. CRC Press.

Zhang, Y., & Qian, S. (2016). A practical optimization for offshore wind farm layout [Renowind Energy Technology (Beijing) Co., Ltd.; Dx wind Technologies (Beijing) Co., Ltd.]. *Proceedings of the WindEurope Conference*.

Zhou, L., Cai, J., & Ding, S. (2023). The identification of ice floes and calculation of sea ice concentration based on a deep learning method. *Remote Sensing*, *15*(10). https://doi.org/10.3390/rs15102663

A

Ice Field Images

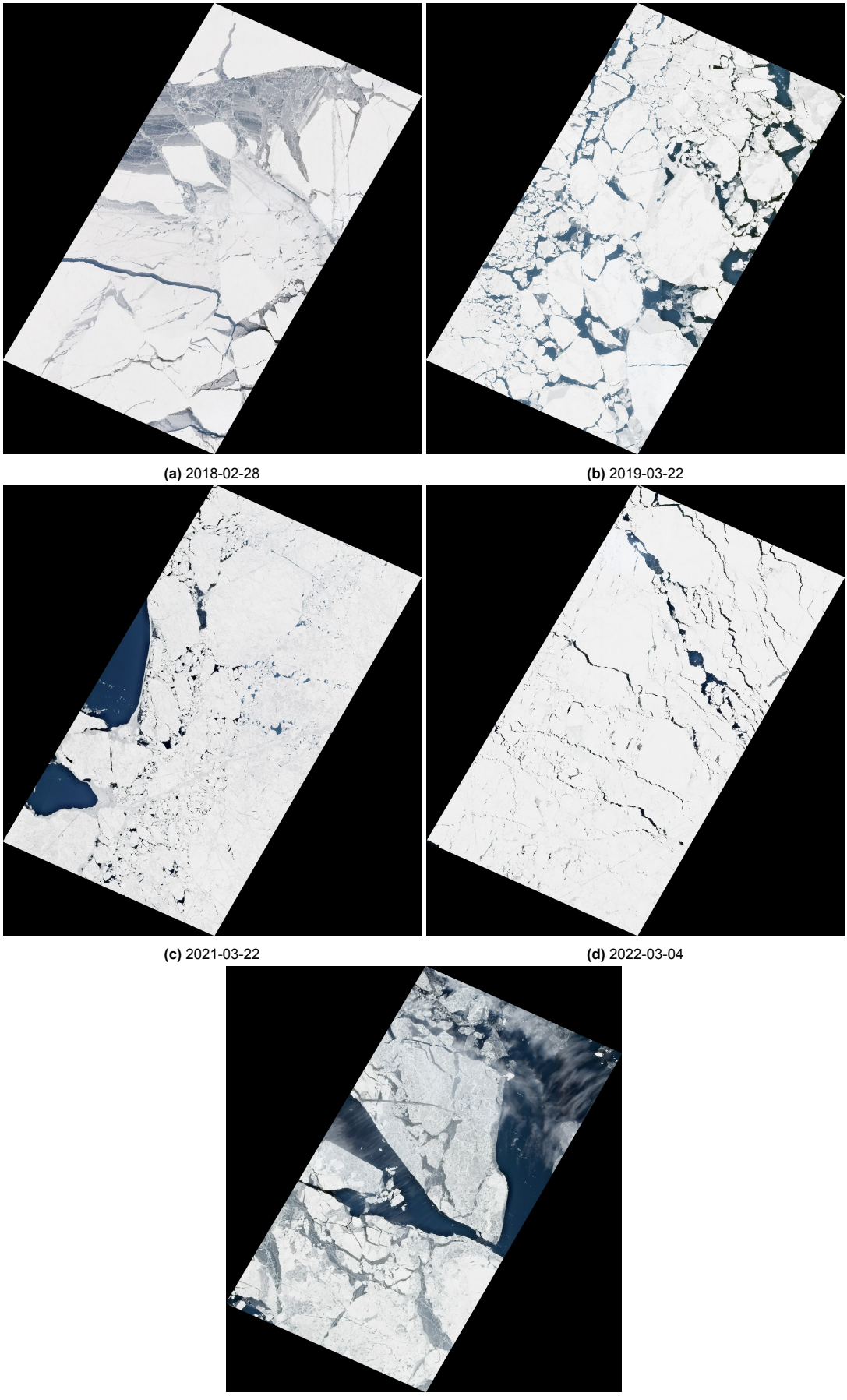

(a) 2018-02-28

(b) 2019-03-22

(c) 2021-03-22

(d) 2022-03-04

(e) 2023-04-21

Figure A.1: Ice fields with an area of 1500 km^2.

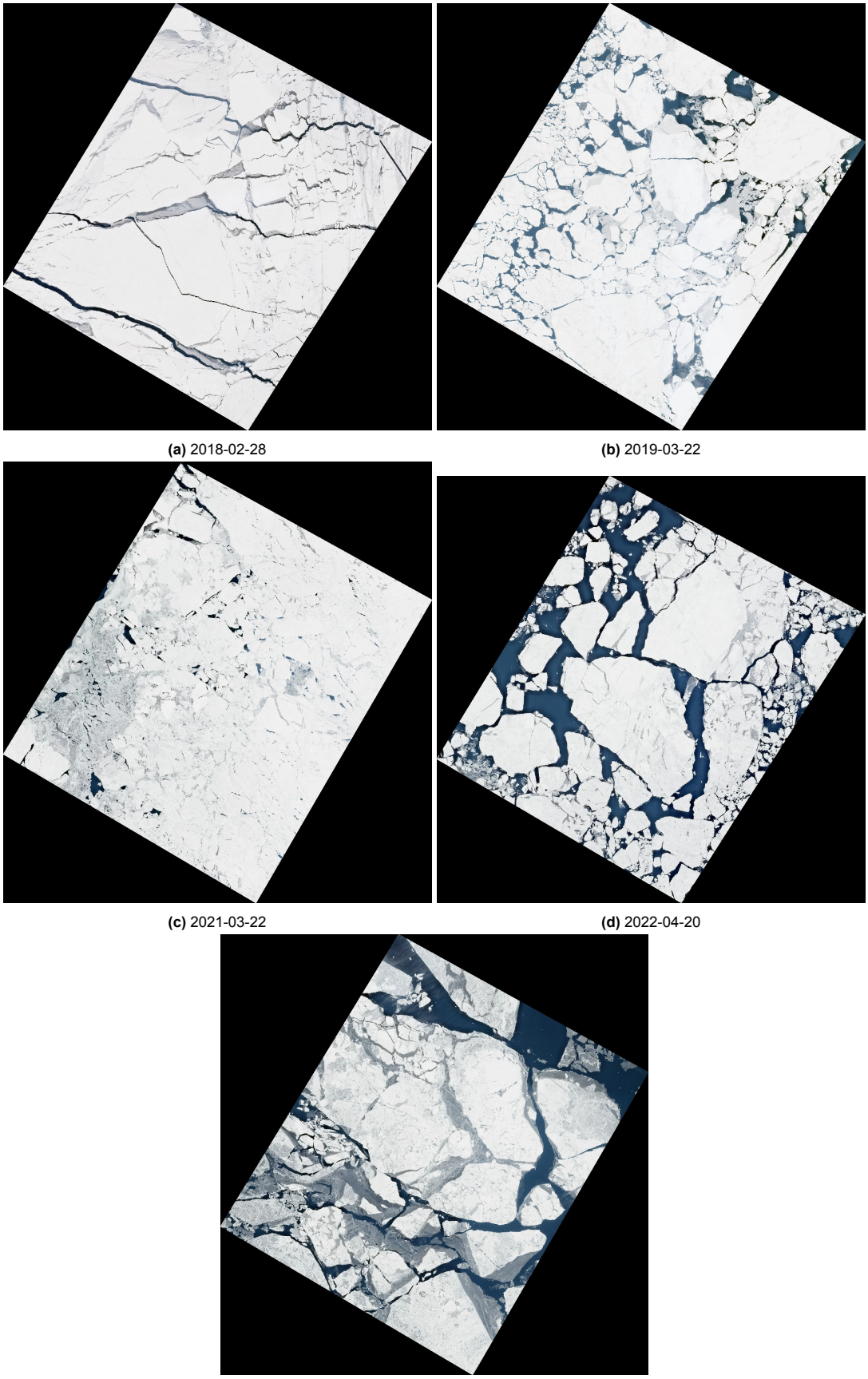

(a) 2018-02-28

(b) 2019-03-22

(c) 2021-03-22

(d) 2022-04-20

(e) 2023-04-21

Figure A.2: Ice fields with an area of 2500 km^2.

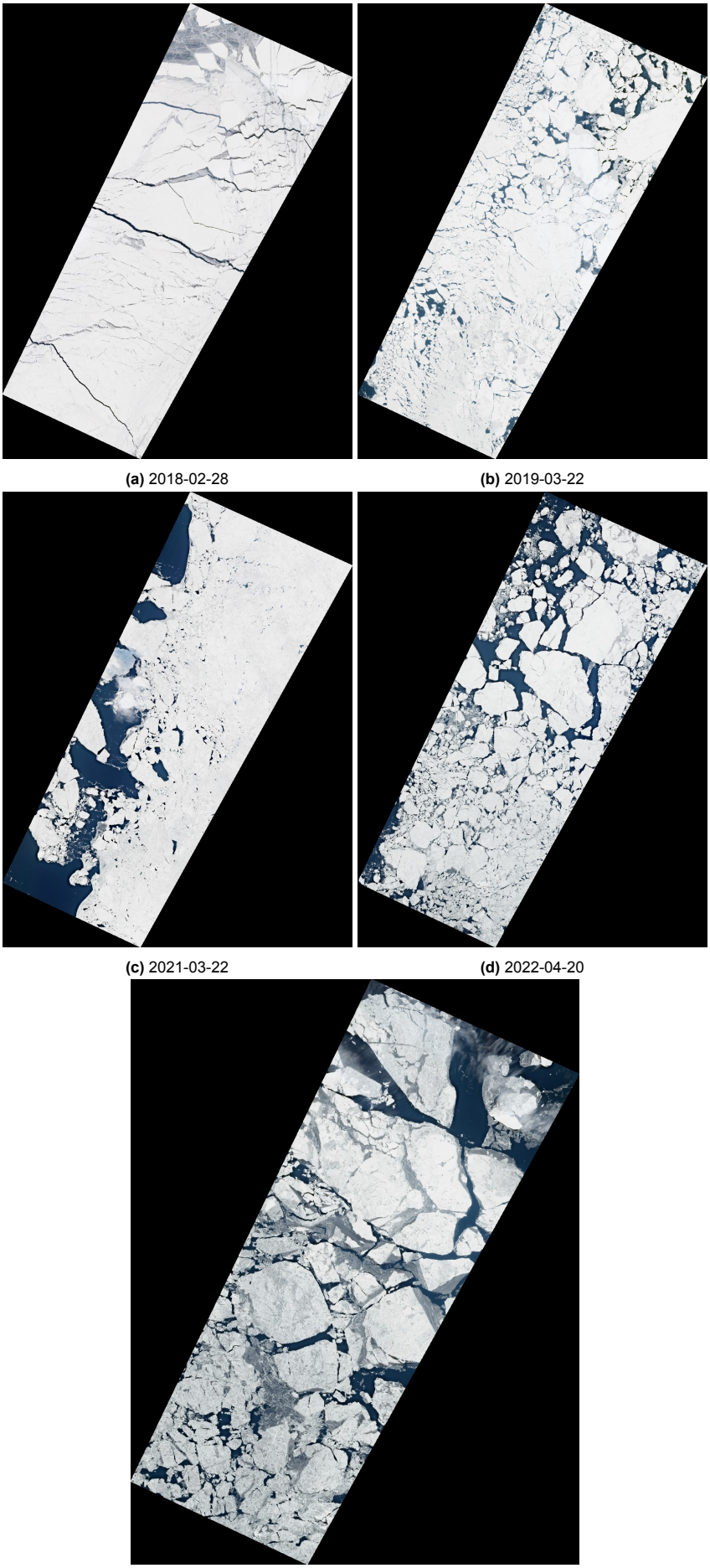

(a) 2018-02-28 **(b)** 2019-03-22

(c) 2021-03-22 **(d)** 2022-04-20

(e) 2023-04-21

Figure A.3: Ice fields with an area of 6100 km^2.

B

Power Law Derivation

Derivation of C

Given the probability density function $p(x) = C \cdot x^{-\alpha}$, determine C using the normalization condition for PDFs:

$$\int_{x_{\text{min}}}^{x_{\text{max}}} p(x)\,dx = 1 \tag{B.1}$$

Substituting the given form of $p(x)$:

$$\int_{x_{\text{min}}}^{x_{\text{max}}} C \cdot x^{-\alpha}\,dx = 1 \tag{B.2}$$

Factoring out the constant C:

$$C \int_{x_{\text{min}}}^{x_{\text{max}}} x^{-\alpha}\,dx = 1 \tag{B.3}$$

The integral of $x^{-\alpha}$ is:

$$\int x^{-\alpha}\,dx = \frac{x^{1-\alpha}}{1-\alpha} \quad \text{(for } \alpha \neq 1\text{)} \tag{B.4}$$

Substituting this into the equation:

$$C \left[\frac{x^{1-\alpha}}{1-\alpha} \right]_{x_{\text{min}}}^{x_{\text{max}}} = 1 \tag{B.5}$$

Evaluating the limits:

$$C \left(\frac{x_{\text{max}}^{1-\alpha} - x_{\text{min}}^{1-\alpha}}{1-\alpha} \right) = 1 \tag{B.6}$$

Solving for C:

$$C = \frac{1-\alpha}{x_{\text{max}}^{1-\alpha} - x_{\text{min}}^{1-\alpha}} \tag{B.7}$$

Thus, the value of C is:

$$C = \frac{1-\alpha}{x_{\text{max}}^{1-\alpha} - x_{\text{min}}^{1-\alpha}} \tag{B.8}$$

Inverse Transform Sampling Derivation

Given the probability density function (PDF):

$$p(x) = C \cdot x^{-\alpha}, \quad x_{\min} \leq x \leq x_{\max}$$

where C is the normalizing constant:

$$C = \frac{1-\alpha}{x_{\max}^{1-\alpha} - x_{\min}^{1-\alpha}}$$

To find the cumulative distribution function (CDF), integrate the PDF from $x_{\min}$ to x:

$$F(x) = \int_{x_{\min}}^{x} C \cdot x'^{-\alpha}\, dx' \tag{B.9}$$

Substituting C into the equation:

$$F(x) = \int_{x_{\min}}^{x} \frac{1-\alpha}{x_{\max}^{1-\alpha} - x_{\min}^{1-\alpha}} \cdot x'^{-\alpha}\, dx' \tag{B.10}$$

One now computes the integral of $x'^{-\alpha}$:

$$\int x'^{-\alpha}\, dx' = \frac{x'^{1-\alpha}}{1-\alpha}$$

Thus, the CDF becomes:

$$F(x) = \frac{1-\alpha}{x_{\max}^{1-\alpha} - x_{\min}^{1-\alpha}} \cdot \frac{x^{1-\alpha} - x_{\min}^{1-\alpha}}{1-\alpha} \tag{B.11}$$

Simplifying this expression gives:

$$F(x) = \frac{x^{1-\alpha} - x_{\min}^{1-\alpha}}{x_{\max}^{1-\alpha} - x_{\min}^{1-\alpha}} \tag{B.12}$$

For inverse transform sampling,$F(x) = u$ must be satisfied, where u is a random variable uniformly distributed between 0 and 1. Therefore, we solve for x:

$$\frac{x^{1-\alpha} - x_{\min}^{1-\alpha}}{x_{\max}^{1-\alpha} - x_{\min}^{1-\alpha}} = u \tag{B.13}$$

Now solve for $x^{1-\alpha}$:

$$x^{1-\alpha} = u \cdot (x_{\max}^{1-\alpha} - x_{\min}^{1-\alpha}) + x_{\min}^{1-\alpha} \tag{B.14}$$

Finally, solve for x:

$$x = \left[u \cdot (x_{\max}^{1-\alpha} - x_{\min}^{1-\alpha}) + x_{\min}^{1-\alpha}\right]^{\frac{1}{1-\alpha}} \tag{B.15}$$

Thus, to generate a random sample x from the distribution:

$$x = \left[u \cdot (x_{\max}^{1-\alpha} - x_{\min}^{1-\alpha}) + x_{\min}^{1-\alpha}\right]^{\frac{1}{1-\alpha}} \tag{B.16}$$

where u is a random variable uniformly distributed between 0 and 1.

C

Statistical Analysis of ILF for Each Line of Turbines

Table C.1: Statistical analysis of ILF [MN] for each line of turbines (IC = 50%).

Angle	Line	Length	Min	Max	Mean	Std	Sum
0°	1	5	91.62	9.35×10^3	3.49×10^3	3.77×10^3	1.74×10^4
	2	5	0.00	131.65	59.83	47.25	299.17
	3	5	0.00	46.86	13.83	18.58	69.14
	4	5	0.00	40.65	10.84	15.80	54.22
	5	5	0.00	28.39	6.81	11.01	34.06
15°	1	9	42.93	1.30×10^4	1.99×10^3	3.98×10^3	1.79×10^4
	2	7	81.74	430.56	219.42	131.70	1.54×10^3
	3	5	78.01	770.93	276.77	255.15	1.38×10^3
	4	3	25.82	698.87	279.84	298.52	839.51
	5	1	70.70	70.70	70.70	0.00	70.70
30°	1	9	120.66	3.13×10^4	6.37×10^3	1.02×10^4	5.73×10^4
	2	7	33.33	466.46	257.48	159.52	1.80×10^3
	3	5	30.57	305.92	167.82	88.96	839.08
	4	3	60.39	143.78	108.59	35.27	325.77
	5	1	65.68	65.68	65.68	0.00	65.68
45°	1	9	122.74	1.20×10^4	3.26×10^3	4.08×10^3	2.93×10^4
	2	7	2.01	191.10	95.08	68.61	665.56
	3	5	0.00	62.76	28.28	20.42	141.42
	4	3	0.00	4.21	2.52	1.81	7.55
	5	1	0.00	0.00	0.00	0.00	0.00

Table C.2: Statistical analysis of ILF [MN] for each line of turbines (IC = 60%).

Angle	Line	Length	Min	Max	Mean	Std	Sum
0°	1	5	321.65	1.12×10^4	4.44×10^3	4.60×10^3	2.22×10^4
	2	5	110.42	522.17	348.30	138.07	1.74×10^3
	3	5	0.00	152.55	78.56	58.36	392.79
	4	5	0.00	177.60	48.41	65.43	242.06
	5	5	0.00	28.08	9.13	10.97	45.63
15°	1	9	134.27	4.91×10^3	1.32×10^3	1.45×10^3	1.19×10^4
	2	7	154.12	731.13	324.03	183.07	2.27×10^3
	3	5	46.16	855.15	320.39	282.49	1.60×10^3
	4	3	104.46	205.01	164.88	43.49	494.64
	5	1	50.81	50.81	50.81	0.00	50.81
30°	1	9	262.95	1.03×10^4	1.79×10^3	3.03×10^3	1.61×10^4
	2	7	142.83	671.61	409.42	191.29	2.87×10^3
	3	5	59.83	195.90	145.74	55.59	728.72
	4	3	69.59	239.77	138.35	73.22	415.04
	5	1	0.00	0.00	0.00	0.00	0.00
45°	1	9	158.94	5.73×10^3	1.58×10^3	2.01×10^3	1.42×10^4
	2	7	71.41	339.91	177.98	76.62	1.25×10^3
	3	5	3.97	210.57	84.00	68.96	419.99
	4	3	15.44	175.92	78.55	69.85	235.65
	5	1	16.19	16.19	16.19	0.00	16.19

Table C.3: Statistical analysis of ILF [MN] for each line of turbines (IC = 70%).

Angle	Line	Length	Min	Max	Mean	Std	Sum
0°	1	5	699.50	6.88×10^3	3.70×10^3	2.53×10^3	1.85×10^4
	2	5	125.10	220.22	179.92	34.49	899.61
	3	5	11.99	100.09	59.09	35.38	295.43
	4	5	5.62	54.26	21.19	17.73	105.94
	5	5	0.00	37.35	14.78	12.57	73.89
15°	1	9	261.11	1.12×10^4	2.89×10^3	3.30×10^3	2.60×10^4
	2	7	103.81	2.26×10^3	595.67	711.46	4.17×10^3
	3	5	133.57	634.80	368.04	165.16	1.84×10^3
	4	3	118.64	207.60	154.69	38.23	464.07
	5	1	113.81	113.81	113.81	0.00	113.81
30°	1	9	232.29	1.23×10^4	3.06×10^3	3.70×10^3	2.75×10^4
	2	7	95.73	1.06×10^3	557.81	303.15	3.90×10^3
	3	5	129.19	4.92×10^3	1.14×10^3	1.89×10^3	5.72×10^3
	4	3	38.31	167.46	93.16	54.49	279.47
	5	1	37.39	37.39	37.39	0.00	37.39
45°	1	9	745.50	4.84×10^3	1.66×10^3	1.28×10^3	1.49×10^4
	2	7	114.44	1.27×10^3	449.85	407.91	3.15×10^3
	3	5	22.96	209.95	127.60	70.15	638.02
	4	3	34.77	199.02	125.43	68.13	376.28
	5	1	0.00	0.00	0.00	0.00	0.00

Table C.4: Statistical analysis of ILF [MN] for each line of turbines (IC = 80%).

Angle	Line	Length	Min	Max	Mean	Std	Sum
0°	1	5	677.25	1.35×10^4	5.74×10^3	5.25×10^3	2.87×10^4
	2	5	110.81	525.49	337.48	156.23	1.69×10^3
	3	5	70.59	477.19	250.63	131.52	1.25×10^3
	4	5	8.62	231.34	130.45	77.20	652.27
	5	5	0.00	53.01	22.14	20.22	110.70
15°	1	9	490.68	1.07×10^4	3.92×10^3	4.35×10^3	3.53×10^4
	2	7	374.65	1.95×10^3	785.49	503.69	5.50×10^3
	3	5	141.15	572.13	288.85	148.89	1.44×10^3
	4	3	201.35	505.32	322.79	131.40	968.38
	5	1	353.25	353.25	353.25	0.00	353.25
30°	1	9	74.65	2.66×10^4	6.75×10^3	7.74×10^3	6.08×10^4
	2	7	41.12	4.84×10^3	873.52	1.63×10^3	6.11×10^3
	3	5	32.57	253.19	152.33	94.77	761.63
	4	3	51.88	134.64	97.38	34.29	292.15
	5	1	30.89	30.89	30.89	0.00	30.89
45°	1	9	379.57	1.83×10^4	5.70×10^3	6.18×10^3	5.13×10^4
	2	7	24.96	711.00	382.19	196.56	2.68×10^3
	3	5	28.89	207.26	141.83	63.44	709.13
	4	3	0.00	67.32	25.46	29.83	76.39
	5	1	8.82	8.82	8.82	0.00	8.82

D

ILCF Results

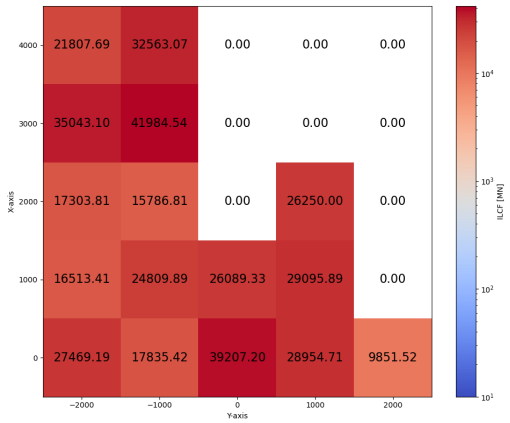

(a) ILCF Scenario 1.1.

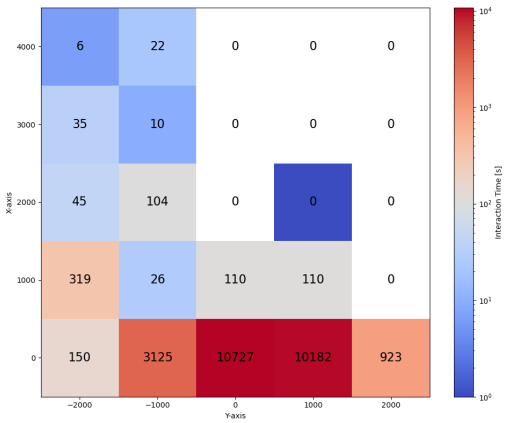

(b) Ice interaction time [s], Scenario 1.1.

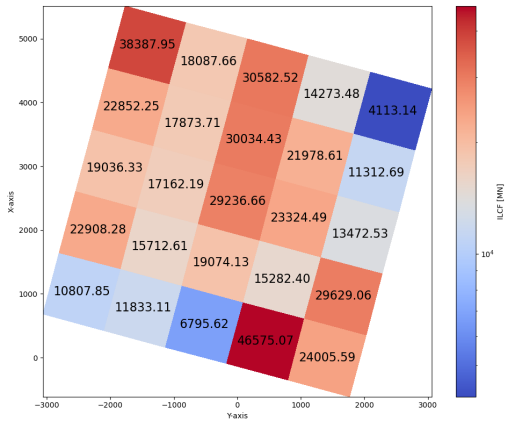

(c) ILCF Scenario 1.2.

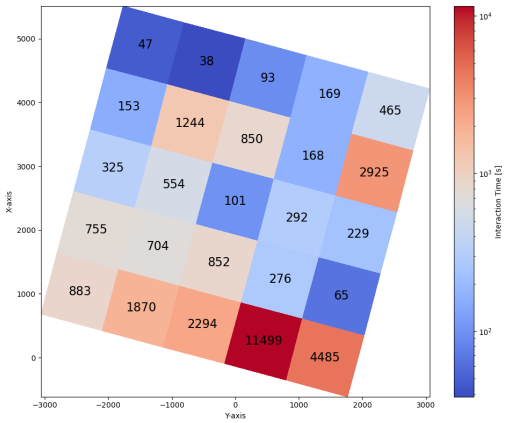

(d) Ice interaction time [s], Scenario 1.2.

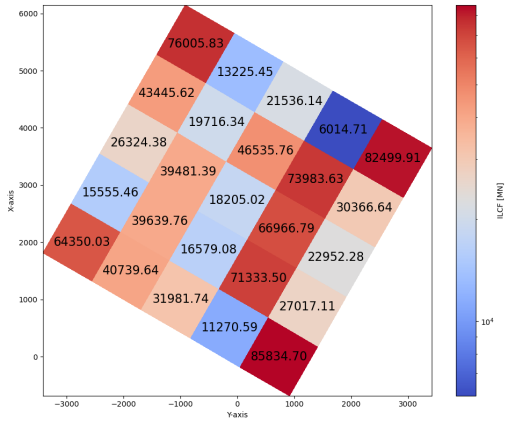

(e) ILCF Scenario 1.3.

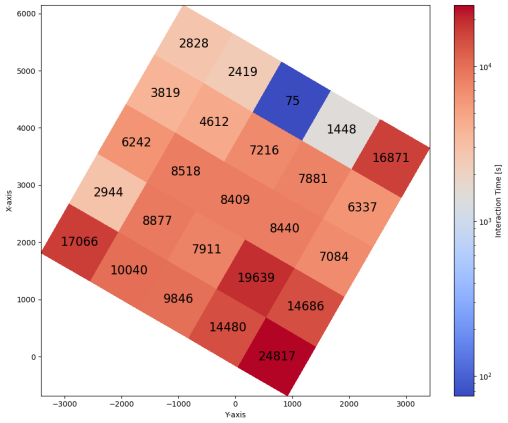

(f) Ice interaction time [s], Scenario 1.3.

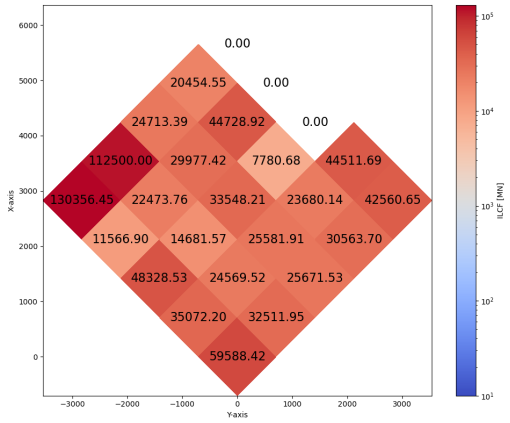

(g) ILCF Scenario 1.4.

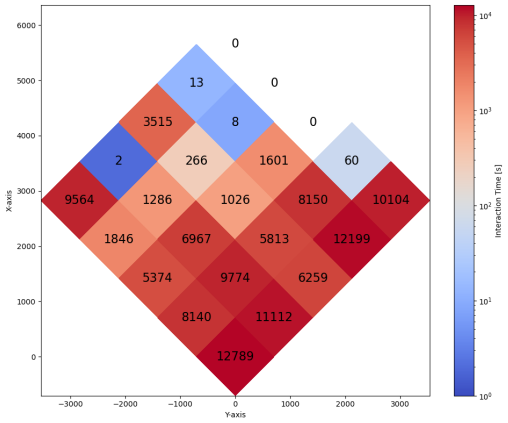

(h) Ice interaction time [s], Scenario 1.4.

Figure D.1: ILCF and Ice Interaction Time for IC = 50%.

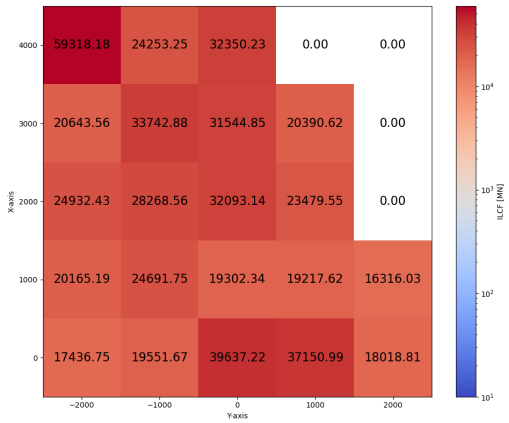

(a) ILCF Scenario 2.1.

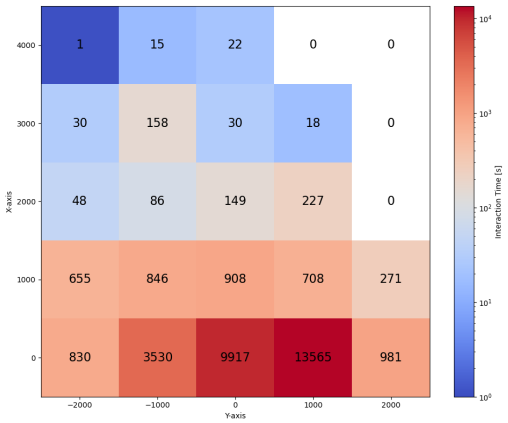

(b) Ice interaction time [s], Scenario 2.1.

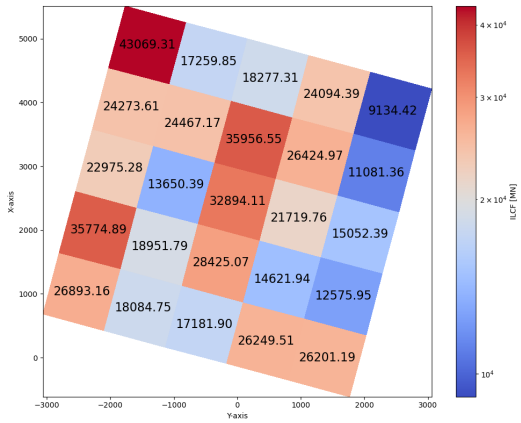

(c) ILCF Scenario 2.2.

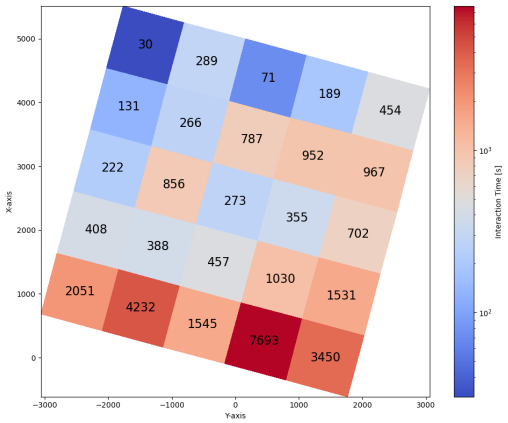

(d) Ice interaction time [s], Scenario 2.2.

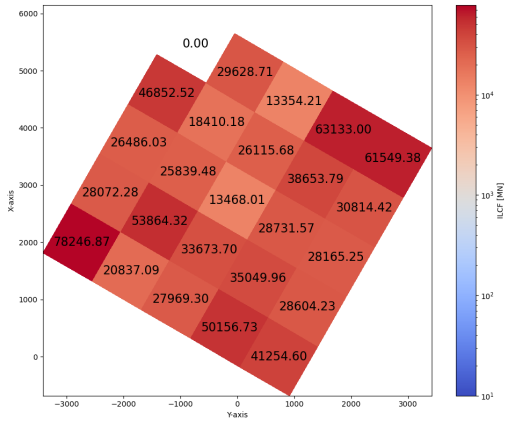

(e) ILCF Scenario 2.3.

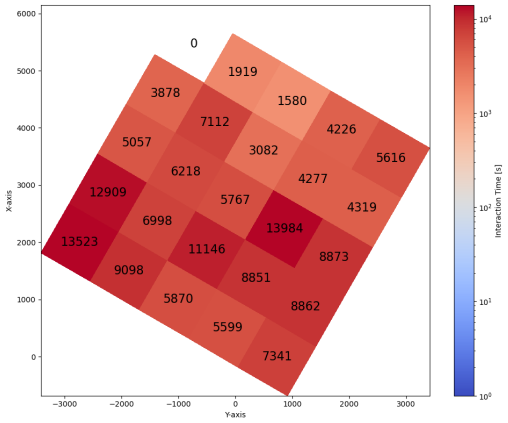

(f) Ice interaction time [s], Scenario 2.3.

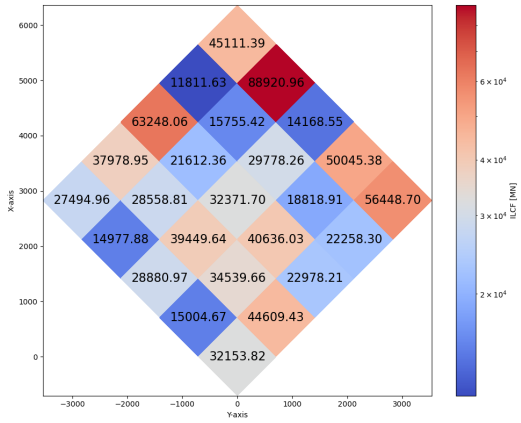

(g) ILCF Scenario 2.4.

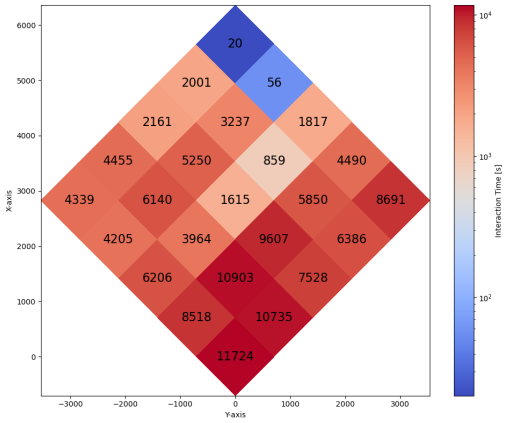

(h) Ice interaction time [s], Scenario 2.4.

Figure D.2: ILCF and Ice Interaction Time for IC = 60%.

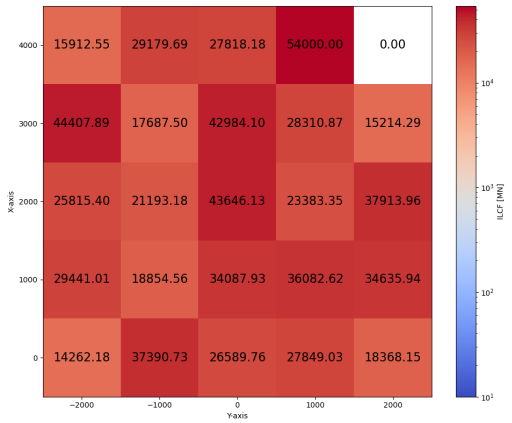

(a) ILCF Scenario 3.1.

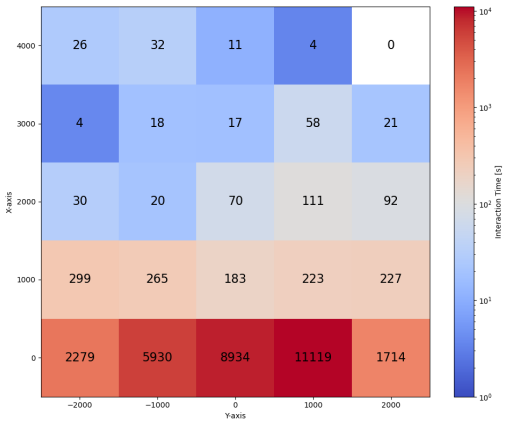

(b) Ice interaction time [s], Scenario 3.1.

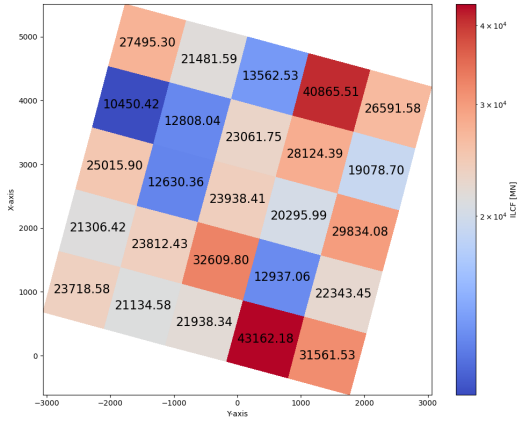

(c) ILCF Scenario 3.2.

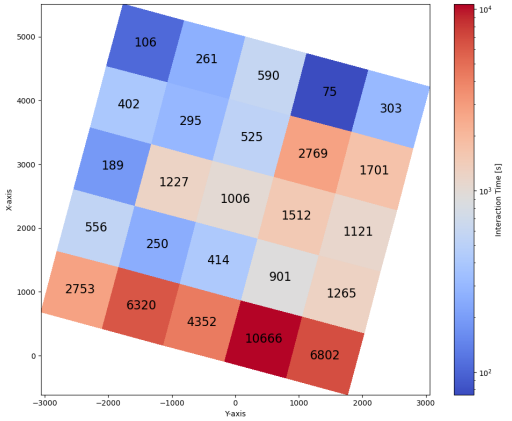

(d) Ice interaction time [s], Scenario 3.2.

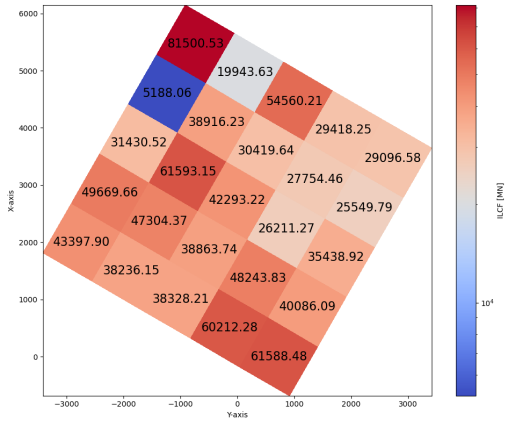

(e) ILCF Scenario 3.3.

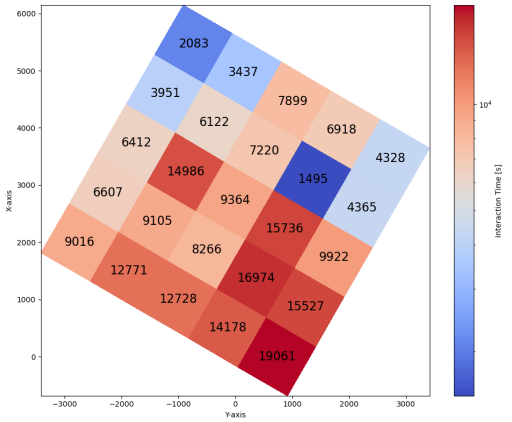

(f) Ice interaction time [s], Scenario 3.3.

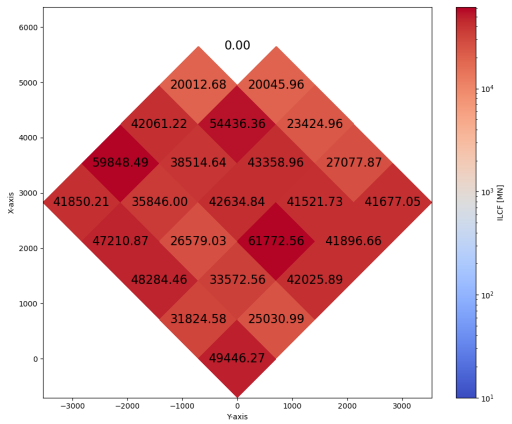

(g) ILCF Scenario 3.4.

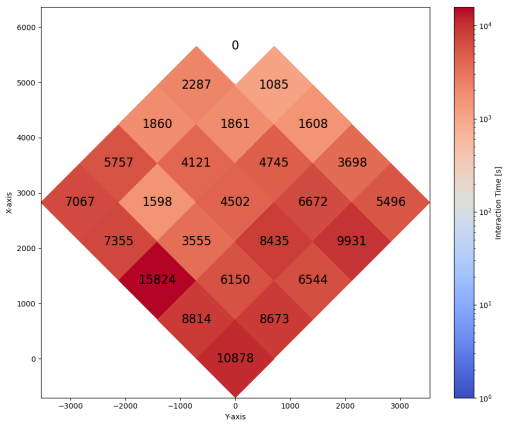

(h) Ice interaction time [s], Scenario 3.4.

Figure D.3: ILCF and Ice Interaction Time for IC = 70%.

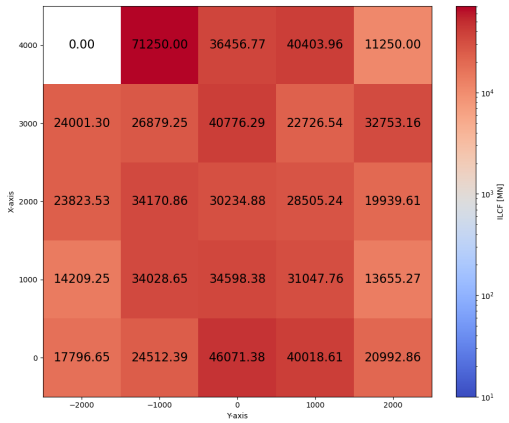

(a) ILCF Scenario 4.1.

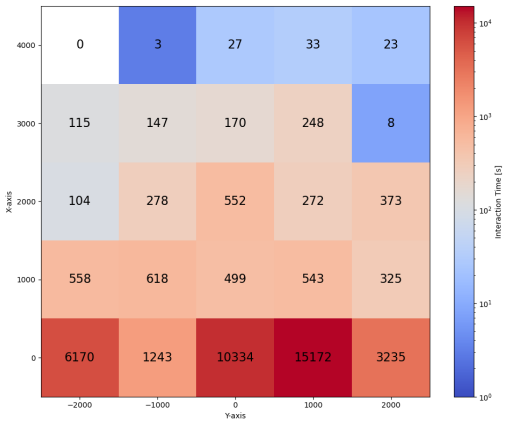

(b) Ice interaction time [s], Scenario 4.1.

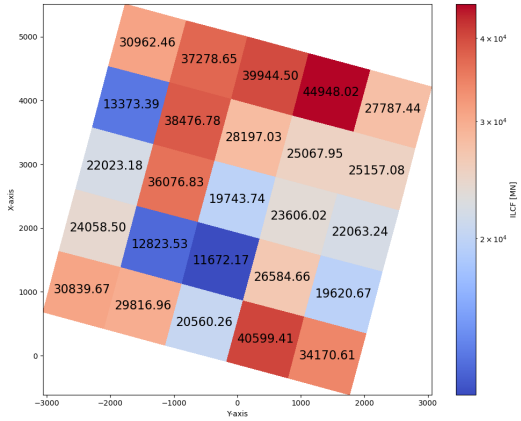

(c) ILCF Scenario 4.2.

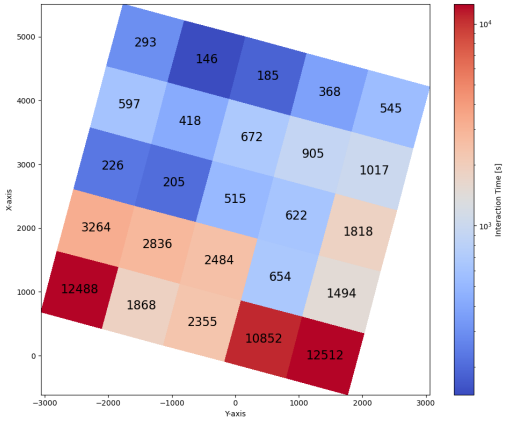

(d) Ice interaction time [s], Scenario 4.2.

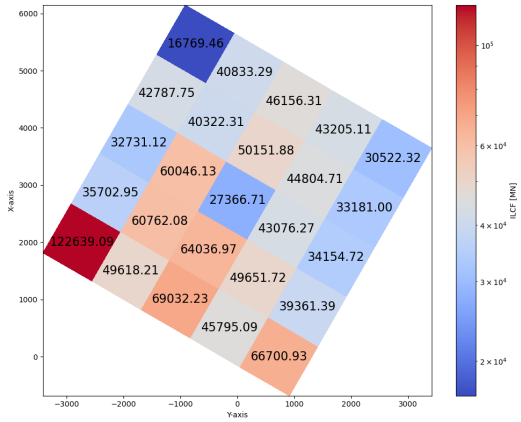

(e) ILCF Scenario 4.3.

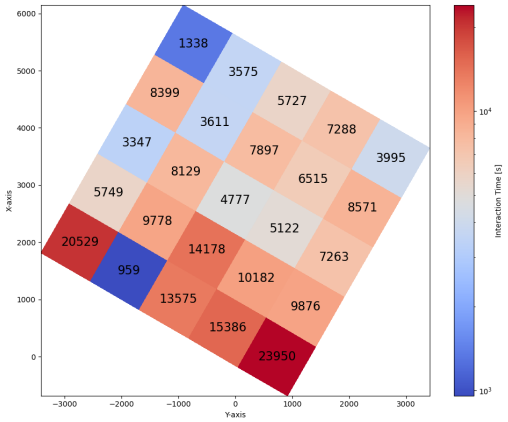

(f) Ice interaction time [s], Scenario 4.3.

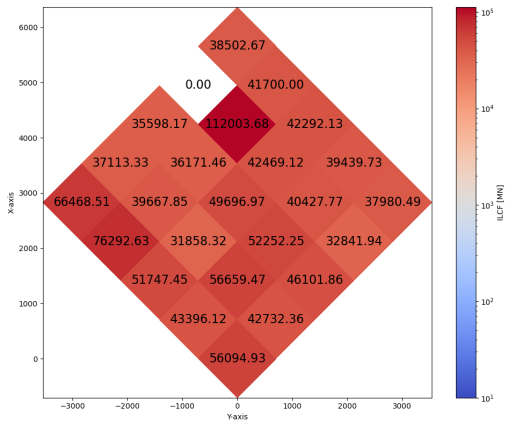

(g) ILCF Scenario 4.4.

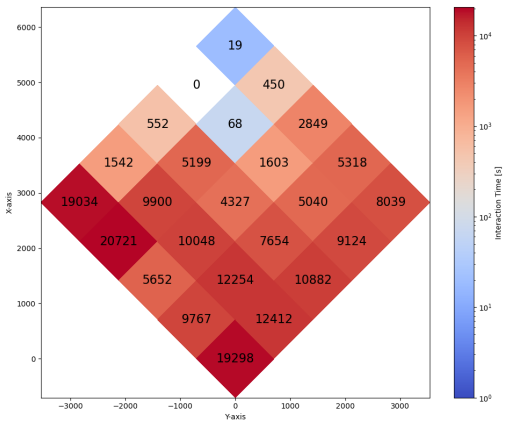

(h) Ice interaction time [s], Scenario 4.4.

Figure D.4: ILCF and Ice Interaction Time for IC = 80%.

Table D.1: Statistical analysis of ILCF [MN] values for IC = 50%.

Dataset	Min	Max	Mean	Std Dev	Sum
Scenario 1.1	0.00	4.20×10^4	1.64×10^4	1.41×10^4	4.11×10^5
Scenario 1.2	4.11×10^3	4.66×10^4	2.06×10^4	9.51×10^3	5.14×10^5
Scenario 1.3	6.01×10^3	8.58×10^4	3.97×10^4	2.42×10^4	9.92×10^5
Scenario 1.4	0.00	1.30×10^5	3.38×10^4	2.99×10^4	8.45×10^5

Table D.2: Statistical analysis of ILCF [MN] values for IC = 60%.

Dataset	Min	Max	Mean	Std Dev	Sum
Scenario 2.1	0.00	5.93×10^4	2.25×10^4	1.34×10^4	5.63×10^5
Scenario 2.2	9.13×10^3	4.31×10^4	2.26×10^4	8.26×10^3	5.65×10^5
Scenario 2.3	0.00	7.82×10^4	3.40×10^4	1.70×10^4	8.49×10^5
Scenario 2.4	1.18×10^4	8.89×10^4	3.35×10^4	1.75×10^4	8.38×10^5

Table D.3: Statistical analysis of ILCF [MN] values for IC = 70%.

Dataset	Min	Max	Mean	Std Dev	Sum
Scenario 3.1	0.00	5.40×10^4	2.82×10^4	1.16×10^4	7.05×10^5
Scenario 3.2	1.05×10^4	4.32×10^4	2.36×10^4	7.97×10^3	5.90×10^5
Scenario 3.3	5.19×10^3	8.15×10^4	4.02×10^4	1.56×10^4	1.01×10^6
Scenario 3.4	0.00	6.18×10^4	3.76×10^4	1.35×10^4	9.40×10^5

Table D.4: Statistical analysis of ILCF [MN] values for IC = 80%.

Dataset	Min	Max	Mean	Std Dev	Sum
Scenario 4.1	0.00	7.12×10^4	2.88×10^4	1.36×10^4	7.20×10^5
Scenario 4.2	1.17×10^4	4.49×10^4	2.74×10^4	8.78×10^3	6.85×10^5
Scenario 4.3	1.68×10^4	1.23×10^5	4.76×10^4	1.97×10^4	1.19×10^6
Scenario 4.4	0.00	1.12×10^5	4.60×10^4	1.90×10^4	1.15×10^6

Table D.5: Statistical analysis of ILCF [MN] for each line of turbines, IC = 50%.

Angle	Line	Length	Min	Max	Mean	Std	Sum
0°	1	5	9.85×10^3	3.92×10^4	2.47×10^4	1.00×10^4	1.23×10^5
	2	5	0.00	2.91×10^4	1.93×10^4	1.05×10^4	9.65×10^4
	3	5	0.00	2.63×10^4	1.19×10^4	1.03×10^4	5.93×10^4
	4	5	0.00	4.20×10^4	1.54×10^4	1.90×10^4	7.70×10^4
	5	5	0.00	3.26×10^4	1.09×10^4	1.38×10^4	5.44×10^4
15°	1	9	4.11×10^3	4.66×10^4	1.76×10^4	1.27×10^4	1.59×10^5
	2	7	1.43×10^4	2.33×10^4	1.89×10^4	3.58×10^3	1.33×10^5
	3	5	1.72×10^4	3.06×10^4	2.52×10^4	5.85×10^3	1.26×10^5
	4	3	1.79×10^4	2.28×10^4	1.96×10^4	2.30×10^3	5.88×10^4
	5	1	3.84×10^4	3.84×10^4	3.84×10^4	0.00	3.84×10^4
30°	1	9	1.13×10^4	8.58×10^4	4.41×10^4	2.54×10^4	3.97×10^5
	2	7	6.01×10^3	7.40×10^4	4.14×10^4	2.71×10^4	2.90×10^5
	3	5	1.82×10^4	4.65×10^4	3.04×10^4	1.08×10^4	1.52×10^5
	4	3	1.32×10^4	4.35×10^4	2.55×10^4	1.30×10^4	7.64×10^4
	5	1	7.60×10^4	7.60×10^4	7.60×10^4	0.00	7.60×10^4
45°	1	9	1.16×10^4	1.30×10^5	4.63×10^4	3.24×10^4	4.16×10^5
	2	7	1.47×10^4	1.13×10^5	3.83×10^4	3.14×10^4	2.68×10^5
	3	5	0.00	3.36×10^4	1.92×10^4	1.31×10^4	9.60×10^4
	4	3	0.00	4.47×10^4	2.17×10^4	1.83×10^4	6.52×10^4
	5	1	0.00	0.00	0.00	0.00	0.00

Table D.6: Statistical analysis of ILCF [MN] for each line of turbines, IC = 60%.

Angle	Line	Length	Min	Max	Mean	Std	Sum
0°	1	5	1.74×10^4	3.96×10^4	2.64×10^4	9.88×10^3	1.32×10^5
	2	5	1.63×10^4	2.47×10^4	1.99×10^4	2.71×10^3	9.97×10^4
	3	5	0.00	3.21×10^4	2.17×10^4	1.13×10^4	1.09×10^5
	4	5	0.00	3.37×10^4	2.13×10^4	1.20×10^4	1.06×10^5
	5	5	0.00	5.93×10^4	2.32×10^4	2.22×10^4	1.16×10^5
15°	1	9	9.13×10^3	2.69×10^4	1.80×10^4	6.49×10^3	1.62×10^5
	2	7	1.46×10^4	3.58×10^4	2.43×10^4	6.35×10^3	1.70×10^5
	3	5	1.36×10^4	3.60×10^4	2.47×10^4	8.49×10^3	1.24×10^5
	4	3	1.73×10^4	2.45×10^4	2.20×10^4	3.35×10^3	6.60×10^4
	5	1	4.31×10^4	4.31×10^4	4.31×10^4	0.00	4.31×10^4
30°	1	9	2.08×10^4	7.82×10^4	4.08×10^4	1.79×10^4	3.68×10^5
	2	7	2.81×10^4	6.31×10^4	4.02×10^4	1.23×10^4	2.81×10^5
	3	5	1.33×10^4	2.65×10^4	2.11×10^4	6.24×10^3	1.05×10^5
	4	3	1.84×10^4	4.69×10^4	3.16×10^4	1.17×10^4	9.49×10^4
	5	1	0.00	0.00	0.00	0.00	0.00
45°	1	9	1.50×10^4	5.64×10^4	2.94×10^4	1.28×10^4	2.65×10^5
	2	7	1.88×10^4	5.01×10^4	3.57×10^4	9.16×10^3	2.50×10^5
	3	5	1.42×10^4	6.33×10^4	3.22×10^4	1.68×10^4	1.61×10^5
	4	3	1.18×10^4	8.89×10^4	3.88×10^4	3.55×10^4	1.16×10^5
	5	1	4.51×10^4	4.51×10^4	4.51×10^4	0.00	4.51×10^4

Table D.7: Statistical analysis of ILCF [MN] for each line of turbines, IC = 70%.

Angle	Line	Length	Min	Max	Mean	Std	Sum
0°	1	5	1.43×10^4	3.74×10^4	2.49×10^4	8.04×10^3	1.24×10^5
	2	5	1.88×10^4	3.61×10^4	3.06×10^4	6.29×10^3	1.53×10^5
	3	5	2.12×10^4	4.37×10^4	3.04×10^4	8.80×10^3	1.52×10^5
	4	5	1.52×10^4	4.44×10^4	2.97×10^4	1.22×10^4	1.49×10^5
15°	1	9	1.91×10^4	4.32×10^4	2.66×10^4	7.02×10^3	2.39×10^5
	2	7	1.29×10^4	4.09×10^4	2.57×10^4	8.44×10^3	1.80×10^5
	3	5	1.26×10^4	2.50×10^4	1.96×10^4	5.39×10^3	9.82×10^4
	4	3	1.05×10^4	2.15×10^4	1.49×10^4	4.74×10^3	4.47×10^4
	5	1	2.75×10^4	2.75×10^4	2.75×10^4	0	2.75×10^4
30°	1	9	2.56×10^4	6.16×10^4	4.13×10^4	1.17×10^4	3.72×10^5
	2	7	2.62×10^4	4.97×10^4	3.82×10^4	9.60×10^3	2.67×10^5
	3	5	3.04×10^4	6.16×10^4	4.41×10^4	1.24×10^4	2.20×10^5
	4	3	5.19×10^3	3.89×10^4	2.14×10^4	1.38×10^4	6.41×10^4
	5	1	8.15×10^4	8.15×10^4	8.15×10^4	0	8.15×10^4
45°	1	9	2.50×10^4	4.94×10^4	4.10×10^4	7.49×10^3	3.69×10^5
	2	7	2.66×10^4	6.18×10^4	4.09×10^4	1.35×10^4	2.86×10^5
	3	5	2.34×10^4	4.34×10^4	3.80×10^4	7.48×10^3	1.90×10^5
	4	3	2.00×10^4	5.44×10^4	3.15×10^4	1.62×10^4	9.45×10^4

Table D.8: Statistical analysis of ILCF [MN] for each line of turbines, IC = 80%.

Angle	Line	Length	Min	Max	Mean	Std	Sum
0°	1	5	1.78×10^4	4.61×10^4	2.99×10^4	1.11×10^4	1.49×10^5
	2	5	1.37×10^4	3.46×10^4	2.55×10^4	9.53×10^3	1.28×10^5
	3	5	1.99×10^4	3.42×10^4	2.73×10^4	4.97×10^3	1.37×10^5
	4	5	2.27×10^4	4.08×10^4	2.94×10^4	6.64×10^3	1.47×10^5
15°	1	9	1.96×10^4	4.06×10^4	2.79×10^4	6.47×10^3	2.51×10^5
	2	7	1.17×10^4	4.50×10^4	2.41×10^4	1.02×10^4	1.69×10^5
	3	5	1.97×10^4	3.99×10^4	2.92×10^4	7.81×10^3	1.46×10^5
	4	3	1.34×10^4	3.85×10^4	2.97×10^4	1.16×10^4	8.91×10^4
	5	1	3.10×10^4	3.10×10^4	3.10×10^4	0	3.10×10^4
30°	1	9	3.05×10^4	1.23×10^5	5.46×10^4	2.74×10^4	4.91×10^5
	2	7	3.57×10^4	6.40×10^4	4.88×10^4	9.47×10^3	3.41×10^5
	3	5	2.74×10^4	6.01×10^4	4.33×10^4	1.18×10^4	2.16×10^5
	4	3	4.03×10^4	4.28×10^4	4.13×10^4	1.06×10^3	1.24×10^5
	5	1	1.68×10^4	1.68×10^4	1.68×10^4	0	1.68×10^4
45°	1	9	3.28×10^4	7.63×10^4	5.04×10^4	1.31×10^4	4.54×10^5
	2	7	3.19×10^4	5.67×10^4	4.25×10^4	8.10×10^3	2.97×10^5
	3	5	3.56×10^4	4.97×10^4	4.13×10^4	5.13×10^3	2.06×10^5
	5	1	3.85×10^4	3.85×10^4	3.85×10^4	0	3.85×10^4

Table D.9: Percentual change compared to the ILCF [MN] sum of the first line for each IC.

Line	IC = 50			
	0°	15°	30°	45°
Line 2	-21.74	-16.39	-26.94	-35.61
Line 3	-51.88	-20.49	-61.69	-76.93
Line 4	-37.54	-62.90	-80.76	-84.34
Line 5	-55.91	-75.79	-80.86	-100.00
Line	**IC = 60**			
	0°	15°	30°	45°
Line 2	-24.36	4.65	-23.51	-5.58
Line 3	-17.47	-23.82	-71.36	-39.13
Line 4	-19.33	-59.37	-74.19	-56.01
Line 5	-12.04	-73.49	-100.00	-82.96
Line	**IC = 70**			
	0°	15°	30°	45°
Line 2	23.01	-24.82	-28.09	-22.49
Line 3	22.09	-58.97	-40.77	-48.55
Line 4	19.40	-81.31	-82.78	-74.41
Line 5	1.97	-88.51	-78.09	-100.00
Line	**IC = 80**			
	0°	15°	30°	45°
Line 2	-14.63	-32.66	-30.50	-34.44
Line 3	-8.51	-41.75	-55.92	-54.54
Line 4	-1.51	-64.44	-74.76	-66.12
Line 5	6.67	-87.65	-96.58	-91.51

Table D.10: Percentual change compared to the ILCF [MN] mean of the first line for each IC.

Line	IC = 50			
	0°	15°	30°	45°
Line 2	-21.74	7.49	-6.06	-17.21
Line 3	-51.88	43.11	-31.05	-58.48
Line 4	-37.54	11.29	-42.28	-53.02
Line 5	-55.91	117.91	72.30	-100.00
Line	**IC = 60**			
	0°	15°	30°	45°
Line 2	-24.36	34.55	-1.65	21.40
Line 3	-17.47	37.12	-48.46	9.56
Line 4	-19.33	21.88	-22.56	31.97
Line 5	-12.04	138.60	-100.00	53.32
Line	**IC = 70**			
	0°	15°	30°	45°
Line 2	23.01	-3.34	-7.54	-0.34
Line 3	22.09	-26.15	6.61	-7.38
Line 4	19.40	-43.93	-48.34	-23.23
Line 5	1.97	3.38	97.21	-100.00
Line	**IC = 80**			
	0°	15°	30°	45°
Line 2	-14.63	-13.42	-10.65	-15.71
Line 3	-8.51	4.85	-20.65	-18.17
Line 4	-1.51	6.69	-24.27	1.64

E

Ice Load Return Period

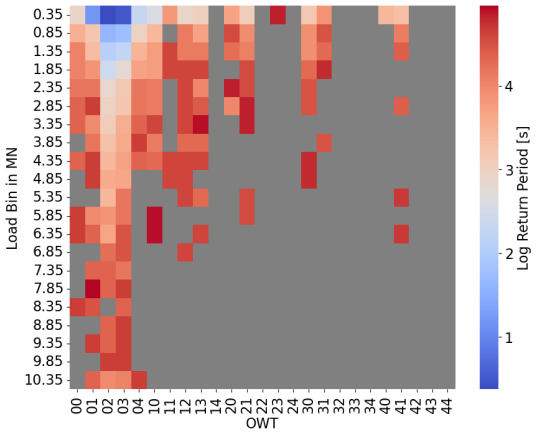

(a) Return Period for Scenario 1.1.

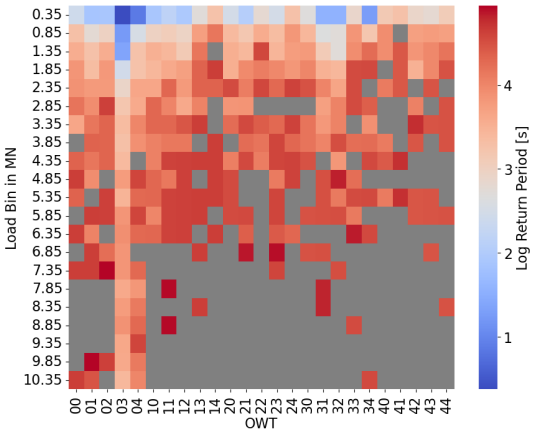

(b) Return Period for Scenario 1.2.

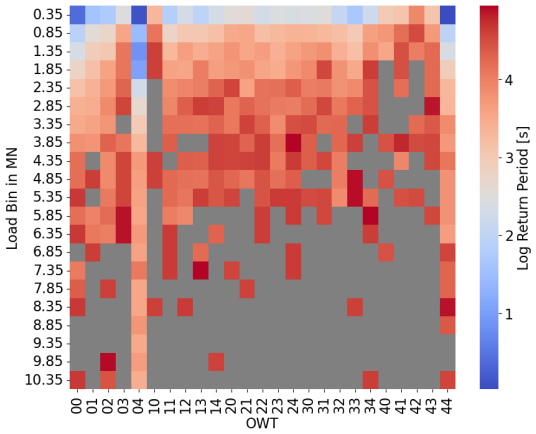

(c) Return Period for Scenario 1.3.

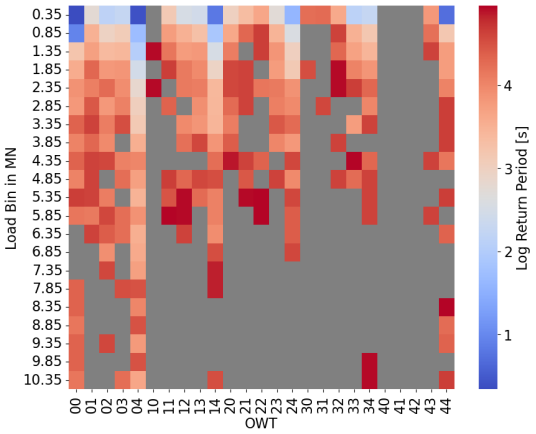

(d) Return Period for Scenario 1.4.

Figure E.1: Return Period for IC = 50%.

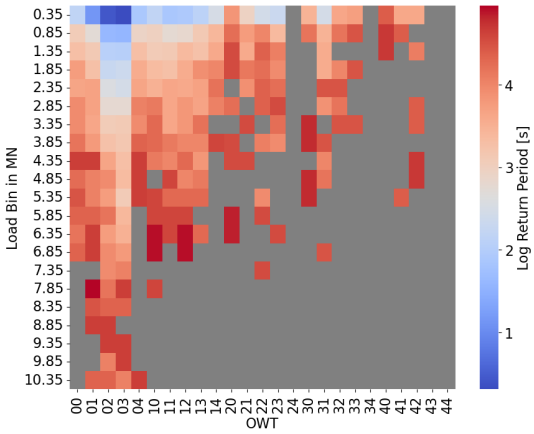

(a) Return Period for Scenario 2.1.

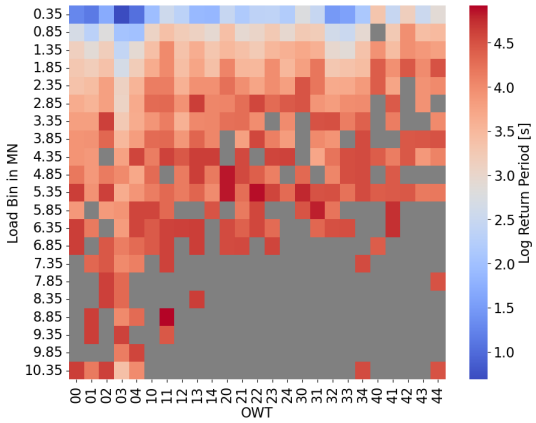

(b) Return Period for Scenario 2.2.

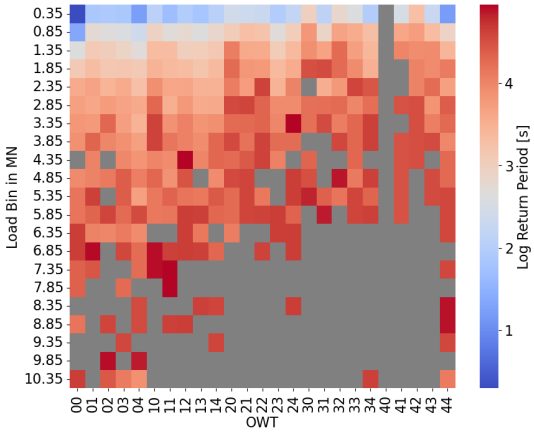

(c) Return Period for Scenario 2.3.

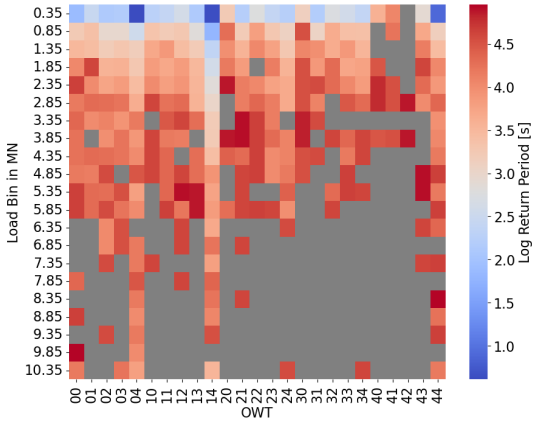

(d) Return Period for Scenario 2.4.

Figure E.2: Return Period for IC = 60%.

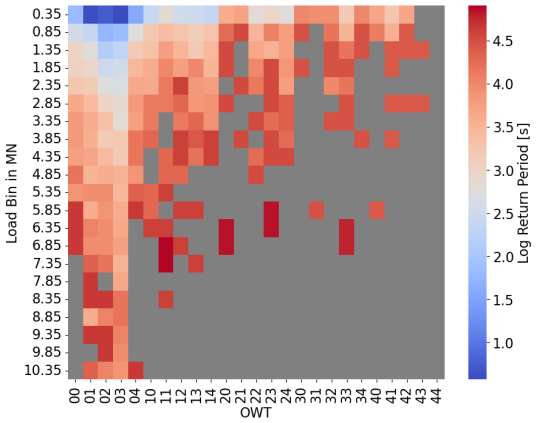

(a) Return Period for Scenario 3.1.

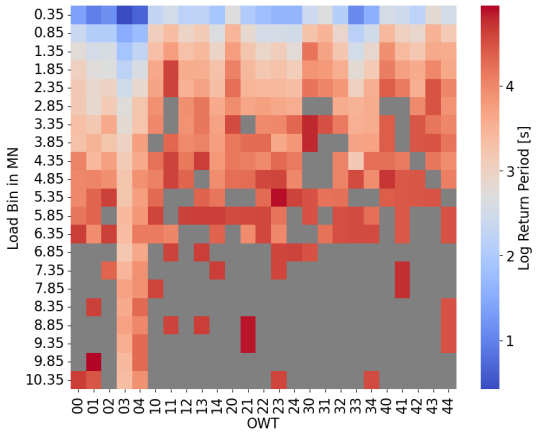

(b) Return Period for Scenario 3.2.

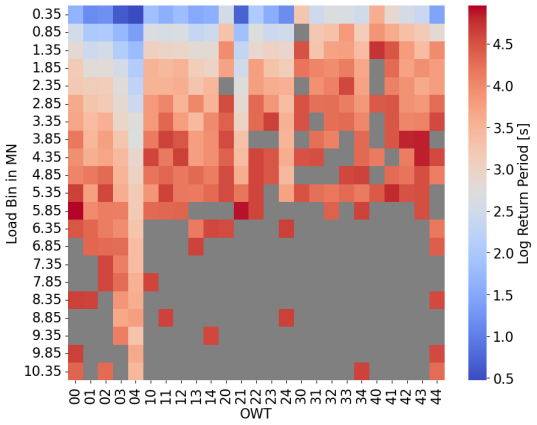

(c) Return Period for Scenario 3.3.

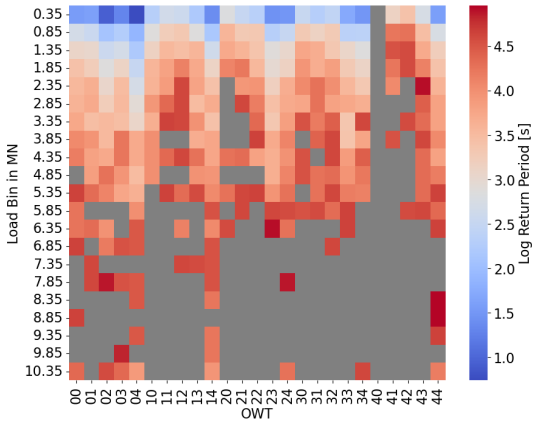

(d) Return Period for Scenario 3.4.

Figure E.3: Return Period for IC = 70%.

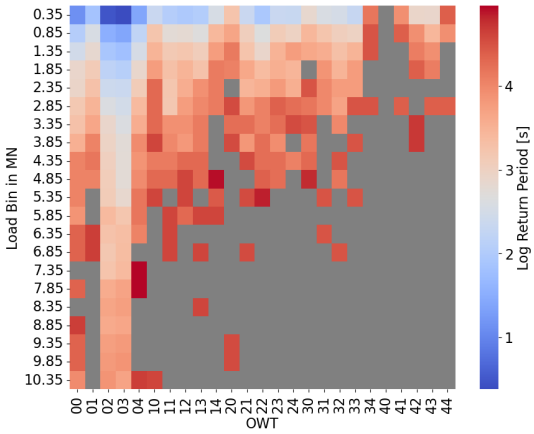

(a) Return Period for Scenario 4.1.

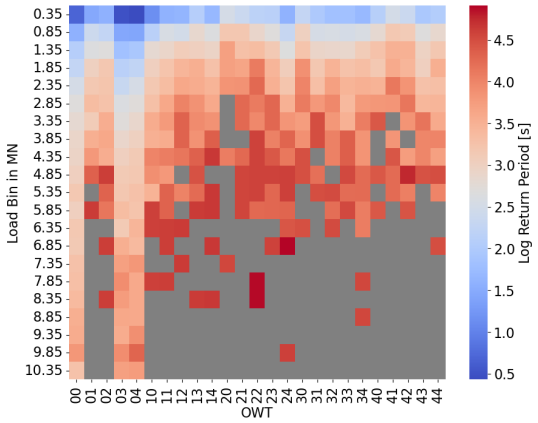

(b) Return Period for Scenario 4.2.

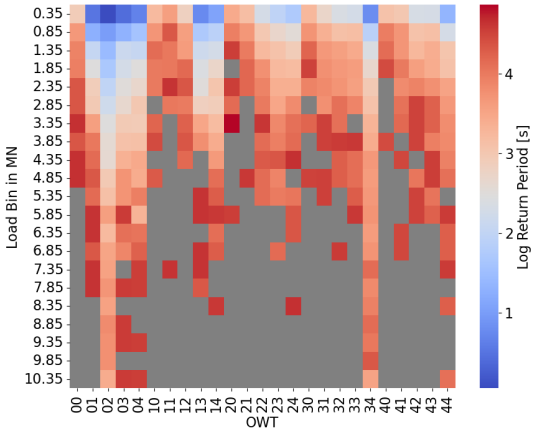

(c) Return Period for Scenario 4.3.

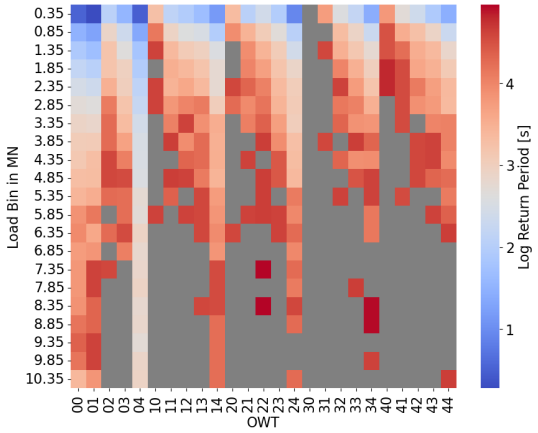

(d) Return Period for Scenario 4.4.

Figure E.4: Return Period for IC = 80%.

F

Machine Learning Results

Table F.1: Prediction and absolute error for every value in the test data set using different ML regressors.

Actual ILF	LR Pred	LR Abs Error	DTR Pred	DTR Abs Error	RFR Pred	RFR Abs Error	SVR Pred	SVR Abs Error
196.82	2732.82	2536.00	110.81	86.01	349.78	152.97	219.24	22.42
324.49	339.22	14.72	157.63	166.86	129.19	195.30	212.03	112.46
95.82	2502.43	2406.62	304.69	208.87	264.82	169.00	218.37	122.55
22.27	1783.46	1761.18	70.59	48.31	158.57	136.29	215.68	193.40
191.10	995.97	804.87	0.00	191.10	235.69	44.59	214.79	23.69
3521.21	2989.21	532.00	5733.73	2212.52	2917.61	603.59	219.57	3301.64
10735.99	3679.94	7056.06	5390.81	5345.19	5923.71	4812.28	221.33	10514.66
206.36	1662.50	1456.14	0.00	206.36	161.19	45.18	216.68	10.32
167.46	-185.84	353.30	199.02	31.56	184.45	16.99	211.20	43.74
1751.00	2927.14	1176.13	506.16	1244.85	1036.98	714.02	218.72	1532.29
0.00	2716.68	2716.68	42.93	42.93	133.50	133.50	219.24	219.24
42.67	635.49	592.82	659.69	617.02	362.88	320.22	213.08	170.42
461.96	1424.55	962.59	78.01	383.96	307.86	154.11	215.00	246.96
30.57	-543.10	573.67	100.28	69.71	51.72	21.15	210.84	180.27
304.07	2264.95	1960.87	339.91	35.84	426.83	122.76	217.46	86.61
770.93	441.39	329.54	855.15	84.22	443.97	326.96	213.00	557.93
1436.38	3002.16	1565.78	1516.16	79.78	1647.37	210.98	219.13	1217.25
13947.98	1677.17	12270.81	1954.97	11993.01	1001.16	12946.83	215.36	13732.62
143.74	2027.46	1883.71	876.92	733.18	1039.63	895.88	216.53	72.79
28.89	-316.07	344.96	353.25	324.36	186.82	157.93	210.58	181.69
347.98	2319.50	1971.52	379.84	31.87	507.55	159.57	217.25	130.73
40.65	826.96	786.31	174.95	134.30	30.28	10.37	213.31	172.66
9.08	-312.89	321.97	167.20	158.12	178.00	168.93	210.99	201.91
73.70	-999.10	1072.80	142.48	68.79	107.96	34.26	209.42	135.72
91.62	3648.07	3556.44	1238.65	1147.03	2093.64	2002.01	220.28	128.66
67.32	-976.25	1043.56	105.64	38.33	107.08	39.76	209.65	142.33
0.00	1784.38	1784.38	136.35	136.35	133.06	133.06	216.93	216.93
1451.05	2689.65	1238.60	851.05	600.00	2639.76	1188.71	217.79	1233.26
364.93	1099.55	734.62	423.16	58.23	316.61	48.32	214.55	150.39
392.85	3665.12	3272.27	202.00	190.85	852.84	459.99	221.45	171.40
8.82	-1642.78	1651.60	105.64	96.82	66.68	57.86	207.91	199.08
125.05	1004.03	878.98	75.30	49.75	272.03	146.98	214.79	89.74
4920.89	627.42	4293.47	2264.20	2656.69	468.01	4452.88	213.08	4707.81
257.03	1896.68	1639.66	46.86	210.16	264.06	7.04	216.47	40.56
316.04	2273.01	1956.97	340.39	24.34	908.94	592.89	217.46	98.59
177.60	837.27	659.67	20.85	156.75	37.63	139.97	213.59	35.99
152.55	1782.13	1629.58	136.35	16.20	136.81	15.74	216.62	64.07
572.13	465.59	106.54	365.58	206.55	428.92	143.21	213.00	359.13
629.76	2376.88	1747.12	341.74	288.02	555.03	74.73	217.93	411.83
205.01	203.90	1.12	698.87	493.86	387.72	182.70	212.09	7.07
300.30	1013.81	713.51	124.10	176.20	152.39	147.91	213.88	86.42
33.33	952.42	919.09	174.95	141.62	307.16	273.83	213.57	180.24
122.74	1652.97	1530.22	78.01	44.74	324.29	201.54	215.36	92.61
212.05	2673.51	2461.46	7733.95	7521.90	4742.15	4530.10	217.79	5.74
132.57	1656.14	1523.58	78.01	54.56	141.20	8.63	215.79	83.22
436.44	1680.34	1243.90	271.41	165.03	403.61	32.83	215.79	220.65
154.12	-212.74	366.85	81.74	72.38	84.83	69.29	211.79	57.68
185.45	997.68	812.23	318.88	133.43	233.99	48.54	213.88	28.43
0.00	-108.92	108.92	28.08	28.08	29.29	29.29	211.55	211.55
171.66	-62.90	234.57	134.27	37.39	133.09	38.57	212.30	40.64
25.82	-711.92	737.73	4.21	21.60	123.28	97.47	209.95	184.13
8.55	-86.97	95.52	38.79	30.24	83.11	74.56	211.24	202.69
374.65	1618.89	1244.24	555.63	180.98	581.74	207.09	216.16	158.49
65.68	-1487.36	1553.04	0.00	65.68	13.44	52.24	208.09	142.41
1290.60	425.36	865.24	1129.35	161.25	2137.95	847.35	213.78	1076.82
76.25	1840.24	1764.00	0.00	76.25	191.63	115.39	217.07	140.82
7.56	-90.54	98.10	0.00	7.56	34.39	26.83	211.89	204.33
59.83	-535.04	594.87	46.16	13.67	59.74	0.09	210.84	151.00
430.56	1765.77	1335.21	22.05	408.51	368.90	61.66	215.62	214.94
569.31	2718.01	2148.70	522.17	47.14	486.88	82.43	218.36	350.95
0.00	-96.36	96.36	0.00	0.00	12.00	12.00	212.27	212.27
994.48	1678.63	684.15	782.33	212.15	606.11	388.37	216.68	777.80
542.39	968.55	426.16	66.66	475.73	316.74	225.65	213.57	328.82
278.29	2986.03	2707.73	330.17	51.88	665.50	387.20	219.13	59.16
1533.85	3658.38	2124.53	321.65	1212.20	1639.44	105.59	220.64	1313.21
266.81	2011.32	1744.51	46.86	219.95	260.99	5.82	216.53	50.28
26609.79	2734.14	23875.65	525.49	26084.31	619.13	25990.67	218.36	26391.44
95.73	758.42	662.69	54.26	41.47	393.82	298.09	214.13	118.40
1204.97	1686.70	481.73	716.91	488.06	569.82	635.15	216.68	988.29
61.02	-70.97	131.99	61.94	0.93	134.64	73.63	212.30	151.29
0.00	-89.21	89.21	38.79	38.79	79.59	79.59	211.00	211.00
104.46	-41.66	146.12	114.82	10.36	143.88	39.43	211.22	106.77
131.65	2707.70	2576.04	330.36	198.70	425.56	293.91	218.02	86.37
70.70	-957.47	1028.17	143.78	73.08	77.55	6.85	209.12	138.42
522.12	1683.52	1161.40	1271.63	749.51	855.86	333.74	216.24	305.88
207.60	-695.78	903.39	283.10	75.50	170.94	36.66	209.95	2.34
2251.42	3180.76	929.34	1141.50	1109.91	1860.03	391.39	219.63	2031.79
4506.47	1238.62	3267.85	232.29	4274.18	376.43	4130.03	215.60	4290.87

Continued on next page

.00

Table F.1 – continued from previous page

Actual ILF	LR Pred	LR Abs Error	DTR Pred	DTR Abs Error	RFR Pred	RFR Abs Error	SVR Pred	SVR Abs Error
176.36	1661.03	1484.68	363.18	186.82	434.92	258.57	215.36	39.00
935.59	2341.99	1406.40	1062.44	126.85	1582.48	646.89	218.13	717.46